MAGNETIC NANOSTRUCTURES PATTERNED BY BLOCK COPOLYMER LITHOGRAPHY

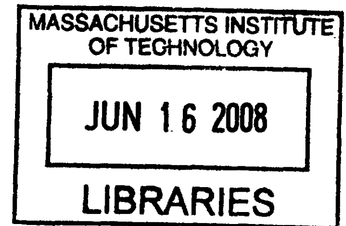

MASSACHUSETTS INSTITUTE OF TECHNOLOGY
JUN 16 2008
LIBRARIES
ARCHIVES

by

Filip Ilievski

B.S. Materials Science and Engineering

Massachusetts Institute of Technology, 2003

Submitted to the Department of Materials Science and Engineering
in partial fulfillment of the requirements for the degree of

Doctor of Philosophy in Materials Science and Engineering

at the

Massachusetts Institute of Technology

June 2008

© Massachusetts Institute of Technology. All rights reserved.

Signature of Author ______________________________
Department of Materials Science and Engineering
May 15, 2008

Certified by ______________________________
Caroline A. Ross
Toyota Professor of Materials Science and Engineering
Thesis Supervisor

Accepted by ______________________________
Samuel M. Allen
POSCO Professor of Physical Metallurgy
Chair, Departmental Committee on Graduate Students

Room 14-0551
77 Massachusetts Avenue
Cambridge, MA 02139
Ph: 617.253.5668 Fax: 617.253.1690
Email: docs@mit.edu
http://libraries.mit.edu/docs

DISCLAIMER OF QUALITY

Due to the condition of the original material, there are unavoidable flaws in this reproduction. We have made every effort possible to provide you with the best copy available. If you are dissatisfied with this product and find it unusable, please contact Document Services as soon as possible.

Thank you.

Missing pages 3-4

MAGNETIC NANOSTRUCTURES PATTERNED BY BLOCK COPOLYMER LITHOGRAPHY

by

Filip Ilievski

Submitted to the Department of Materials Science and Engineering on May 15, 2008 in partial fulfillment of the requirements for the degree of Doctor of Philosophy in Materials Science and Engineering at the Massachusetts Institute of Technology.

Abstract

The aim of this research was twofold: understanding the methods of patterning magnetic films using self-assembled block copolymer masks and examining the magnetic reversal mechanisms of as deposited and patterned magnetic films. Ti / Co 66 at. % Cr 22 at. % Pt 12 at. % (CoCrPt) films with perpendicular magnetic anisotropy were deposited on silicon wafers by UHV sputtering. Ti was used as an adhesion layer and texture promoter so that the easy magnetic axis of Co is aligned perpendicular to the sample plane. Magnetic reversal of Ti/CoCrPt films and Ti/CoCrPt/Ti/CoCrPt pseudo spin valve films is a domain nucleation and growth process with a slow time-dependent magnetization reversal which was attributed to growth of reverse domains.

The films were patterned into nanosized islands by block copolymer lithography using self assembled polystyrene-polyferrocenyldimethylsilane (PS-PFS) as a mask. The islands reverse their magnetization in a coherent and independent fashion (Stoner-Wohlfarth reversal), in contrast to the continuous film. Micromagnetic simulation confirmed the coherent reversal of the thicker islands.

Two graphoepitaxy methods were examined for inducing long range order (LRO) in block copolymers. Nanoimprint lithography with in-situ annealing was successful in guiding the self assembly of the block copolymers in the grooves, however, no LRO was achieved. Selectively removable polymeric templates fabricated out of BARL-i® anti reflection coating guide the self-assembly of PFS domains with good LRO and very few defects over a large area. The ordered arrays were then transferred into silica and W, forming an ordered array of cp-packed W islands with period of 29 nm and island diameter of 17 nm. Transfer of the pattern into CoCrPt is difficult due to the non-selective ion beam etching process.

Thesis supervisor: Caroline A. Ross,
Toyota Professor of Materials Science and Engineering

Магнетни Наноструктури Оформени со Блок Кополимерна Литографија

од

Филип Илиевски

Приложено кон Одделот за Наука и Инжињерство на Материјали за делумно задоволување на условите за доделување на степен Доктор на Филозофија во Наука и Инжињерство на Материјали при Масачусетс Инситутот за Технологија, 15 мај 2008.

Абстракт

Целта на овој научен труд е разјаснување на методите за обликување магнетни тенки филмови користејќи калапи од само-организирани блок кополимери. Дополнително, испитани се механизмите на промена на магнетните домени во тенки магнетни филмови и во магнетни нано-структури. Со физичка гасна депозиција нанесовме тенки филмови од титаниум / кобалт 66 ат. % хром 22 ат. % платина 12 ат. % (CoCrPt) на силициумски плочки. Титаниумот служи за индуцирање на кристална текстура во филмот од CoCrPt за да ја ориентира кристалната ц-оска на кобалтот нормално на рамнината на филмот. Магнетните промени во еднослојни филмови и двослојни псевдо-електрон-спин-вентили се одвиваат по стандардна нуклеација и растеж на инверзни магнетни домени проследени со спори промени во севкупната магнетизацијата заради магнетна вискозност.

Тенките филмови беа оформени во овални нано-елементи користејќи блок-кополимерна литографија, за која користевме самоорганизиран полистирен-полифероценилдиметилсилан како калап (маска). Магнетните наноелементите ја ротираат својата магнетизатција индивидуално и кохерентно (ротација од тип Стонер-Волфхарт), спротивно од непрекинатите тенки филмови. Микромагнетна симулација ги потврди наодите за кохерентна ротација во подебелите нано-елементи.

Два метода на графоепитаксија беа испитани за подобрување на далекуопсежно подредување (ДОП). Литографија на нано-втиснување со локално калење успешно го води само-организирањето на блок кополимери во тесни канали, но ДОП не беше постигнато. Селективно отстранливи полимерски мостри фабрикувани од Barl-i анти-рефлективен слој успешно го водат ДОП на микродомените со минимални дефекти на голема површина. Структурата на подредените полимерски домени беше префрлена во слоеви од силициум диоксид и волфрам, формирајќи хексагонално подредена матрица од елементи со дијаметар од 17 нм и период од 29 нм. Трансфер во магнетниот филм од CoCrPt е тешко да се изврши заради неселективната природа на процесот на нагризување со јонски сноп.

Академски ментор: Керолајн А. Рос / Caroline A. Ross,
Тојота Професор по Наука и Инжињерство на Материјали

Table of contents

Chapter 1 Motivation and scope **21**

1.1 Introduction *21*

1.2 Contents of this thesis *23*

Chapter 2 Magnetic media and magnetic characterization **27**

2.1 Continuous-media hard drive technology *27*

2.2 Approaches to increasing the data density of hard drives *29*

2.3 Bit patterned media requirements *31*

2.4 Magnetic characterization *32*

2.4.1. Introduction 32

2.4.2. The vibrating sample magnetometer (VSM) 33

2.4.3. The Alternating Gradient Field Magnetometer 35

2.4.4. Comparison of the magnetometry instrumental techniques 38

2.5 Sweep rate dependent magnetic reversal measurements *39*

2.5.1. Small particle magnetism 39

2.6 Imaging magnetism on the micro- and nano-scale *44*

2.6.1. Introduction 44

2.6.2. Scanning probe and magnetic force microscopy 46

Chapter 3 Pattern formation by block copolymer, interference and nanoimprint lithography **53**

3.1 Introduction *53*

3.1.1. Methods of inducing microphase segregation 57

3.1.2. Surface modifications 59

3.2 Directed (templated) self-assembly *60*

3.2.1. Introduction 60

3.2.2. Chemical epitaxy of block copolymers 61

3.2.3. Graphoepitaxy of block copolymers 62

3.3 Pattern transfer from block copolymers *65*

3.3.1. Introduction 65

3.3.2. Additive methods 65

3.3.3. Subtractive methods 66

3.4 Unconventional lithography methods *68*

3.4.1. The Lloyd's mirror interferometer lithography tool 68

3.4.2. Tri-layer photo-resist stack for interference lithography 70

3.4.3. Nanoimprint lithography 75

3.5 Summary *76*

Chapter 4 Magnetic film deposition and properties 83

4.1 Thin film deposition by RF magnetron sputtering *83*

4.1.1. Example of a complete sputter system 87

4.2 Magnetic thin films with perpendicular anisotropy *89*

4.3 Effect of oxygen partial pressure on the properties of perpendicular CoCrPt films *92*

4.4 Magnetic reversal phenomena in pseudo spin valve films with perpendicular anisotropy *97*

4.4.1. Introduction 97

4.4.2. Experimental Procedures 98

4.4.3. Results and discussion 99

4.5 Conclusions *103*

Chapter 5 Magnetic dot arrays 107

5.1 Introduction *107*

5.2 Methods for etching materials *108*

5.2.1. Introduction 108

5.3 Patterning perpendicular magnetic films using PS-PFS block copolymer as a mask *112*

5.3.1. Material choice for block copolymer lithography pattern formation 112

5.3.2. Preparation of block copolymer thin films 114

5.3.3. Effect of molecular weight on the microphase segregation of PS-PFS 117

5.3.4. Fabrication of islands with perpendicular magnetic anisotropy using BCP lithography 119

5.4 Magnetic properties of arrays of islands with perpendicular magnetic anisotropy *124*

5.5 Conclusion *128*

Chapter 6 Directed self assembly of block copolymers 133

6.1 Directed self-assembly of block copolymers using selectively removable topographic templates *134*

6.1.1. Introduction 134

6.1.2. Fabrication of selectively removable templates using interference lithography 136

6.1.3. Directed assembly of PS-PFS in selectively removable templates 137

6.1.4. Pattern transfer of ordered arrays into functional materials 140

6.2 Nanoimprint lithography with in-situ annealing *144*
6.3 Mask fabrication by interference lithography *146*
6.3.1. Mold treatment with release layer 147
6.4 Directed assembly of PS-PFS under coated silicon molds *149*
6.5 Conclusions *155*
Chapter 7 Conclusions and recommendations for future work **158**
7.1 Conclusions *158*
7.2 Future work *161*

List of figures

Figure 2-1: Schematic of a conventional longitudinal hard-drive medium. An exchange-decoupled polycrystalline film stores the information as a net magnetization direction in a region of the film called a bit cell. The bit has a jagged edge which gives rise to noise in the read-back signal. After[2]. 28

Figure 2-2: Schematic of a bit-patterned media. Series of close-packed islands are arranged in tracks; each island has an easy axis perpendicular to the sample plane. 30

Figure 2-3: Schematic of the writing of a single bit by a fringing field from a pole head. Short elements are favored as during writing as neighboring cells are unaffected by the write field. Tall elements would be exposed to significant fields reducing their stability and resulting in write errors. 31

Figure 2-4: Simplified overview of control circuitry of a vibrating sample magnetometer. 35

Figure 2-5: Simplified schematic of operating circuitry of an alternating gradient field magnetometer. 37

Figure 2-6: Energy states of a Stoner-Wohlfarth particle at zero and non-zero field. 39

Figure 2-7: Definition of θ and φ. 40

Figure 2-8: Ideal hysteresis curves for a single Stoner-Wohlfarth particle. 41

Figure 2-9: Typical setup of the cantilever and the optics of a scanning probe microscope. An x, y, z stage for sample positioning is common, as well a piezo-driven mount for scanning (and driving) the cantilever. The optical setup is also shown where a laser beam is reflected off the backside of the cantilever and onto a photodetector array sensitive to minute cantilever displacements. 44

Figure 2-10: Interleave mode of AM-SPM. The instrument first measures the topography by tapping the surface with the probe (panel a), then lifts the probe and retraces the topography offset vertically by a set distance (panel b) while measuring phase changes. The second (interleaved) scan only registers the magnetic contribution. Panel c) shows the topographic image of a magnetic recording tape used for calibration, and panel d) only the magnetic image of the same area showing a track edge. Scan width is 5 × 5 µm. 47

Figure 2-11: Separation of topography and magnetism by combining a constant height and constant frequency shift taken very close to the sample. Panel a) shows a convolution between the van der Waals and magnetic forces measured at a fixed distance. Panel b) only shows a true topographic measurement.[47] 48

Figure 3-1: Top view SEM showing multiple "grains" of ordered polymer microdomains. The average width of each domain expressed in number of periods is the correlation length. 55

Figure 3-2: Theoretical block-copolymer phase diagram and corresponding morphologies. S – spherical, C – cylindrical, G-gyroid, L-lamellar. After [15]. 56

Figure 3-3: Orientation of a lamellar phase diblock copolymer on a surface: left, the surface has preferential wetting to one of the block, right, a neutral surface has no preference to the wetting of the blocks. 58

Figure 3-4: a) top view schematic of a self-assembled block copolymer in lamellar morphology on a neutral surface, b) same but assembled on a chemically patterned surface, the lamellae follow the chemical pattern on the surface c) cross-sectional view, the different colors represent different surface chemistries. 62

Figure 3-5: Schematic of a disordered spherical morphology thin film block copolymer and the same guided by a topographic template. The ordering is improved near the edge of the template. 63

Figure 3-6: Naito's process for image reversal and pattern transfer from a self-assembled block copolymer pattern[18]. 67

Figure 3-7: A schematic of the Lloyd's mirror interferometer lithography tool. The beam from a HeCd laser with wavelength of 325 nm is spatially filtered and allowed to expand for 2 meters. There the beam is incident on a mirror and substrate which are mounted on a rotation stage for easy adjustment of the fringe period. After Walsh[66]. 69

Figure 3-8: Left, optimized tri-layer stack for fabricating 400 nm period grating using interference lithography. Thickness and complex refractive index is shown for each layer. Right, a typical output of the computerized algorithm for optimizing the ARC thickness shown on left. Reflectivity at the resist/silica interface is shown as a function of ARC thickness. 71

Figure 3-9: The pattern transfer of the tri-layer stack for interference lithography. After exposure and development, the photo-resist lines are transferred into the oxide layer using CF_4 RIE (second row), and lastly the pattern is transferred in ARC using He/O_2 RIE (bottom row). The slightly rough-looking bottoms of the trenches are due to ARC residue remaining that was cleared by a short He/O_2 RIE step. The resulting lines can now be transferred into the substrate or further processed. This is the basic IL / pattern transfer process used throughout this thesis. 74

Figure 3-10: Simplified comparison of imprint lithography techniques. Pattern transfers for lift-off are also possible. After [74]. 75

Figure 4-1: Schematic of a basic RF sputtering system. For DC sputtering the RF generator and matching network are replaced by a DC power generator. 84

Figure 4-2: Steady-state voltage distribution in unequal area electrode RF powered system as compared to equal area electrode system. The target (source) would be placed on the left electrode and the substrate on the right. After Plummer[2] and Campbell [3] 85

Figure 4-3: Planar magnetron sputtering system. The permanent magnets arranged circularly underneath the target create a curling field that concentrates the ion bombardment along a circular "track" between the magnets. 86

Figure 4-4: Schematic of a complete sputter system with a load-lock and a residual gas analyzer (RGA) capable of measuring gas composition during deposition. Three targets (2 shown for clarity) deposit in a sputter-up position, on a sample which is mounted on a rotating stage. 87

Figure 4-5: Schematic of the Ti/CoCrPt film grown on a Si substrate. Arrows show the perpendicular alignment of the crystalline c-axis of cobalt which is the easy magnetocrystalline direction..89

Figure 4-6: AFM / MFM images of the surface of 5 nm Ti / 15 nm CoCrPt film, left: height data showing the surface of the film, vertical scale 10 nm, right: phase image during interleave mode showing maze-like domain structures of AC-demagnetized sample, vertical scale is 2 degrees. Scan size is 5 × 5 μm..91

Figure 4-7: Hysteresis curves of Ti/CoCrPt films deposited in pure Ar atmosphere, and 0.25% and 0.5% oxygen..94

Figure 4-8: Hysteresis curves of Ti/CoCrPt films deposited in Ar atmosphere mixed with 0.75% - 2% oxygen. 95

Figure 4-9: Summary figure of the deposition growth. Films deposited with oxygen concentration lower than 0.5% grow with the anisotropy axes perpendicular to the plane while those grown above 1.25% with clear in-plane anisotropy. 96

Figure 4-10: Major and minor hysteresis loops of a perpendicular PSV sample. Loops starting at the plateau B demonstrate the cycling of the thin (5nm) CoCrPt layer. Time dependent switching seen in the minor loops starting at regions A and C are attributed to domain growth. 98

Figure 4-11: The rate of change of magnetization at a given reverse field in the range of 55 – 420 Oe, applied after saturation. When the reverse field is within either of the steps in the major loop, a time-dependent magnetization is observed. The inset shows the reversal rate as a function of applied field. 99

Figure 4-12: a) a large single domain (north) may expand by moving the domain wall, sometimes leaving behind a 'bubble' domain, depicted in b) which are magnetostatically stabilized and require high fields to annihilate. 100

Figure 4-13: MFM images taken at remanence with a net zero moment of the sample (equal amount of 'up' and 'down' domains). For a) the sample was first saturated, then a reverse field of 355 Oe was applied for 30 seconds. b) a short-duration higher field (435 Oe for 200ms) was

applied. Image area is 10×10μm, phase height is 7 degrees, light gray regions correspond to reversed domains. Notice the finer domain wall structure present in case b)........ 101

Figure 5-1: Chemical structure of polystyrene-b-polyferrocenyldimethylsilane (PS PFS). 112

Figure 5-2: Schematic of the arrangement of the polymer chains of PS-PFS at the surface of silica. The PFS preferentially wets the silica surface, and as a minority phase microphase segregates into spheres embedded in a polystyrene matrix. 113

Figure 5-3: A typical spin curve of PS-PFS solution in toluene. 113

Figure 5-4: Effect of film thickness on the morphology of the self assembled PS-PFS 47/15 block copolymer. 1% solution was spin cast at: a) 750 rpm, b) 1000 rpm, c) 1500 rpm, d) 2000 rpm, e) 2500 rpm and f) 3000 rpm........116

Figure 5-5: Top view micrographs of different molecular weight PS-PFS morphologies on a flat surface: a) 69/21 PS-PFS and b) 33/10. Note the different length scale........ 118

Figure 5-6: Schematic of the pattern formation and transfer process. a) the starting multilayer, which is annealed to induce microphase segregation in the block copolymer; b) monolayer of PFS domains embedded in PS matrix forms; reactive ion etching is used to form and transfer the pattern from b) through e) and ion beam etching transfers the pattern into the magnetic layer f). 119

Figure 5-7: Tilted-view scanning electron micrographs at different steps of the pattern transfer. a) PFS spheres on silica surface exposed by RIE, b) silica pillars formed by RIE, c) tungsten caps formed by RIE, d) finished sample by ion milling into the magnetic layer. 120

Figure 5-8: Magnetization and coercivity of sample A-15 as a function of ion beam etching time. At short times, partial etching roughens the surface of the magnetic film, the coercivity is increased slightly and the total moment of the sample is reduced as a result of magnetic material being etched away. Further etching fully transfers the pattern into the magnetic film, which is accompanied by a sharp jump in the coercivity. At this point the magnetic islands are physically and magnetically separated from each other. Further ion etching results in pattern degradation by side-wall erosion of the islands accompanied by lowering of the total moment, while the coercivity remains roughly constant. 124

Figure 5-9: Coercivity of unpatterned film, as well as patterned samples. Islands in set A have an average diameters of 34 nm, while those in set B have an average diameters of 28 nm........ 125

Figure 5-10: Switching volume V* as measured for arrays of uniaxial islands fabricated by block-copolymer lithography. 125

Figure 5-11: V* measured by following the analysis of Wohlfarth[21] for sample B-15. 126

Figure 5-12: Results of micro-magnetic simulation showing coherent and independent reversal of a single island. Inset shows two consecutive stages in the simulation at field difference of 10 Oe. Bottom right shows the top-down view, where a single island can be seen reversing the magnetization abruptly (black islands have the magnetization pointing towards the reader, and white away from the reader). The gray horizontal line depicts the location of the cross-section shown in top-left, where all magnetization vectors are aligned with the vertical c-axis. The varying cell-colors depict the angle of the vector in the basal (substrate) plane consistent with the slight variation of the c-axis programmed into the simulation. 127

Figure 6-1: A non-removable topographic template used for ordering the microdomains of a block copolymer will transfer into the underlying layers ultimately forming magnetic stripes next to magnetic islands which could have undesirable magnetic interactions. 134

Figure 6-2: Schematic of the process flow for fabrication of selectively removable templates using interference lithography (not to scale). 135

Figure 6-3: a) pattern transferred into the ARC layer, other layers visible (from bottom upwards: dark band on bottom is substrate, brighter band is the Ti/CoCrPt/W layers, medium gray is silica hard mask, layer with spots is the ARC removable template, and a thin silica interlayer is between the free-standing ARC grating and removable template. c) a 500 nm period grating on silicon substrate. 136

Figure 6-4: Block copolymer solution spin-coated on a grating of a selectively removable template. 137

Figure 6-5: Scanning electron micrograph of the guided assembly of PS-PFS in selectively removable template. Polymer forms 14 rows in the groove which is 370 nm wide. 139

Figure 6-6: Scanning electron micrograph of the guided assembly of PS-PFS in selectively removable template. Polymer forms 7 rows in the groove which is 180 nm wide. 139

Figure 6-7: Guided self assembly of 47/15 in 250 nm period grooves made of selectively removable material. 140

Figure 6-8: Pattern transfer into silica hard mask. a) partially transferred block copolymer pattern into the silica layer – silica pillars are being formed and trenching is visible where the template used to be. b) full pattern transfer into the oxide, free-standing oxide pillars have been formed and the area beneath the removable template is void of material. 142

Figure 6-9: Block copolymer ordered patterns by selectively-removable template transferred into tungsten forming a well-ordered array of islands with 17 nm diameter. 143

Figure 6-10: Pattern transferred into CoCrPt using ion beam etching. 143

Figure 6-11: Schematic of the process steps in guided self-assembly of block copolymers by nanoimprint lithography and in-situ annealing. 145

Figure 6-12: Schematic of the nanoimprint press for in-situ annealing. 146
Figure 6-13: Silicon etch depth as a function of etch time in CF_4 RIE, bias 50V, power 70W. Effective etch rate is 10.4nm/min. 147
Figure 6-14: SEM micrograph of a 250nm period grating with groove depth of 90 nm. 148
Figure 6-15: Imprinted pattern into PS-PFS, left without the use of a release layer on the mold, right, with release layer. 148
Figure 6-16: Mold was grating with 400nm period, a) 45nm deep mold, b) 55nm deep mold, c) 65 nm deep mold. All polymer was 47/15 spun at 45nm thickness. 149
Figure 6-17: Mold was 400 nm period, 45 nm deep grating. Polymer was 33/10 spun to a) 26 nm, b) 32 nm. 150
Figure 6-18: Mold was 1μm period, 65nm deep; polymer was 47/15 spun to a) 47nm, b) 42 nm, c) 38 nm, d) 36 nm. 151
Figure 6-19: Flow of polymer during nanoimprinting. 152
Figure 6-20: Mold was 55nm deep, 1 μm period grating. Polymer was 47/15 spun at a) 54 nm, b) 42 nm, c) 36 nm, d) 32 nm, e) 29 nm, d) 26 nm. Samples a-d were annealed at 150° C, and e-f were annealed at 175° C. 154
Figure 6-21: Mold was 1μm period, 55 nm deep grating; Polymer was 33/10 spun to a) 32nm, b)29 nm, c) 26 nm, d) 23 nm. 155

List of tables

Table 5-1: Molecular weight, size and correlation length of PS-PFS used in this work. 117

Acknowledgements

In the last nine years I've had the honor to work in a great institution and there have been many people that have made this experience so much better. Foremost, I would like to thank my advisor, Professor Caroline Ross who provided me with great guidance throughout my graduate (and undergraduate) work while encouraging me to try research directions that were interesting to me. She is a terrific academic advisor – the best I could have hoped for. Professors Hank Smith and Karl Berggren have been an invaluable resource, providing both fruitful discussions and resources with the NanoStructures Lab. I'm also grateful for the support from my thesis committee members Professors Ned Thomas and Carl Thompson, as well as Professor Marc Baldo for the UHV AFM facility.

While we all take our fair share of classes, I believe that having the opportunity to be elbow-deep in all the experiments in the laboratory and sharing the labs with a great research group has been the source of the most important lessons I learned in (the art of) science. It has been a privilege to work with such a great researchers and I appreciate Dr. Joy Cheng, Dr. Fernando Castaño, Dr. Tamar Tepper, Dr. Wonjoon Jung, Dr. Vikram Sivakumar, Vivian Chuang, Brian Ng, Lei Bi, Yeon Sik Jung, Gabrielle Joseph and other members past and present of the Magnetic Materials and Devices group for sharing their lives and work with me. My UROP students Joy Perkinson and Megan Tsai have both been a source of help and lessons. CMSE and NSL staff has made many experiments possible, and I am thankful to Libby Shaw and Jim Daley for their dedication.

My family, while geographically far, has always been close to me. Six time-zones away has never been an issue for my parents Svetlana and Mihailo and my sister Ana to form a great pillar of support without which this journey certainly would neither have started nor progressed to this point. I hope that the friendships that I've formed at MIT will last a lifetime, and it has been lots of fun spending time with Damian, Matt, Tamam, Apara, Borjan, Elizabeta and so many others. Finally, I lack enough words to express my admiration and gratefulness for Adriana Tajonar, the person that has celebrated with me in my highs and pushed me through the lows for all her patience and love.

The most exciting phrase to hear in science, the one that heralds new discoveries, is not 'Eureka!' but 'That's funny...'
Isaac Asimov (1920-1992)

Chapter 1

Motivation and scope

1.1 Introduction

In the last decade we have seen a large proliferation of technologies which heavily reinforce our dependence on data storage. Historically, hand painting and writing were the methods of archiving data for five millennia, before Gutenberg invented the printing press. Today, information is no longer just written word transferred into stone or on paper, but also music, video and image archives are increasingly more important. A 2003 University of California at Berkeley study estimated that 5 billion GB (gigabytes) of information was produced in 2002 alone out of which 92% was stored on magnetic hard drives. Whether hard drives enabled this explosion or are a result of the need to store the vast amounts of data is debatable, but the need to store larger amounts of data is evident.

More than forty years ago G. Moore put forward his observations of the doubling of the number of transistors in integrated circuits each year[1]. Ever since, the so-called

Moore's law has been the direction that the semiconductor industry has taken, and effectively has been the driving force behind the technological and ultimately social revolution that began at the end of the last century and continues today. We have seen an explosion of technologies in all spheres of our lives and a large proliferation of devices that 20 years ago might have been in the realm of fiction are reality today. Devices such as portable music players capable of storing thousands of songs, small-form digital cameras able to take high-quality photographs etc. are ubiquitous today. The need to store large amounts of digital information has grown proportionally and an analogue to Moore's law has emerged which states that not only the data density has doubled per annum, but the cost per unit information has steadily decreased as well[2].

Current top-of the line commercially available hard-drives have recently switched over to perpendicular media and already report 130 Gb/in^2 data density (Seagate, 2008). The increases in data density, read-rate and performance have been generally enabled by parallel scaling of the medium and the read-write head. This progress unfortunately cannot continue at the same rate for much longer as the theoretical limits of the technology will be reached in the next 5 years. A conceptual change in the design of the hard drive media will have to be undertaken in order to continue the expected increase in data density.

A variety of other devices, from DNA-sorting devices to plasmon waveguides require a well controlled nano-scaled periodic pattern that might cover a relatively large area. From a manufacturing point of view, the areal throughput largely determines the price of such devices and consequently their feasibility[3]. While methods such as electron-beam lithography[4, 5], dip-pen lithography[6] and atom manipulation by scanning tunneling microscope[7] possess the necessary resolution, the serial nature of

the pattern formation is the high price paid for such a precision. Conventional photolithography which relies on the exposure of a photosensitive layer by photons is extremely fast, but limited in the resolution of features due to diffraction. Using shorter wavelength (deep-UV and x-ray) to achieve better resolution is hindered by the lack of readily available brilliant light sources at those wavelengths [8-10]. Even as such sources become available, other problems such as line edge roughness and critical dimension control might hinder further shrinking of features that could be patterned. Nanoimprint lithography[11] has the required throughput and resolution, but the problem of fabricating an expensive master remains a problem.

We believe that block copolymer lithography can answer a lot of the problems outlined above, especially if combined with a top-down method utilizing the registration precision of conventional lithography methods with the self-healing high-throughput benefits of block copolymer lithography. Therefore we set out to examine the technological challenges in using a self-assembled block copolymer mask to pattern magnetic films with perpendicular anisotropy. Once fabricated, the magnetic properties of large-area nanoscaled magnetic assemblies are interesting to study both for fundamental understanding of nanosized elements and to provide guideline information on future devices. Lastly, we wanted to develop a method of transferring solely the pattern formed by templated polymer microdomains without transferring the template used for guiding the self-assembly of the block-copolymer.

1.2 Contents of this thesis

The goal of this work was to fabricate and analyze a magnetic dot array applicable as a bit-patterned medium. Chapter 2 summarizes the current state of the technology for

magnetic recording, including a brief background information on magnetism of small particles, and magnetic characterization techniques. Chapter 3 introduces the lithography methods using block copolymers, as well as the pattern transfer methods used throughout this thesis. Chapter 4 covers the growth and analysis of magnetic films with perpendicular magnetic anisotropy. In Chapter 5 we present the work on using block copolymer lithography to pattern perpendicular magnetic films, and the magnetic characterization of the fabricated arrays. Chapter 6 covers two methods of imposing long range order to the block copolymer pattern and finally Chapter 7 gives general conclusions, and proposed future exploration.

References

[1] G. E. Moore, "Cramming more components onto integrated circuits," *Electronics*, vol. 38, 1965.

[2] C. Walter, "Kryder's Law," *Scientific American*, vol. 293, pp. 32, 2005.

[3] G. L. Timp, *Nanotechnology*. New York: AIP Press, 1999.

[4] H. C. Pfeiffer, "Recent advances in electron-beam lithography for the high-volume production of VLSI devices," *IEEE Transactions on Electron Devices*, vol. ED-26, pp. 663, 1979.

[5] R. F. M. Thornley and M. Hatzakis, "Electron-optical fabrication of solid-state devices," Berkeley, CA, 1967.

[6] R. D. Piner, Z. Jin, X. Feng, H. Seunghun, and C. A. Mirkin, ""Dip-pen" nanolithography," *Science*, vol. 283, pp. 661, 1999.

[7] L. J. Whitman, J. A. Stroscio, R. A. Dragoset, and R. J. Celotta, "Manipulation of adsorbed atoms and creation of new structures on room-temperature surfaces with a scanning tunneling microscope," *Science*, vol. 251, pp. 1206, 1991.

[8] H. I. Smith, D. J. D. Carter, M. Meinhold, E. E. Moon, M. H. Lim, J. Ferrera, M. Walsh, D. Gil, and R. Menon, "Soft x-rays for deep sub-100 nm lithography, with and without masks," *Microelectronic Engineering*, vol. 53, pp. 77, 2000.

[9] H. I. Smith and D. C. Flanders, "X-ray lithography-a review and assessment of future applications," New York, NY, USA, 1980.

[10] U. Stamm, R. Paetzel, I. Bragin, V. Berger, I. Klaft, J. Kleinschmidt, R. Osmanov, T. Schroeder, K. Vogler, W. Zschocke, and D. Basting, "High repetition rate excimer lasers for DUV lithography," *Proceedings of SPIE - The International Society for Optical Engineering*, vol. 3679, pp. 1050, 1999.

[11] S. Y. Chou, P. R. Krauss, W. Zhang, L. Guo, and L. Zhuang, "Sub-10 nm imprint lithography and applications," *Journal of Vacuum Science & Technology B: Microelectronics Processing and Phenomena*, vol. 15, pp. 2897, 1997.

Chapter 2
Magnetic media and magnetic characterization

This chapter covers the current state of the continuous media hard drive technology, including lithographic and magnetic requirements of bit-patterned media. A background on magnetism relevant to this thesis is presented, with focus on time dependent magnetization properties of arrays of magnetic particles with uniaxial anisotropy, as well as an introduction to standard magnetometry methods widely used throughout this work.

2.1 Continuous-media hard drive technology

Modern hard disk media consists of a plate (or disc) of glass or aluminum alloy which has been sputter-coated with a multilayer thin film. Several layers are often deposited, such as underlayers, seed layer, data layer and capping layers. The data layer is most commonly made of an alloy of CoCrPt, with some additional elements, such as B

and Ta added as well to promote intergranular magnetic isolation[1]. The deposited film is polycrystalline and is sputter-deposited at elevated temperatures to promote the segregation of the non-magnetic elements into the grain boundaries. The grain boundaries can partially 'isolate' or exchange-decouple neighboring grains and therefore, each grain behaves similarly to a as a single-domain particle. For longitudinal media, during recording a magnetic head magnetizes a region (called a bit-cell) in the film parallel or antiparallel to the track direction. The read-back is achieved by detecting the fringe fields between neighboring bit-cells by using the read-head (Figure 2-1). Perpendicular media employs the same general methodology, except the bits are magnetized out-of-plane.

High density media stores one bit of information over an area roughly equal to 100 grains. As each bit is not perfectly rectangular, noise arises from this jaggedness that dominates the overall signal-to-noise ratio. If the bit sizes are reduced to increase the data density, so must the grain size as well in order to avoid increasing the noise of the system. However, this scaling method cannot continue indefinitely, as thermal energy (k_bT – Boltzmann constant times temperature) becomes sufficient to overcome the magnetic energy of the grain (KV – magnetocrystalline anisotropy times grain volume) and the grains

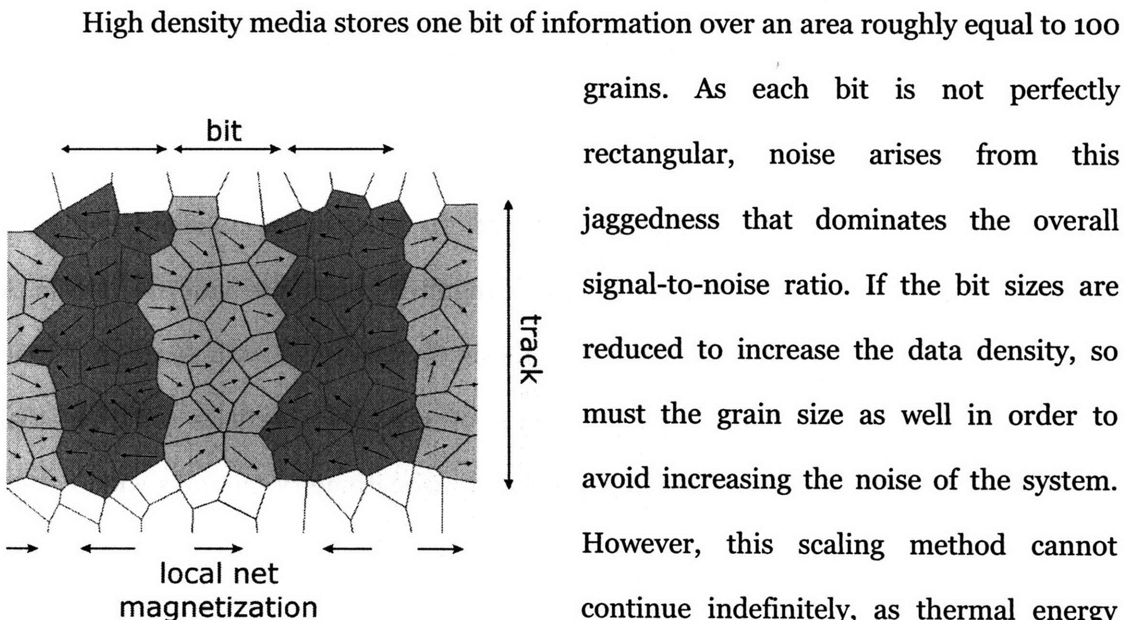

Figure 2-1: Schematic of a conventional longitudinal hard-drive medium. An exchange-decoupled polycrystalline film stores the information as a net magnetization direction in a region of the film called a bit cell. The bit has a jagged edge which gives rise to noise in the read-back signal. After[2].

become superparamagnetic. To keep the information stored on the hard-drive for a significant amount of time, the ratio KV/k_bT must be larger than 40[1]. As the volume of the grains is reduced, the only way to keep this ratio from reducing is to increase the anisotropy, but this approach cannot be extended far, as the larger K-value materials require higher write fields which are unfeasible in write-heads which have a limit of about 5000 Oe[2] at which point the writing pole is fully saturated[3]. Substituting the pole material to achieve higher write-fields is not possible due to the unavailability of materials with higher saturation magnetization. As a result, several methods have been examined to circumvent this limitation in the scaling processes of hard drive technology.

2.2 Approaches to increasing the data density of hard drives

To increase the thermal stability of smaller grains, films with larger magnetic anisotropy values must be used. However, in order to be able to write the data, the coercive field of the film must be reduced to values less than 5000 Oe (maximum field achievable by the write head). As a result, recent research has been aimed toward thermally-assisted writing [4] where a laser locally heats the area during the write cycle of the head. For this application, even larger-anisotropy materials can be used, such as ordered (Co, Fe) (Pd, Pt) compounds or rare earth-transition metal alloys. Another approach to increasing the data density is the use of patterned media.

The concept of patterned media[2, 5-7] (also called bit patterned media or discrete media) consists of a periodic array of magnetic elements, each with parallel uniaxial anisotropy. A possible arrangement is schematically presented in Figure 2-2. Series of islands are arranged in tracks, similar to the arrangement of data in conventional media.

---

[1] This stability criterion assumes that 95% of the stored information will be unaffected for 10 years from the moment of data-writing, a standard widely accepted by the hard-drive industry.

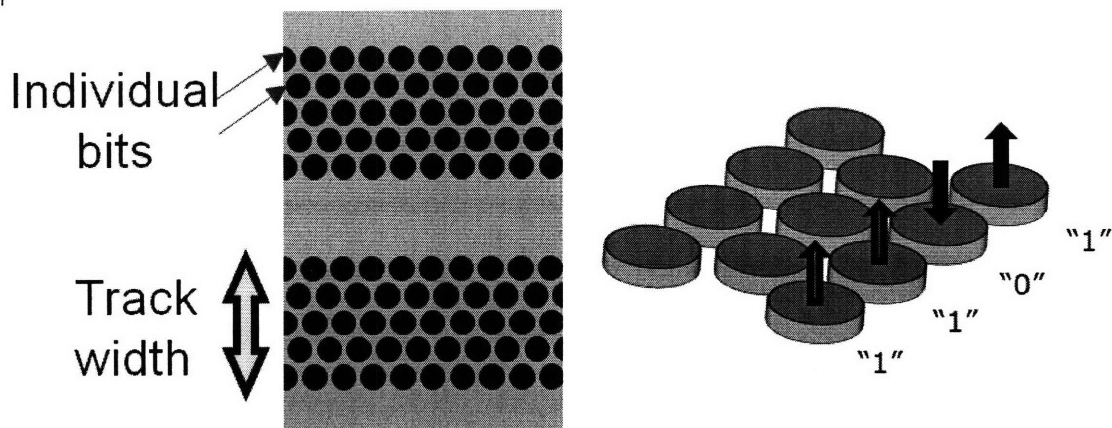

Figure 2-2: Schematic of a bit-patterned media. Series of close-packed islands are arranged in tracks; each island has an easy axis perpendicular to the sample plane.

Each island has an easy magnetization axis perpendicular to the plane of the film, and would store one bit of information. The medium is incorporated in a spinning disc, and an ultra-narrow head reads and writes the information by magnetizing individual elements.

For such a medium to be viable, it must provide improved performance at a cost comparable or lower than current technology. Ignoring other performance benchmarks, if we are simply driven the data density, such a technology must provide equal or higher densities than are achievable with conventional media. The limits of longitudinal media have already been reached with densities of roughly 100 Gb/in^2 [8] and perpendicular media is projected to reach its limit around 500 Gb/in^2 [9](some predictions place that number higher at 1000 Gb/in^2 [10]). Bit patterned media must therefore provide densities of 500 Gb/in^2 or higher. At the same time, the cost of fabricating such a device must be kept at a minimum. Such densities imply fabricating periodic patterns with a pitch of 50 nm or less over an area with 2.5 inches in diameter at a reasonable cost (<1$/platter).

2.3 Bit patterned media requirements

In conventional media, the noise that is intrinsic to the system arises from the polycrystalline nature of the deposited film. For patterned media, the argument on noise is very different. To increase the stability of the media, each patterned bit must be a single-domain particle that reverses the magnetization independently of neighboring particles. Grain-boundary isolation is not favored as it would introduce multiple domains per bit, therefore, the magnetic film should be deposited with large magnetic exchange coupling between grains. High density media already employs thin films [11], a requirement that bit-patterned media shares with continuous media[9]. Bits would be written by a fringing field emanating from a single pole head, and to avoid affecting neighboring bits during writing, the patterned bits must be short. The fringing field expands away from the tip of the write head, so closely packed tall elements would be exposed to a large fields possibly resulting in erroneous writing of neighboring cells hindering the ability to bring the bits closer.

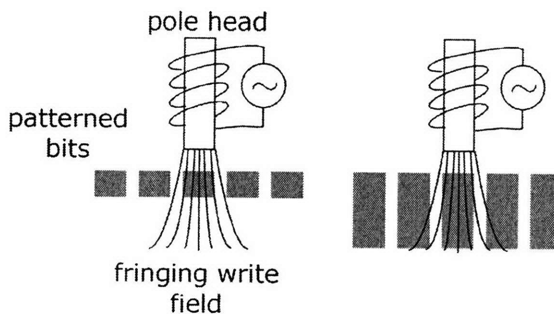

Figure 2-3: Schematic of the writing of a single bit by a fringing field from a pole head. Short elements are favored as during writing as neighboring cells are unaffected by the write field. Tall elements would be exposed to significant fields reducing their stability and resulting in write errors.

The bit placement error will be independent from the writing head and no longer be a result of on the head field, but rather depend entirely on the lithography used to fabricate the patterned medium. Similarly, 'jitter' noise which arises from the jagged edge of a bit written in continuous media hard drives, no longer applies as each bit has pre-defined geometry independent of the

head field. As a result, the source of jitter noise in bit patterned media will solely come from the quality of the lithography. Albrecht *et al.* found that for a case of focused-ion beam fabricated array, the jitter noise was constant and limited by the lithography[12, 13], unlike the track-width dependent jitter noise typical of continuous media. In order for a drive to function within current error tolerances, the placement and position errors must be within $1\sigma = 10\%$ of the patterned bit size [14].

2.4 Magnetic characterization

2.4.1. Introduction

Perhaps the most useful piece of magnetic information – the hysteresis loop – is the first characteristic measured for any magnetic sample. Over the years many instruments and methods have been devised that can determine this and other magnetic properties. The methods generally fall in three categories: (1) measurement of a force exerted on a material by a non-uniform magnetic field, (2) measurement of induction in the vicinity of the material and (3) indirect measurement of phenomena related to or dependent on magnetic properties. From methods that rely on measuring the force exerted by a non-uniform field, by far the most popular today is the alternating gradient field magnetometer (AGFM, or AGM), while methods such as the Faraday balance are now rarely used. Measurement techniques that rely on magnetic induction in the vicinity of the sample are the simple (but highly limited) hysteresis meter (HM), the vibrating sample magnetometer (VSM) and the superconducting quantum interface device magnetometer (SQUID). Lastly, indirect techniques, such as the measurement of the Faraday or Kerr effect, or microwave ferromagnetic resonance can also be utilized to determine magnetic properties of samples. A common instrument for determining magnetic properties is the VSM, and the majority of bulk magnetic measurements

presented in this work have been done on the VSM. Some measurements were also obtained using an AGM and the instrumentation method will be noted where appropriate. Modern magnetometers are capable of determining several types of magnetic information and have quickly replaced other methods that predate them. Bates' book "Modern Magnetism" contains a comprehensive review on these older methods and is quite interesting to read[15].

2.4.2. The vibrating sample magnetometer (VSM)

A. Introduction and basic principles

It was Foner who invented the VSM in 1956 [16]. While inductive measurement methods where either the sample or the pick-up coils were oscillated had been previously reported[17], it was Foner's design of the pick-up coils, and oscillating mechanism that has proven most effective. This early design has been further developed and improved upon, especially in the method of control by the incorporation of modern electronics and computers.

The basis of the VSM is the familiar Faraday's law of electromagnetic induction:

$$\varepsilon = -N\frac{d\Phi_B}{dt}$$

where ε is the induced electromotive force (voltage) in a coil with N turns where $\frac{d\Phi_B}{dt}$ is the time-varying change in magnetic flux. A magnetic sample is held on a rod (Figure 2-4) which vibrates the sample in front of a set of pick-up coils. The induced *emf* in the pick-up coils is proportional to the sample magnetization and can be calibrated by a reference sample. The hysteresis loop is plotted by measuring this moment as a function of applied field. A uniform field is applied by a set of coils with a ferromagnetic core

which concentrates and amplifies the field. The pick-up coils are insensitive to this uniform magnetic field, as there is no time-varying component to it.

B. *Instrumental considerations*

The magnetic field is generated by a DC bipolar power supply passing current though a set of coils that are continuously cooled by closed-circuit chilled water. The magnetic field is measured by a Hall-effect device in a feedback loop with the power supply and controlled by a computer. The field is continuously monitored by the computer and the current in the coils is adjusted appropriately to maintain a stable field.

To be able to measure small moment samples, the voltage induced in the pick-up coils is amplified by a voltage amplifier. If this signal were to be directly used as a reference signal, large errors and noise would be present in the measurement. Therefore, a signal lock-in takes in as a reference the signal in the vibrating assembly and only processes induced voltages that correspond to the physical movement of the sample.

Background signals are typically characterized as random or time-varying and "offset" (typically time-independent) signals. The time-varying noise typically arises from electronic noise induced in lead-wires and is minimized by good electronic shielding. Whatever noise cannot be eliminated by this method is typically averaged over by repeating the measurement at each point as much as long-term signal stability and drift will permit. Offset signals arise from magnetic signals from the rod, substrate or a combination of both. These are typically eliminated by first performing a measurement without the sample and subtracting the data from the final measurement with the sample. To the extent that the measurements are reproducible and significant drift does not occur during repeated measurements, the background signals can easily be cancelled out.

The VSM used for this research was made by ADE Magnetics (previously Digital Measurement Systems) and recently acquired by KLA-Tencor[18]. It has a model 1660 signal processor, can continuously heat/cool the sample from 100 – 1000 °K and can automatically rotate the sample for angle-dependent measurements. The maximum applied field is 1.35 T, and the system is sensitive so signals as low as 10^{-6} emu.

2.4.3. The Alternating Gradient Field Magnetometer

A. Introduction and Basic Principles

Unlike the VSM which relies on measuring the induced coltage in the pickup coils placed in the vicinity of the sample, the alternating gradient field magnetometer (AGM)

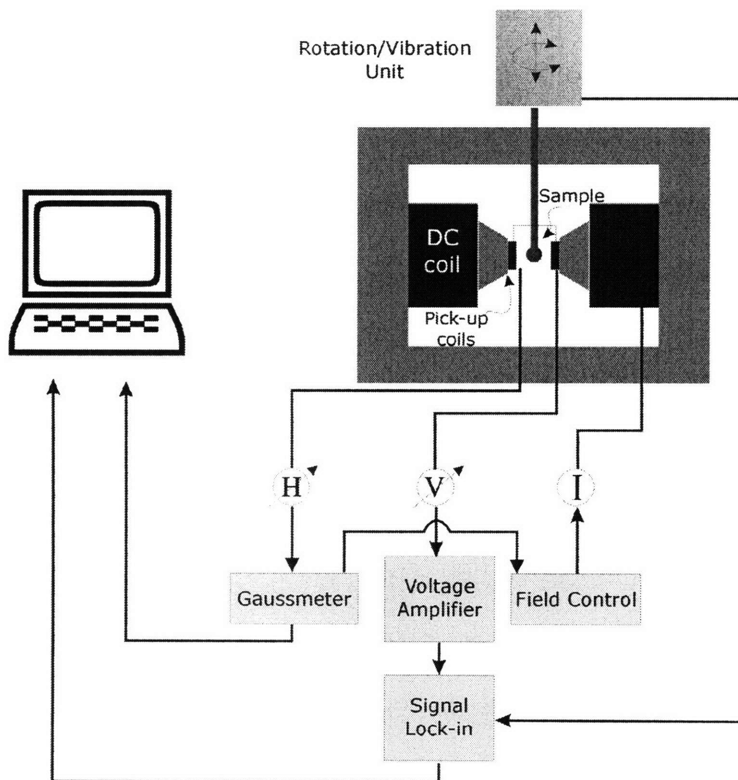

Figure 2-4: Simplified overview of control circuitry of a vibrating sample magnetometer.

relies on detecting the force exerted on the sample by a non-uniform field. The first description of this method for measuring a full hysteresis loop is the method proposed by Zijlstra in 1970[19]. Zijlstra mounted a small magnetic particle (few microns in diameter) on a flexible reed. Then an alternating field was applied with a frequency close to the natural acoustic resonant frequency of the reed. The deflection was observed under a microscope and a stroboscopic light. Zijlstra was able to step the field and measure a full hysteresis loop in this manner.

The modern AGM uses an alternating gradient field to exert a periodic force on a sample placed in a magnetic field. The force exerted is proportional to the magnitude of the gradient field and the magnetic moment of the sample. To enable the detection of this force, the sample is mounted on a piezoelectric element which builds up a voltage as a response to the applied stress. As a consequence, this output voltage is proportional to the gradient field and magnetic moment of the sample. To maximize the signal, the entire assembly is operated at or near the natural resonant frequency[20]. The AGM used in this research is a Princeton Measurements Model 2900 Alternating Field Gradient Magnetometer.

B. *Instrumental Considerations*

The circuitry controlling the DC applied field is equivalent to the circuitry in the VSM. The difference in the AGM appears in the method of acquiring data on the moment of the sample. Unlike the VSM, the AGM does not possess pick-up coils. Gradient field coils that apply an alternating gradient field superimposed over the DC field are located in the same place where pick-up coils are and are driven at the resonant frequency of the complete assembly (probe and sample). This frequency is automatically determined by the computer which instructs the reference oscillator to drive the coils at this frequency.

The periodic force acting on the probe is translated into a periodic voltage differential across the piezo element and this voltage is amplified and tuned to the original reference signal and returned to the computer for processing. This circuit has been optimized for noise and sensitivity and is capable of detecting moments as low as 1×10^{-8} emu. To further stress the sensitivity, it should be noted that the amplitude of vibration of the assembly is in the range of several nanometers to a few microns. Also, it important to note that the instrument is somewhat sensitive to physical vibration (as much as the probe is vibration-isolated from the instrument) and therefore loud noises must be avoided during data acquisition.

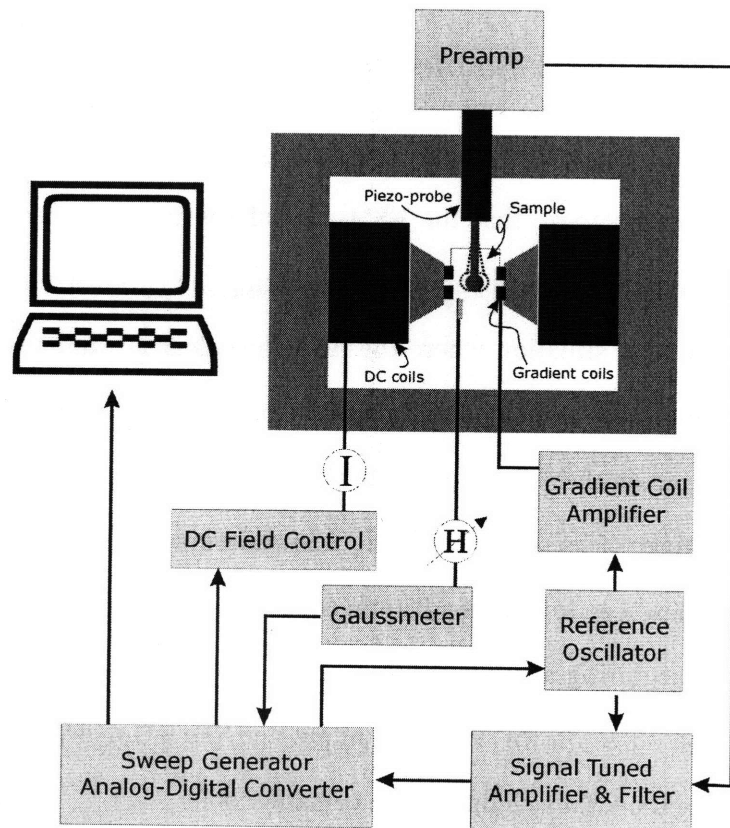

Figure 2-5: Simplified schematic of operating circuitry of an alternating gradient field magnetometer.

The gradient field typically has several ranges, with the largest range being 15 Oe/mm and stepping down over 3 decades to 150 mOe/mm. Since the detected signal is proportional to this gradient, it is reasonable that the largest gradient gives the largest signal to noise ratio and is the range where the quoted sensitivity of 1×10^{-8} emu can be achieved. This range, however, is not practical for very soft samples or measuring true remanence as the field oscillation necessary for the measurement can be demagnetizing very soft samples and falsely under-reporting remanence values. When measuring samples with low coercivities it is therefore necessary to reduce the gradient as to avoid such demagnetizing problems. This results in a reduced signal to noise ratio that is typically solved by increasing the data acquisition time[20].

2.4.4. Comparison of the magnetometry instrumental techniques

While the AGM has a theoretical sensitivity which is lower than the one of the VSM, the physical sample size that the VSM can take is 10-100 times larger than the sample that the AGM can measure, effectively equating the two instruments in terms of the sensitivity. The only situation where the AGM has clear advantage is with samples that have both a small area and small moment. The particular engineering solution to the heating/cooling setup on the VSM is easier to use than the cryostat on the AGM which in turn has the advantage of being able to achieve lower temperatures. Lastly, the speed of data acquirement has been touted as advantageous on the AGM, but from experience the time required for acquiring a full measurement is comparable between the tools. The automated rotation stage on the VSM is unique and the AGM does not possess such capabilities making the VSM a slightly more versatile tool.

2.5 Sweep rate dependent magnetic reversal measurements

2.5.1. Small particle magnetism

In hard-drives, information stored as a magnetization direction in a finite number of small magnetically isolated particles. The magnetic behavior of such fine structures has been of interest for several decades, long before hard-drives were practical devices. Early work by Stoner and Wohlfarth[21] in 1948, Néel [22] in 1949 and Brown [23, 24] in 1959 set forward the foundations of the theoretical understanding of small particle magnetism. Sharrock[25], Bruno[26], Weller and Moser[27] and other further developed the theory with applications to hard drives.

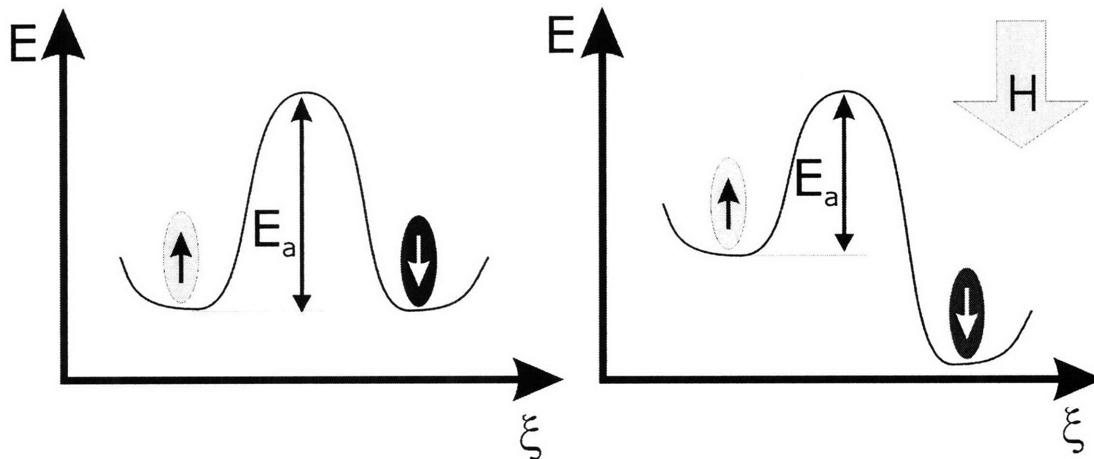

Figure 2-6: Energy states of a Stoner-Wohlfarth particle at zero and non-zero field.

A. Coherent rotation

The most simple case of a single non-interacting Stoner-Wohlfarth particle[21] is particularly illustrative and important to understand. We start with a single particle with uniaxial anisotropy, which would have two magnetic states corresponding to energetic minima in zero external field (Figure 2-6). Those states are separated by an energy barrier E_a. Let us first neglect the effects of finite temperature on the system. Assuming

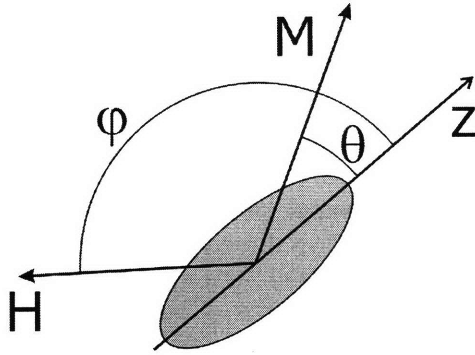

Figure 2-7: Definition of θ and φ.

uniaxial anisotropy and particle size small enough so that non-uniform magnetization states, such as domain walls, curling and canting are avoided, we can ignore all but the Zeeman and the anisotropy energy terms. Then the energy dependence on the external field will be:

$$E(\theta,\varphi) = K_u \cdot V \cdot \sin^2\theta + H \cdot M_S \cdot V \cdot \cos(\theta - \varphi)$$

where V is the particle volume, K is the magnetic anisotropy energy and M_S is the saturation magnetization, and θ and φ describe the orientation of the particle with respect to the applied external field, H. We can approximate this energy barrier E_a to be[27]:

$$E_a^{\pm}(H) \cong K_u \cdot V \cdot \left(1 \mp \frac{H_d}{H_o(\varphi)}\right)^m$$

$$\ldots$$

$$H_o(\varphi) = \frac{2K_u}{M_s} \times \left(\cos^{2/3}\varphi + \sin^{2/3}\varphi\right)^{-3/2}$$

$$m \cong 0.86 + 1.14 \cdot \left(\cos^{2/3}\varphi + \sin^{2/3}\varphi\right)^{-3/2}$$

To better visualize these equations, let us examine them with respect to the hysteresis loop. If the field is applied in the direction of the anisotropy, a perfectly square loop would arise, with a hysteresis field equal to the anisotropy field. If the field were to be applied perpendicular to the axis of anisotropy, the hysteresis curve would be a straight line that saturates after fields higher than the anisotropy field with no coercive field. Discontinuities in the rate of the magnetization arise at h = ±1 (in reduced units of

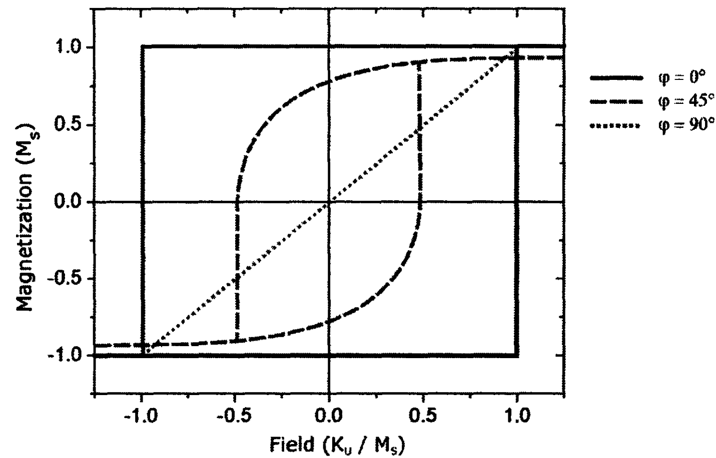

Figure 2-8: Ideal hysteresis curves for a single Stoner-Wohlfarth particle.

K_U/M_S). A field applied at a 45° angle would result in a curving hysteresis curve (Figure 2-8), with a calculated moment of 0.9306 when the reduced field is equal to 1 (in reduced units)[21]. These values were obtained by numerical evaluations, and reference [21] contains tabulated hysteresis behavior for other applied field angles.

B. *Thermally activated reversal*

We have so far neglected temperature, so this treatment would apply to measurements performed at cryogenic temperatures of a single particle. At finite temperatures, the added thermal fluctuations aid the reversal of the particle (Arrhenius –Néel)[22]. If the thermal energy available to the particle (k_bT, k_b is the Boltzmann constant and T is temperature) is equal to or larger than E_a, that particle would be superparamagnetic, meaning that it will behave as a paramagnet and not be able to sustain a remanent magnetization. Particles where this energy barrier is larger than the thermal energy will generally require the aid of an external field to reverse their magnetization for this change to occur in reasonable time scales. We can therefore

analyze the magnetization reversal as an Arrhenius thermally activated process, whose temperature and field dependent time constant is defined as:

$$\tau(T,H) = f_o \exp\left(\frac{E_B(H)}{k_b T}\right)$$

We may write the time-temperature-field dependent magnetization to evolve as follows[27]:

$$M(t,T,H) = M_o\left[2 \cdot P(t,T,H) - 1\right]$$
$$P(t,T,H) = \tau/\tau_- + \left(1 - \tau/\tau_-\right)\exp\left(-\frac{t}{\tau(T,H)}\right)$$

where P is the Maxwell-Boltzmann probability of not switching the magnetization, and τ_- is the reversal switching rate. This is a familiar exponential decay dependence that appears in many processes and M_o is the magnetization at zero time, and M decays exponentially as outlined above. Lastly, the coercivity can be expressed as[25, 26, 28]:

$$H_C(t) = H_o\left\{1 - \left[\frac{k_b T}{KV}\ln(f_o t)\right]^n\right\}$$

where f_o is the thermal attempt frequency, or "jumping rate" of the particle attempting to undergo reversal, with a typical value of 10^9 Hz.

C. *Sweep-rate dependent magnetization reversal*

If we consider an assembly of non-interacting uniaxial particles, we can obtain values of the coercivity of the array by simply averaging over all particles, so the form of the equations is the same as for a single particle. However, if the particles are interacting, the statistics of the reversal described above would be affected and would need to be modified by adding terms which describe reversal mechanism due to interactions. If the particles do not have codirectional anisotropy axes, and are randomly distributed, then

the hysteresis curve would be similar to Figure 2-8 for $\varphi = 45^o$, with remanent magnetization $M_R = ½ M_S$ and coercivity $H_C=0.479(\Delta N)M_S$[21]. Small angle distributions do not change the behavior drastically from the uniaxial case and only result in decrease of the coercive field.

During a regular hysteresis measurement, the field is swept at a certain rate and the moment of the sample is measured. If the measurement is taken at finite temperature, we must consider what thermal effects take place, particularly for the case of an array of small particles. The measured coercivity of the array will have a dependence on the rate at which we apply the field. If the field is applied slowly, some particles will have the opportunity to reverse their magnetization purely from thermal jumping attempts. This would result in a measured coercivity which is lower than coercivity measured with a quickly reversing field[25]. In the case of fast field application, the majority of the reversal will be due to the applied field, and the reversal approaches ideal Stoner-Wohlfarth coherent reversal. The dependence of the coercivity of an array of particles on the rate R at which the field is applied can be expressed as follows[26, 28]:

$$H_C = \frac{k_b T}{V^* M_S}\left\{\ln\left(\frac{\partial H}{\partial t}\right) + \ln\left[\ln(2)\tau_{(H=0)}\frac{V^* M_S}{k_b T}\right]\right\}, or$$

$$H_C = \frac{k_b T}{V^* M_S}\left\{\ln(R) + const.\right\}; for\ R = \frac{\partial H}{\partial t}$$

In this equation, V^* is the switching volume, or the minimum volume of material that reverses its magnetization. We can measure hysteresis curves at different field rates, and extract from this a value of the switching volume. We can compare this volume to a physical volume of the particle and draw conclusions on the reversal method of the array. If the switching volume is equal to the physical volume of one particle of the array than

this suggests that individual particles reverse their magnetization in a coherent and independent fashion. If the switching volume is higher than the physical volume, than on average several particles reverse their magnetization collectively, a behavior which is not favorable in the case of patterned magnetic media, as data would be stored over several particles (islands). Lastly, if the switching volume is less than the physical volume of one particle, than the reversal is incoherent, and the particle reverses its magnetization by domain wall nucleation/growth.

2.6 Imaging magnetism on the micro- and nano-scale

2.6.1. Introduction

Ever since Weiss postulated his theory of ferromagnetism in 1907 in which he predicted the existence of magnetic domains[29], the need for imaging magnetic materials on the microscale has been evident. Early work by Bitter included decorating the surface of the magnetic material with magnetic particles[30] that would arrange themselves on the surface guided by the stray fields emanating from the sample. Recently, methods such as photo-emission electron microscopy (PEEM) combined with x-ray magnetic circular dichroism (XMCD)[31, 32] have shown

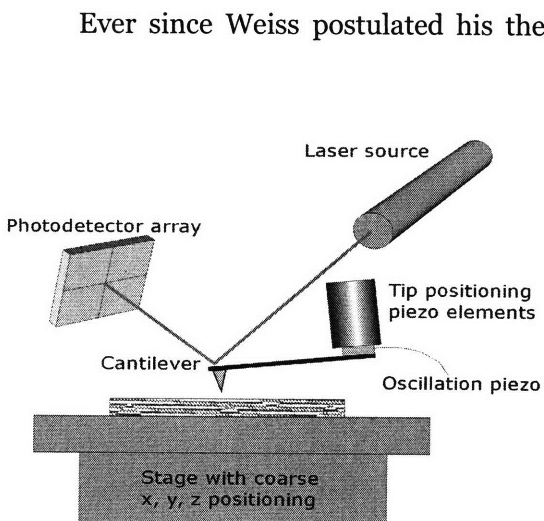

Figure 2-9: Typical setup of the cantilever and the optics of a scanning probe microscope. An x, y, z stage for sample positioning is common, as well a piezo-driven mount for scanning (and driving) the cantilever. The optical setup is also shown where a laser beam is reflected off the backside of the cantilever and onto a photodetector array sensitive to minute cantilever displacements.

great promise in imaging magnetic structures. This technique is based on the different absorption of left- and right- circularly polarized light (soft x-rays in this case) and can be used to determine spin and orbital moments, or to observe magnetic domains. Scanning electron microscopy with polarization analysis (SEMPA) is another technique which has good resolution and is based on performing a spin analysis on the secondary electrons emitted from the sample[33, 34]. Perhaps the most widespread method of imaging magnetism on the micro and nanoscale is magnetic force microscopy (MFM).

Magnetic force microscopy is a modification to the scanning probe microscopy (SPM) technique. The sharp tip of the scanning probe microscope is modified by "attaching" a magnetic particle, and the sample is imaged by detecting the interactions of the magnetic particle with the stray fields from the sample. Unlike Bitter's method, the magnetic particle is not attached to the sample surface, so evolving magnetic structures can be imaged.

The first MFM measurements were performed by Saenz et al.[35] only three short years after the invention of the scanning probe microscope. They followed similar approaches as Martin et al. to image the forces between the tip and the substrate[36], except instead of imaging van der Waals forces, the MFM technique mainly detects magnetic forces. It was Rugar et al. who performed the first useful MFM measurements applying the technique to observe the magnetic structure of longitudinal recording media[37]. In the years after these initial experiments magnetic force microscopy has exploded in a multitude of varieties – samples have been investigated in air, in vacuum[38], at low temperatures[38, 39] and in large external fields[40]. Furthermore it is possible to calibrate[41, 42] the MFM so that the sample stray fields can be well characterized and quantified from the MFM image.

2.6.2. Scanning probe and magnetic force microscopy

The most basic scanning probe microscopy consists of dragging a very sharp tip attached on a cantilever in a raster motion across a surface and measuring the deflection of the cantilever to extrapolate the surface morphology. This mode is known as "static" or "contact mode" and is useful for measuring surface topography of most samples with sub-nanometer precision. The deflection can be measured by different means, but most popular is the laser beam setup, where a laser beam is reflected from the tip of the cantilever and onto a very sensitive photodetector array (Figure 2-9). Because of the geometry, small displacements of the cantilever result in large displacement of the laser spot on the detector. The instrument is therefore sensitive to subnanometer displacements.

Dynamic mode SPM [36] is a lot more useful for imaging magnetic samples. It consists of driving the cantilever around its natural resonant frequency and following changes in its amplitude or phase. As the cantilever is brought in proximity to the surface, long- and short-range forces of the substrate start interacting with the probe and change the resonant characteristics of the cantilever. Amplitude-locked or amplitude modulation scanning probe microscopy[43] (AM-SPM, or tapping-SPM) is a mode in which the instrument follows the amplitude of the resonating cantilever as the cantilever is brought into contact with the surface. A feedback loop keeps the amplitude at a fixed value as the cantilever is scanned across the surface, adjusting the z-height appropriately to keep the amplitude constant. The z-modulation mapped across the surface gives the surface topography, and in addition, material properties variations can be mapped by following the difference between the phase shift between the driving force and tip oscillation. In frequency-locked or frequency modulated scanning probe microscopy (FM-SPM, sometimes referred to as non-contact SPM) it is the resonant frequency that

is followed and tip-sample distance is adjusted to keep the frequency shift constant. Most frequently, in FM-SPM the cantilever probe does not come in hard physical contact with the substrate and the measurement is done under vacuum.

Conventional AM-SPM measurements done in air can image magnetic structures by a combination of contact and non-contact (lift) scans performed consecutively. Using a magnetic probe, the instrument interleaves a line scan of topography (Figure 2-10, Figure 2-11a) and a line scan of magnetic measurements (Figure 2-10b). First in

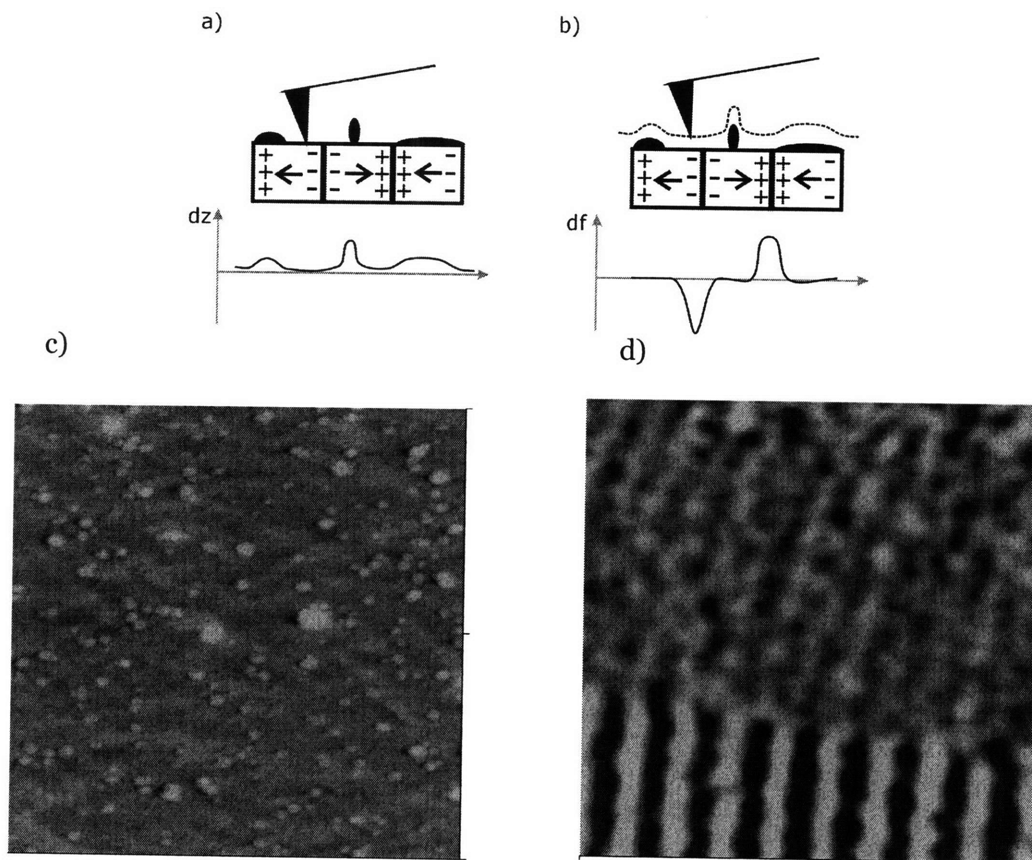

Figure 2-10: Interleave mode of AM-SPM. The instrument first measures the topography by tapping the surface with the probe (panel a), then lifts the probe and retraces the topography offset vertically by a set distance (panel b) while measuring phase changes. The second (interleaved) scan only registers the magnetic contribution. Panel c) shows the topographic image of a magnetic recording tape used for calibration, and panel d) only the magnetic image of the same area showing a track edge. Scan width is 5 × 5 μm.

amplitude modulated tapping mode it measures the height of the sample, then lifts the probe a pre-set distance above the same scan line, and measures only frequency shifts of the probe. There is no need for post-processing of the images to separate the magnetic and topographic signals (Figure 2-11 c, d). However, since the tip comes into contact with the sample, the stray field emanating from the tip can alter the state of the sample. Even for conventional low-moment probes, the stray field close to the sample tip can be significant and perturb the sample. Therefore, tapping-interleave-lift should only be used when the sample has a reasonably large coercivity, so that perturbation of the sample can be avoided. In most cases it is usually easy to detect if the sample is being modified by the tip during scanning and adjust the parameters appropriately[44-46].

For measurements using UHV FM-SPM, a magnetic probe is also used, but the data acquisition is significantly different. Typically, first an image is acquired in phase-shift constant height mode. In this case, the image reflects a convolution between magnetic and van der Waals forces as shown in the sketch (Figure 2-11). A second step, where the probe is brought in close proximity (less than 3nm) to the substrate only

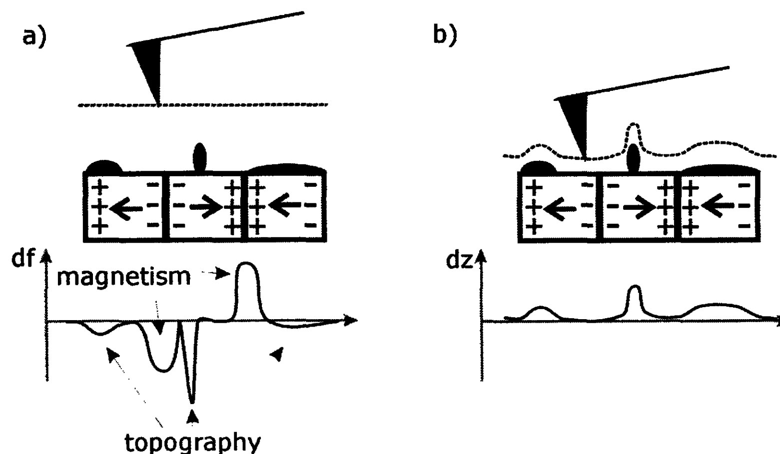

Figure 2-11: Separation of topography and magnetism by combining a constant height and constant frequency shift taken very close to the sample. Panel a) shows a convolution between the van der Waals and magnetic forces measured at a fixed distance. Panel b) only shows a true topographic measurement.[47]

reveals the topography. At this distance, van der Waals forces dominate over magnetic forces. Subtracting the topography from first image reveals the sole magnetic signal[47].

It should be noted that the tip is only sensitive to gradients in the magnetic field, such as those present near domain walls. Uniform fields do not affect the frequency of the vibration of the MFM cantilever, which makes it possible to operate the MFM under externally applied magnetic fields [35]. In order to achieve the best resolution and simplify the quantitative interpretation of the acquired data, the ideal MFM tip should be a single-domain element with a large aspect ratio (needle-like)[48, 49]. Resolution is difficult to define for MFM, but the best resolution reported gives values of 30 nm magnetic features at FWHM [50]. Quantification of the images, albeit complicated, is also possible as demonstrated by several researchers [41, 42].

Magnetic force microscopy has been advancing in large strides over the past 15 years. Even though it is a relatively new technology, it has demonstrated great promise for probing magnetism on the nanoscale. From the "crude" proof-of-concept MFM in 1987 to the instruments of today, the MFM has seen expansions which have enabled imaging of a wide variety of samples under a myriad of conditions. It is as equally capable of imaging samples in air as in vacuum, from room to cryogenic temperatures and with or without applied fields during measurement. Imaged samples can be soft or hard, patterned or atomically flat, clean or with surface contaminants (unless they are magnetic) and sample preparation is not required. In addition, an MFM can be used as a tool for local magnetic manipulation, as demonstrated by (involuntary) perturbation of local magnetization by a hard high moment probe.

References

[1] H. Uwazumi, T. Shimatsu, Y. Sakai, A. A. Otsuki, I. A. Watanabe, H. A. Muraoka, and Y. A. Nakamura, "Recording performance of CoCrPt-(Ta, B)/TiCr perpendicular recording media," *Magnetics, IEEE Transactions on*, vol. 37, pp. 1595, 2001.

[2] C. A. Ross, "Patterned magnetic recording media," *Annual Review of Materials Research*, vol. 31, pp. 203-235, 2001.

[3] C. D. Mee and E. D. Daniel, *Magnetic recording technology*, 2nd ed. New York: McGraw-Hill, 1996.

[4] H. Katayama, M. Hamamoto, J. Sato, Y. Murakami, and K. Kojima, "New developments in laser-assisted magnetic recording," *Magnetics, IEEE Transactions on*, vol. 36, pp. 195-199, 2000.

[5] R. L. White, R. M. H. New, and R. F. W. Pease, "Patterned media: a viable route to 50 Gbit/in² and up for magnetic recording?" *Magnetics, IEEE Transactions on*, vol. 33, pp. 990, 1997.

[6] S. Y. Chou, M. S. Wei, P. R. Krauss, and P. B. Fischer, "Single-domain magnetic pillar array of 35 nm diameter and 65 Gbits/in. density for ultrahigh density quantum magnetic storage," *Journal of Vacuum Science & Technology B (Microelectronics Processing and Phenomena)*, vol. 76, pp. 6673, 1994.

[7] S. Y. Chou, "Patterned magnetic nanostructures and quantized magnetic disks," *Proceedings of the IEEE*, vol. 85, pp. 652, 1997.

[8] Hitachi-GSM, "Hitachi lays groundwork for 20 GB microdrive with century-old technology," http://www.hitachi.com/New/cnews/050405.html, 2005.

[9] B. D. Terris, T. Thomson, and G. Hu, "Patterned media for future magnetic data storage," *Microsystem Technologies*, vol. 13, pp. 189, 2007.

[10] R. Wood, "The feasibility of magnetic recording at 1 Terabit per square inch," *Magnetics, IEEE Transactions on*, vol. 36, pp. 36-42, 2000.

[11] H. N. Bertram, *Theory of magnetic recording*. Cambridge; New York: Cambridge University Press, 1994.

[12] M. Albrecht, C. T. Rettner, A. Moser, M. E. Best, and B. D. Terris, "Recording performance of high-density patterned perpendicular magnetic media," *Applied Physics Letters*, vol. 81, pp. 2875, 2002.

[13] J. Moritz, L. Buda, B. Dieny, J. P. Nozieres, R. J. M. van de Veerdonk, T. M. Crawford, and D. Weller, "Writing and reading bits on pre-patterned media," *Applied Physics Letters*, vol. 84, pp. 1519, 2004.

[14] B. Terris. Cambridge, 2008, personal communication.

[15] L. F. Bates, *Modern magnetism*, 4th ed. Cambridge [Eng.]: University Press, 1961.

[16] S. Foner, "Vibrating Sample Magnetometer," *Review of Scientific Instruments*, vol. 27, pp. 548, 1956.

[17] D. O. Smith, "Development of a vibrating-coil magnetometer," *Review of Scientific Instruments*, vol. 27, pp. 261, 1956.

[18] "Model 880 Vibrating Sample Magnetometer Operating Manual," Digital Measurement Systems, 1999.

[19] H. Zijlstra, "A Vibrating Reed Magnetometer for Microscopic Particles," *Review of Scientific Instruments*, vol. 41, pp. 1241-1243, 1970.

[20] "MicroMag 2900 Alternating Gradient Magnetometer Instruction Manual," Princeton Measurement Corporation, 2001.

[21] E. C. Stoner and E. P. Wohlfarth, "A Mechanism of Magnetic Hysteresis in Heterogeneous Alloys," *Philosophical Transactions of the Royal Society of London. Series A, Mathematical and Physical Sciences*, vol. 240, pp. 599, 1948.

[22] L. Néel, "Influence of thermal fluctuations on the magnetization of very fine ferromagnetic particles," *Comptes Rendus Hebdomadaires des Seances de l'Academie des Sciences*, vol. 228, pp. 664-666, 1949.
[23] J. W. F. Brown, "Relaxational Behavior of Fine Magnetic Particles," *Journal of Applied Physics*, vol. 30, pp. S130, 1959.
[24] W. F. Brown, Jr., "Thermal fluctuations of a single-domain particle," *Physical Review*, vol. 130, pp. 1677, 1963.
[25] M. P. Sharrock, "Measurement and interpretation of magnetic time effects in recording media," *IEEE Transactions on Magnetics*, vol. 35, pp. 4414-4422, 1999.
[26] P. Bruno, G. Bayreuther, P. Beauvillain, C. Chappert, G. Lugert, D. Renard, J. P. Renard, and J. Seiden, "Hysteresis properties of ultrathin ferromagnetic films," *Journal of Applied Physics*, vol. 68, pp. 5759-5766, 1990.
[27] D. Weller and A. Moser, "Thermal effect limits in ultrahigh-density magnetic recording," *IEEE Transactions on Magnetics*, vol. 35, pp. 4423, 1999.
[28] M. Sharrock and J. McKinney, "Kinetic effects in coercivity measurements," *Magnetics, IEEE Transactions on*, vol. 17, pp. 3020, 1981.
[29] P. Weiss, "Hypothesis of the molecular field and ferromagnetism," *Bulletin de la Societe Francaise de Physique*, vol. 1, pp. 95, 1907.
[30] F. Bitter, "On the inhomogeneities in the magnetization of ferromagnetic materials," *Physical Review*, vol. 38, pp. 1903-1905, 1931.
[31] S. Anders, H. A. Padmore, R. M. Duarte, T. Renner, T. Stammler, A. Scholl, M. R. Scheinfein, J. Stohr, L. Seve, and B. Sinkovic, "Photoemission electron microscope for the study of magnetic materials," *Review of Scientific Instruments*, vol. 70, pp. 3973, 1999.
[32] J. Stohr, Y. Wu, B. D. Hermsmeier, M. G. Samant, G. R. Harp, S. Koranda, D. Dunham, and B. P. Tonner, "Element-Specific Magnetic Microscopy with Circularly Polarized X-Rays," *Science*, vol. 259, pp. 658-661, 1993.
[33] M. R. Scheinfein, J. Unguris, M. H. Kelley, D. T. Pierce, and R. J. Celotta, "Scanning electron microscopy with polarization analysis (SEMPA)," *Review of Scientific Instruments*, vol. 61, pp. 2501, 1990.
[34] R. Allenspach, "Spin-polarized scanning electron microscopy," *IBM Journal of Research and Development*, vol. 44, pp. 553, 2000.
[35] J. J. Saenz, N. Garcia, P. Grutter, E. Meyer, H. Heinzelmann, R. Wiesendanger, L. Rosenthaler, H. R. Hidber, and H. J. Guntherodt, "Observation of magnetic forces by the atomic force microscope," *Journal of Applied Physics*, vol. 62, pp. 4293, 1987.
[36] Y. Martin, C. C. Williams, and H. K. Wickramasinghe, "Atomic force microscope-force mapping and profiling on a sub 100-Å scale," *Journal of Applied Physics*, vol. 61, pp. 4723, 1987.
[37] D. Rugar, H. J. Mamin, P. Guethner, S. E. Lambert, J. E. Stern, I. McFadyen, and T. Yogi, "Magnetic force microscopy: general principles and application to longitudinal recording media," *Journal of Applied Physics*, vol. 68, pp. 1169, 1990.
[38] H. J. Hug, B. Stiefel, P. J. A. van Schendel, A. Moser, S. Martin, and H. J. Guntherodt, "A low temperature ultrahigh vacuum scanning force microscope," *Review of Scientific Instruments*, vol. 70, pp. 3625, 1999.
[39] T. R. Albrecht, P. Grutter, D. Rugar, and D. P. E. Smith, "Low-temperature force microscope with all-fiber interferometer," Interlaken, Switzerland, 1992.
[40] S. Foss, C. Merton, R. Proksch, G. Skidmore, J. Schmidt, E. D. Dahlberg, T. Pokhil, and Y. T. Cheng, "Variable magnetic field magnetic force microscopy of the magnetization reversal in epitaxial iron (111) thin films," San Francisco, CA, USA, 1998.
[41] H. J. Hug, B. Stiefel, P. J. A. Van Schendel, A. Moser, R. Hofer, S. Martin, H. J. Guntherodt, S. Porthun, L. Abelmann, J. C. Lodder, G. Bochi, and R. C. O'Handley, "Quantitative magnetic force microscopy on perpendicularly magnetized samples," *Journal of Applied Physics*, vol. 83, pp. 5609, 1998.
[42] P. J. A. Van Schendel, H. J. Hug, B. Stiefel, S. Martin, and H. J. Guntherodt, "A method for the calibration of magnetic force microscopy tips," *Journal of Applied Physics*, vol. 88, pp. 435, 2000.

[43] R. Garcia and R. Perez, "Dynamic atomic force microscopy methods," *Surface Science Reports*, vol. 47, pp. 197, 2002.

[44] Z. Xiaobin, P. Grutter, V. Metlushko, and B. Ilic, "Magnetic force microscopy study of electron-beam-patterned soft permalloy particles: Technique and magnetization behavior," *Physical Review B (Condensed Matter and Materials Physics)*, vol. 66, pp. 024423, 2002.

[45] M. Farhoud, I. S. Henry, M. Hwang, and C. A. Ross, "The effect of aspect ratio on the magnetic anisotropy of particle arrays," 2000.

[46] X. Zhu, P. Grutter, V. Metlushko, and B. Ilic, "Systematic study of magnetic tip induced magnetization reversal of e-beam patterned permalloy particles," 2002.

[47] P. Kappenberger, "Exchange Bias Effect and hard Disk Media Studied by Means of Quantitative Magnetic Force Microscopy," in *Philosophisch-Naturwissenschaftlichen Fakultat*. Basel: Universitat Basel, 2005.

[48] A. Van den Bos, I. Heskamp, M. Siekman, L. Abelmann, and C. Lodder, "The CantiClever: A dedicated probe for magnetic force microscopy," Amsterdam, Netherlands, 2002.

[49] P. B. Fischer, M. S. Wei, and S. Y. Chou, "Ultrahigh resolution magnetic force microscope tip fabricated using electron beam lithography," San Diego, CA, USA, 1993.

[50] L. Abelmann, S. Porthun, M. Haast, C. Lodder, A. Moser, M. E. Best, P. J. A. van Schendel, B. Stiefel, H. J. Hug, G. P. Heydon, A. Farley, S. R. Hoon, T. Pfaffelhuber, R. Proksch, and K. Babcock, "Comparing the resolution of magnetic force microscopes using the CAMST reference samples," San Francisco, CA, USA, 1998.

Chapter 3
Pattern formation by block copolymer, interference and nanoimprint lithography

This chapter introduces self-assembled block copolymers and what driving forces are behind the pattern formation. Methods of guiding the self assembly are discussed which give control over the driving forces so that patterns with long range order can be produced. Next, both additive and subtractive techniques of transferring the microdomain pattern into different functional materials are discussed. Lastly, a brief overview of some lithography techniques used in this thesis is given to guide the reader's understanding of the processing used in this work.

3.1 Introduction

Thermodynamically driven self assembled structures of block copolymers have attracted a lot of attention in the past decade which has resulted in the publication of quote a few reviews on the use of block copolymer thin films for lithography

applications[1-11]. Block copolymers are a family of polymers that are composed of two chemically distinct polymeric chains that have been covalently bound to each other. Traditionally, one of two methods are used for the synthesis, often referred to as *one-prepolymer* and *two-prepolymer* methods[12]. The most widely explored block copolymer by far is poly(styrene-b-methylmethacrylate) or PS-PMMA but other chemistries have also been explored such as poly(styrene-b-ferrocenyldimethylsilane) (PS-PFS), poly(styrene-b-isoprene) (PS-PI), poly(styrene-b-dimethylsiloxane) (PS-PDMS), poly(styrene-b-ethylene oxide) (PS-PEO), poly(styrene-b-2-vinylpyridine) (PS-P2VP), poly(styrene-b-lactide) (PS-PLA) etc. Typically, the block copolymer is dissolved in a good solvent for both blocks and the solution is evaporated for bulk samples, or spin-cast / dip-cast onto a substrate to prepare thin films. If the kinetics permit, driven by thermodynamics, the block copolymer will microphase segregate into a state where the free energy of the system is minimized. Because of the covalent linkage, the two components cannot fully segregate, and therefore form periodic microdomain morphologies with periodicity in the 5-100 nm range. Depending on the number of monomers N, the Flory-Huggins parameter χ and the volume fraction f of the blocks, various structures emerge from lamellae (at f ~ 50%), cylinders (at f ~ 22%) to spheres (at f ~ 15%)[13]. In the bulk, the spheres are bcc packed, and the cylinders have a hexagonal packing. The molecular weight determines the size of the polymer and as a result dictates the characteristic length-scale (period) of the microdomain structure. The Flory-Huggins parameter (χ) represents the driving force for microphase segregation, and also plays into the long-range order that can be achieved by the system and is defined as:

$$\chi_{12} = \frac{z\Delta w}{k_b T} = \frac{V_{seg}\left(\delta_a - \delta_b\right)^2}{RT}$$

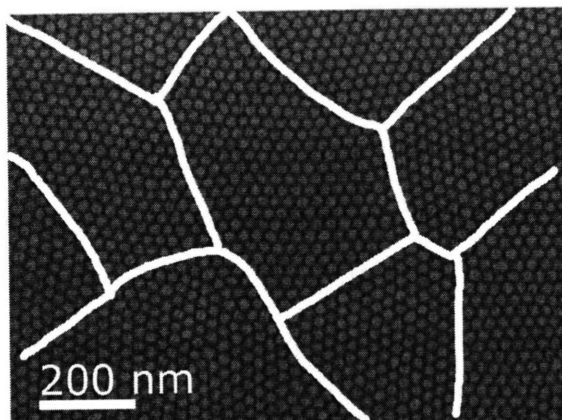

Figure 3-1: Top view SEM showing multiple "grains" of ordered polymer microdomains. The average width of each domain expressed in number of periods is the correlation length.

where z is the coordination number, Δw is the energy increment per monomer-monomer contact, V_{seg} is the volume of polymer segment, and δ_1 and δ_2 are the Hildebrand solubility parameters.

If the block copolymer is deposited as a thin film on a substrate, the microdomain structure is somewhat different. When a spherical morphology block copolymer which forms *bcc packed* microdomains in the bulk is deposited as a thin film such that a single layer of spheres is present will form a *close packed* arrangement of spherical microdomains. On the other hand, the cylindrical morphology can either form a set of parallel cylinders in the plane of the substrate, or if deposited on a neutral surface, will produce cylinders that are close packed and 'standing up' perpendicular to the substrate. Similarly, block copolymer in the lamellar morphology either form lamellae microdomains parallel or perpendicular to the substrate, depending on the substrate affinity to the blocks. Generally, the quality of ordering in a thin film is described by a parameter called 'correlation length'. This parameter measures an average size of the 'grains' across which short range order persists and is expressed in number of microdomain periods (Figure 3-1). Therefore, the higher the value of the correlation length, the better the 'quality of order' of that particular block copolymer.

Segalman and colleagues demonstrated that the segregation energy associated with the minority block χN_{min} (where N_{min} is the degree of polymerization of the minority

block) largely determines the quality of the long range order of the particular block copolymer system[14]. A low χN_{min} value stabilizes fluctuations in the system and dislocation pairs are generated and mutually stabilized resulting in a pattern rich in defects, or liquid- or hexatic-like. A system with an intermediate value of χN_{min} can form a nearly single-crystalline microdomain structure, especially if it is templated in some manner. Lasty, large χN_{min} gives a 'polycrystalline' structure because of very slow diffusion (either due to the large molecular size of the large energy penalty for mixing the two blocks).

Bulk studies of block copolymers are interesting for understanding fundamental properties of these systems. To the microelectronic industry, the behavior of the block

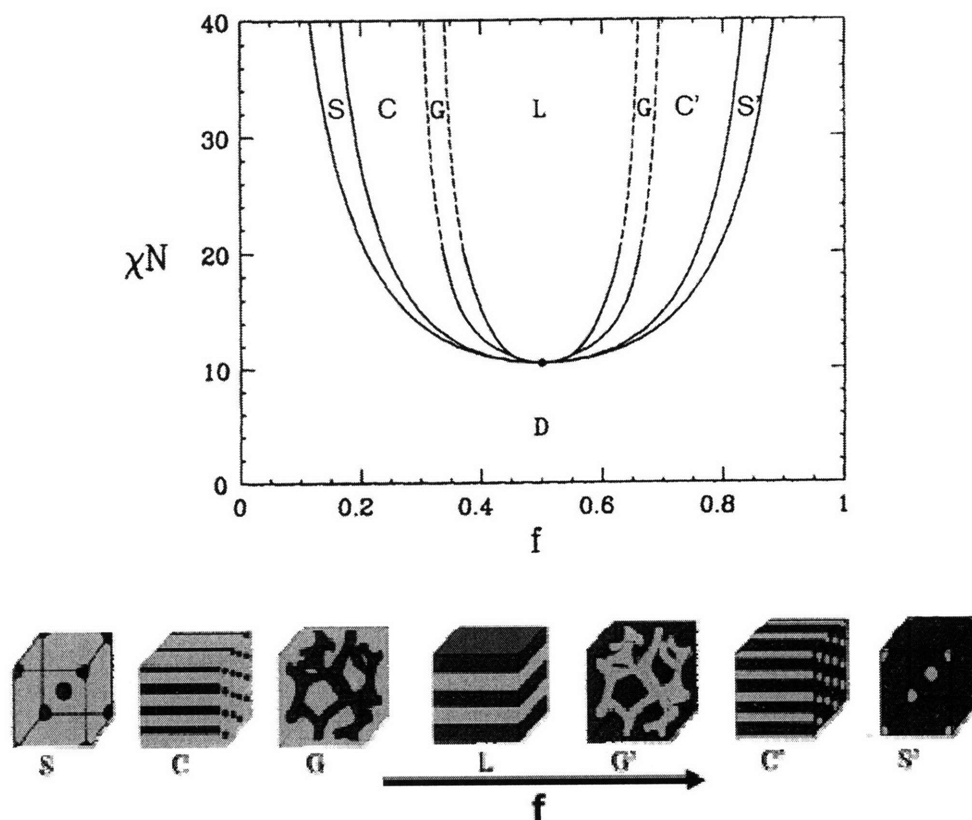

Figure 3-2: Theoretical block-copolymer phase diagram and corresponding morphologies. S – spherical, C – cylindrical, G-gyroid, L-lamellar. After [15].

copolymers in thin-film form is more interesting and will be expanded on in the following sections.

3.1.1. Methods of inducing microphase segregation

While with some BCP systems, such as PI-PFS, spontaneous microphase segregation occurs at room temperature and without any additional driving forces[16], majority of polymers require a boost of the kinetics in the form of elevated temperature[17-20] or annealing under solvent vapor[21-23]. Thermal annealing is done at a temperature above the glass transition temperature of both chains but below the order-disorder temperature of the block copolymer. At higher temperatures the mobility of the polymer is increased and as a result the polymer microdomains form a pattern which has a more uniform distribution of microdomain sizes and fewer defects. Typical annealing times range from a few hours to few days, depending on the polymer system used. A particularly fast case is PI-PFS where a 30 minute room temperature anneal will yield a well ordered structure[16, 24]. Similar to metalworking, annealing history also seems to play a role in the pattern quality of block copolymers, particularly in templated systems. Hammond and colleagues showed that a short anneal above the order-disorder temperature followed by an anneal at a lower temperature helps 'reset' the isotropic state and improves long range order of the system[25]. Zone-annealing, similar to the zone-refining method of crystal growth, is also applicable as a method of increasing the long range order of block copolymer microdomain structures in thin films as shown by Hashimoto[26, 27] and by Berry[28]. A thermal gradient is moved through the polymer film and, analogously to the zone-refining method, dislocation and defects in the block copolymer structure are annihilated. Interestingly, if the hottest temperature is kept below the order-disorder transition, and a sample is zone-annealed without previous

thermal treatment, long range order persists over a much larger area than the same treatment to a sample that has previously been annealed. This agrees well with simulation and theory developed by Zhang[29] and Boyer[30] where block copolymers evolve into highly persistent low-energy metastable states under isotropic annealing conditions.

Increasing the mobility of the system can also be performed using solvent annealing, during which a sample is placed in a vapor atmosphere of a neutral solvent which swells both polymer chains. PS-PMMA, PS-PEO and PS-PDMS thin films have been vapor annealed with great success demonstrating improved microdomain ordering uniformity[21-23, 31]. It should be noted that solvent annealing is highly dependent on the choice of polymer, solvent, vapor pressure and surface pre-treatment. In addition to using a neutral solvent, annealing can be performed in a selective solvent which preferentially swells one of the blocks which can result in a change of film morphology[21]. Changes in morphology can also arise from changes to the surface energies between the environment and the polymer, between the two blocks and between the polymer and substrate due to polymer swelling, and should be considered when choosing an annealing method. Lastly, it should be noted that typical solvent annealing can take as short as 1 minute, or as long as few days which is an important point to be considered for manufacturing applications.

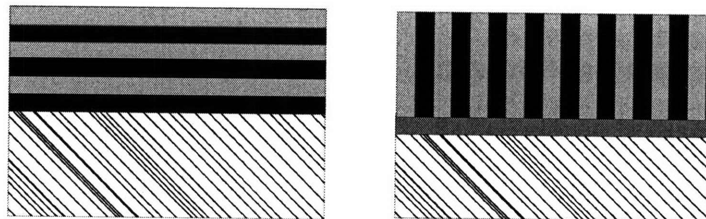

Figure 3-3: Orientation of a lamellar phase diblock copolymer on a surface: left, the surface has preferential wetting to one of the block, right, a neutral surface has no preference to the wetting of the blocks.

3.1.2. Surface modifications

Appropriate orientation of the microdomains in the block copolymer films is an important consideration for the use of block copolymer lithography, especially for morphologies which have directionality, such as the cylinder or lamellae. The microdomains can be oriented by a variety of methods, such as external fields (for example electrical fields), various epitaxy methods that will be discussed at a later chapter, and surface modifications. Surface modifications rely on the fact that interfacial interactions play a crucial role in the microphase segregation of the block copolymers. If one of the blocks has a much lower interfacial energy with respect to a surface as compared to the other block, that block will preferentially segregate at the surface. For example, in the case of PS-PFS, the PS-air interfacial energy is lower than the PFS-air interfacial energy, and therefore the PS preferentially segregates at the air-block copolymer interface. The situation is reversed at the surface with silica where the PFS block has a lower energy and will therefore segregate at that interface.

If a perpendicular alignment is desired, the surface needs to be modified such that it is neutral with respect to both blocks. This is typically achieved by a surface treatment with a random copolymer or a self-assembled monolayer which modifies the energy at that surface. For example random PS-PMMA copolymer treatment of the bottom (substrate-polymer) surface[32] or self assembled alkylchlorosiloxane monolayers[33] have been used to generate perpendicularly oriented lamellae and cylinders in PS-PMMA films. Modifications to the top interface (polymer-air) are possible in controlled atmospheric environments, for example during solvent vapor annealing. Blending low molecular weight block copolymer of same or similar chemical composition to the majority block can also modify the top surface chemistry by segregating the

homopolymer if the interfacial energy of the homopolymer is lower than the longer block copolymer chain.

3.2 Directed (templated) self-assembly

3.2.1. Introduction

In the previous section the process of self-assembly of block copolymers on flat substrates was discussed, showing how a spherical morphology block copolymer can form a close packed array of spheres if deposited as a thin film on a flat substrate. For device applications, such as patterned media, long range ordering, placement accuracy and pattern registration are important aspects that need to be addressed so that block copolymer lithography may be a desirable process candidate. Directed self-assembly of block copolymers addresses these challenges by taking advantage of the spatial precision of conventionally-patterned substrates to guide the assembly of block copolymer microdomains. By combining bottom-up and top-down methods of patterning, the strengths of each method are reinforced and what results is improvements to the patterning methods not achievable by solely using bottom-up or top-down methods alone [8, 9, 34].

Directed self-assembly has taken two major directions – chemical epitaxy and graphoepitaxy. Chemical epitaxy involves guiding the self assembly of the block copolymer microdomains by patterns of varying chemical characteristics, such that the block copolymer microdomains are guided due to the different affinity towards the pattern. For graphoepitaxy, topographical features constrain and guide the lateral ordering of the block copolymer microdomains. Both of these approaches can be used to fabricate well-ordered arrays of block copolymer microdomains, and common to both approaches is the 'healing' nature of the block copolymers. Since the pattern formation

of block copolymers is thermodynamically driven, any imperfections from the stochastic nature of the template formation process are smoothed out as defects increase the energy of the microphase segregated block copolymer. In chemical epitaxy this is manifested as improving the uniformity of the chemical pattern, and in graphoepitaxy as the relative insensitivity to exact dimensions of the topographical template to the quality of the ordering, as will be discussed later.

3.2.2. Chemical epitaxy of block copolymers

The principles behind chemical epitaxy are in essence similar to those governing surface modifications described earlier. Chemical epitaxy goes one step further and instead of uniformly modifying a surface, a pattern is formed such that the chemical characteristics of the surface are tailored locally. A simple modification by forming stripes of gold on a silica surface was examined by Rockford *et al.* [35] and was shown that in-plane order of lamellae-forming PS-PMMA is maximized when the period of the stripes matches the period of the lamellar microdomains. Interestingly, for thin block copolymer films, good ordering and perpendicular lamellae alignment persists even when the mismatch between the periodicity of the pattern and polymer are as large as 40%. For thicker films (greater than 500 nm), a mismatch of 10% is sufficient to cause loss of orientation control[36]. This is analogous to crystal growth on lattice mismatched single-crystal substrates, where thin films can grow epitaxially despite large stresses that build up in the film. Similar results were achieved by Yang *et al.* who used e-beam patterned self assembled monolayers to order PS-PMMA microdomains [37, 38]. Effectively, if the interfacial energy gain from preferential wetting of each block on the chemically patterned surface is sufficiently large to compensate for the strain energy due to lattice mismatch, the block copolymer will form a well-registered surface-directed

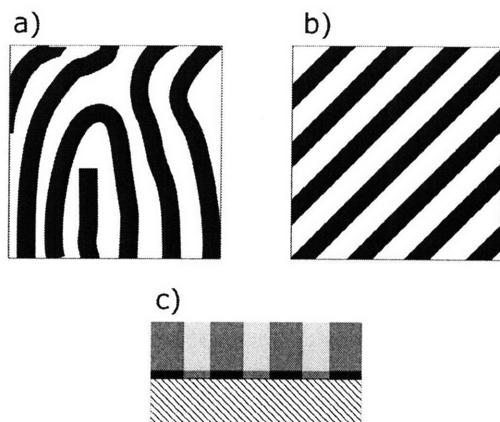

Figure 3-4: a) top view schematic of a self-assembled block copolymer in lamellar morphology on a neutral surface, b) same but assembled on a chemically patterned surface, the lamellae follow the chemical pattern on the surface c) cross-sectional view, the different colors represent different surface chemistries.

epitaxial structure[39]. By blending homopolymer, more complex structures can be replicated from the patterned surface to the block copolymer, such as sharp 45° or 90° elbow patterns, which would not form with unblended block copolymers due to the large difference in the period of the corner pattern and the block copolymer [40, 41].

Chemical epitaxy is seen as a sister-technology to conventional photoresist techniques that would enable the reduction of the variations in size and edge roughness issues as features are reduced. The block copolymers have been shown to improve the line edge roughness of e-beam patterns that arise from the stochastic nature of the e-beam process, particularly for block copolymer systems that have large χ parameters [7, 10, 42].

3.2.3. Graphoepitaxy of block copolymers

Where chemical epitaxy relies on the formation of a chemical pattern on the substrate, graphoepitaxy utilizes topographical features that can be 1-, 2- or 3-dimensional. The presence of an edge or surface causes the block copolymer to expose its close-packed microdomain direction or close-packed microdomain plane to that surface which 'seeds' the long range order that can then persists for many periods(Figure 3-5). Besides large linear confinement [43], large hexagonal features[44] and grooves[45]

have also been used to achieve long-ranger order. In these studies, the feature size was significantly larger than the period of the block copolymer microdomains. As a result, variations to the constraints imposed on the block copolymer system (such as the groove width) do not increase the free energy and therefore incommensurability does not contribute significantly to the system. However, if templates which have features on the order of the block copolymer microdomain period are used, incommensurability becomes a consideration as the block copolymer must minimize its free energy and the number of rows of microdomains makes a difference to the total free energy of the system.

Grooves have been used to order spherical and cylindrical block copolymers by several groups [17, 18, 46-52], and micro-contact printing and nanoimprint lithography have also been explored [19, 53]. Here the block copolymer system selects the most energetically favored number of microdomain rows, and adjusts for template variations by forming defects and adding additional rows of microdomains [17]. Slight variations to the pattern generally are not translated into defects, and line edge roughness in the

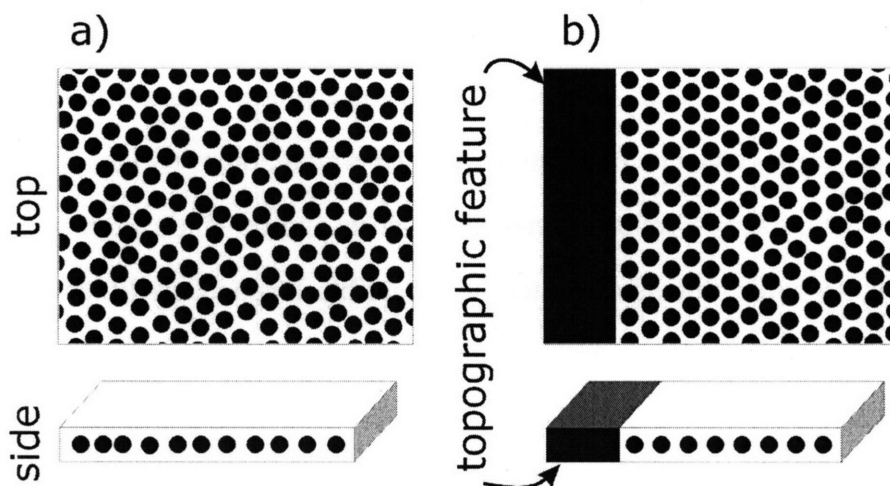

Figure 3-5: Schematic of a disordered spherical morphology thin film block copolymer and the same guided by a topographic template. The ordering is improved near the edge of the template .

template is erased by the third row of microdomains[54]. For example, in a study by Cheng et al., PS-PFS microdomains ordered in HSQ templates followed the edge of topographic feature by forming a row of microdomains at a fixed distance from the local edge (20 nm in the study, with a dispersity of 1.8 nm stemming from polydispersity of the polymer) [54]. As a result, the position of the first row of microdomains could effectively be described by the local edge contour, but by the 3rd row of PFS microdomains, this correlation was annihilated, and the row position is better fitted by a straight line than a combination of edge contours. The work explored edge contour modulations as large as 13 nm, or one half of the distance between microdomain rows. Interesting is the study of the ordering in a groove which has a width close to the natural period of the block copolymer [55]. It was found that the shape of the microdomain changes from the normal sphere to an ellipsoid under the confinement of the groove. Lastly, three dimensional patterns have also been explored[56], forcing FCC packing on an array of spherical microdomains which normally order BCC in bulk because the block copolymer always exposes the close-packed plane to a topographic surface.

Chemical epitaxy and graphoepitaxy are extensions to conventional lithographic methods into smaller feature sizes otherwise inaccessible due to limitations of the lithography method (diffraction limit, speed etc.), and chemical epitaxy can even be used to directly improve the quality of the pattern. Furthermore, they provide an economical approach as the infrastructure has already been set-up and very little alterations need to be addressed to outfit processing centers to accept block copolymer lithography as an extension to the current lithographic techniques.

3.3 Pattern transfer from block copolymers

3.3.1. Introduction

In the previous sections, the pattern formation of block copolymer microdomains was discussed along with methods of achieving better ordering. In a very few limited cases the block copolymer microdomain pattern forms a functional device in itself, but usually the pattern will need to be transferred into a functional material.

Forming the relief pattern typically relies on the selective etching or by the dissolution and swelling of one of the blocks. Depending on the block copolymer used, different methods are utilized. For example, in block copolymers where one block is organic and the other contains inorganic elements in the backbone, oxygen reactive ion etching, or oxygen plasma etching can be utilized to selectively remove the organic block. For PS-PMMA, a rinse in acetic acid is used to etch away the PMMA block leaving behind only the PS microdomain structure. Depending on the polymer system used, there needs to be a method of removing one of the blocks in such a way that the remaining structure may be used for further pattern transfer.

3.3.2. Additive methods

Generally speaking, additive pattern transfer methods rely on the addition of a functional material to a pre-patterned mask, sometimes followed by a removal of the masking material. This technique is akin to using a stencil and painting through this stencil to obtain the desired pattern. Thurn-Albrecht *et al.* used PS-PMMA templates to electro-deposit cobalt within the pores and as a result obtained cobalt nanowires[57]. Besides using the block copolymer as a direct template for deposition of materials, material can be deposited on top of the relief structure formed by the block copolymer.

Chuang *et al.* used PS-PEO/OS blended block copolymer to obtain an 'anti-dot' pattern (pores in a film) in the surface of a polymeric layer, on top of which magnetic films were deposited[58]. Xiao *et al.* took a similar pattern of PS-PMMA and after depositing a Co layer onto the etched block copolymer structure, successfully performed lift-off by a mild ion beam etching followed by oxygen etching to remove the deposited film on the surface resulting in a successful fabrication of cobalt islands or dots on the silicon substrate. Generally lift-off is a difficult process when small features are required due to the difficulty of depositing discontinuous layers that can easily be removed at such dimensions. Subtractive methods are more flexible when it comes to patterning smaller features, but have limitations of their own.

3.3.3. Subtractive methods

Subtractive methods rely on the initial deposition of the desired material, masking it and then removing the material not covered by a mask. As a result, control over the microstructure of the active layer along with any additional requirements on crystalline axis orientations is possible and well understood. Typically, material removal is performed by dry etching, such as reactive ion etching, plasma etching or ion beam etching.

The most straightforward way of performing subtractive processing is using the block copolymer as a direct mask to pattern a substrate. For example, Kubo and colleagues [59] first deposited a permalloy film on which a layer of PS-PI-PLA was spin coated. After anneal, the block copolymer formed perpendicular PLA cylinders in a PS-PI matrix. The PLA cylinders were removed and the resulting pattern was transferred using Ar ion beam etching forming 30.5 nm holes in the permalloy film with periodicity of 50.5 nm. Similar processing was used by Liu *et al.* to form Fe/FeF_2 antidot arrays[60].

Naito *et al.*[18, 61-63] used a process similar to 'image reversal' in standard photolithography. A pattern of close-packed holes is first formed in PS-PMMA by degrading the PMMA block with acetic acid. Next a spin-on-glass (SOG) is deposited which fills in the pattern in the block copolymer and the pattern is etched back to the surface of the PS layer. The PS is removed leaving behind an array of SOG islands. These islands are then used as an etch mask where the pattern is transferred into a magnetic layer, forming 40 nm islands of CoCrPt with periodicity of 80 nm.

Understandably, the subtractive patterning method has certain flexibility because the magnetic films can be optimized independently of the pattern formation steps and generally do not affect the block copolymer structure. As a result, this approach has been used extensively throughout this thesis and will be expanded upon in the following sections in greater detail.

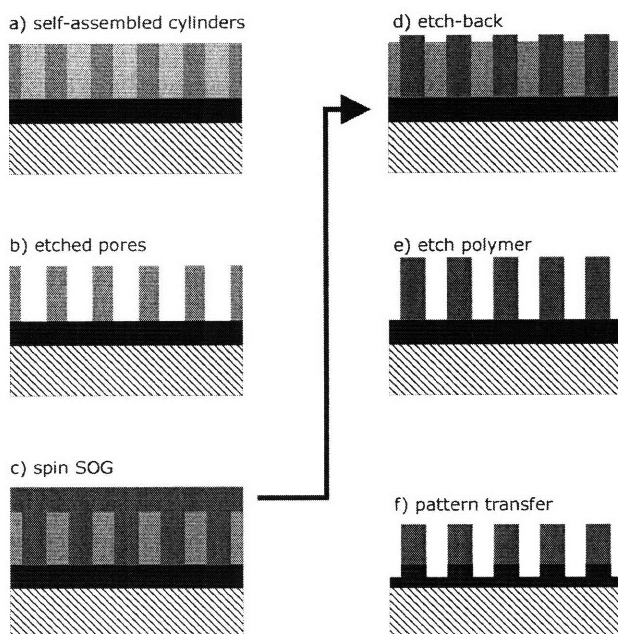

Figure 3-6: Naito's process for image reversal and pattern transfer from a self-assembled block copolymer pattern[18].

3.4 Unconventional lithography methods

3.4.1. The Lloyd's mirror interferometer lithography tool

A variety of processes have been developed for patterning material on the micro- and nano-scale. Several good references compare the advantages and limitations of various tools [64, 65] that have been developed for the microelectronics industry. Photolithography involves the use of a photosensitive material (photoresist) which undergoes a chemical change when exposed to radiation such that the solubility of the exposed region is different than the unexposed region. A selective solvent creates a relief pattern in the photoresist which can then be transferred into other layers.

Interference lithography (IL) is a method of fabricating periodic patterns, such as a grating. The Lloyd's mirror interference lithography tool is particularly appealing as it provides for fast processing and can be utilized for multi-step exposures to create 2D periodic patterns in addition to simple gratings. The setup is based on the Lloyd's mirror interferometer, an early tool which was used to examine the wavelike nature of light by the unaided eye. Today, the tool is used in the opposite extreme – to create interference patterns with periods as small as possible[66]. This is done by using a highly coherent light source – a HeCd laser and appropriate placement of the mirror and image planes. Figure 3-7 is a schematic of the entire setup. The laser beam (λ = 325 nm) is reflected in such a way to ensure the incident light at the image plane is TE polarized (electric field parallel to the substrate). This ensures a higher contrast in the fringes than TM polarization. Before reaching the substrate, the light is filtered at a spatial-filter to remove the high spatial-frequency noise from the beam and ensure an even Gaussian profile. The interferometer is a substrate holder and a mirror arranged at 90° to each other mounted on a rotation stage at a distance of about 2 m from the spatial-filter. The

substrate is coated with a photo-resist which is effectively exposed by the interference pattern of two coherent beams – one direct and a second one reflected from the mirror. These beams interfere at the surface to create a standing wave which is registered into the photo-resist.

The large distance is somewhat of a tradeoff as the beam intensity is decreased, but the uniformity across the exposure plane is increased. Therefore, this leads to more uniform line-width and longer exposure times. The long exposure would normally be undesirable as long-term stability becomes an issue – however, this is not a problem for this particular tool. Unlike double-beam interferometers, such as the Mach-Zehnder interferometer, the Lloyd's mirror setup utilizes a single-beam and as a consequence is almost insensitive to small vibrations, beam motion or air currents. Because a rigid

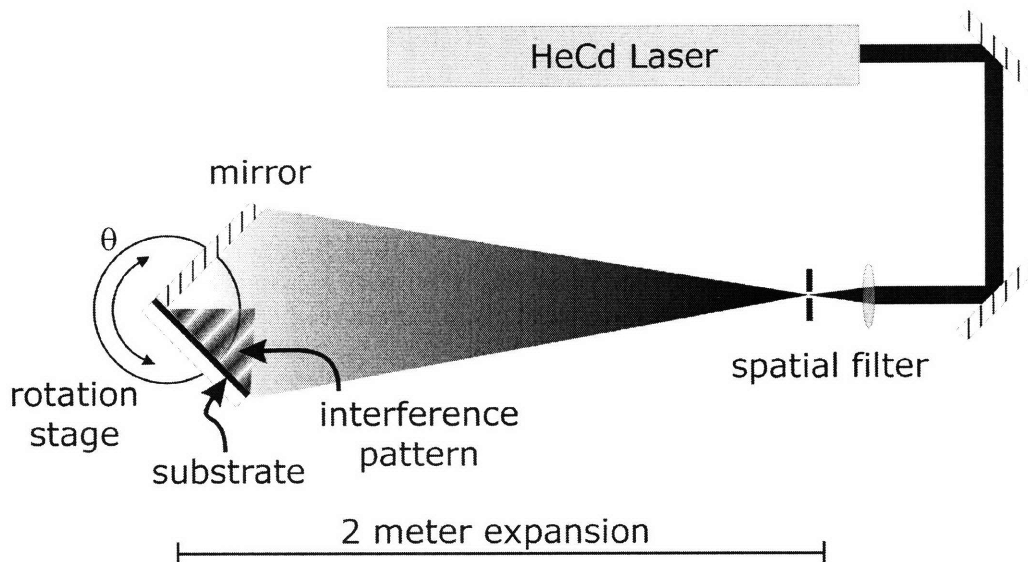

Figure 3-7: A schematic of the Lloyd's mirror interferometer lithography tool. The beam from a HeCd laser with wavelength of 325 nm is spatially filtered and allowed to expand for 2 meters. There the beam is incident on a mirror and substrate which are mounted on a rotation stage for easy adjustment of the fringe period. After Walsh[66].

mechanical connection exists between the mirror and the wafer, the few centimeters of the part where the beam splits in two arms is extremely stable. As a consequence the fringe pattern at the exposure plane is stationary which allows for long exposure times without blurring of the features.

The period of the exposed grating can be determined by the equation:

$$P_o = \frac{\lambda}{2\sin\theta}$$

where λ is the wavelength of light and θ is the angle of the incident beam to the mirror plane[66]. By simply rotating the mirror-wafer assembly, one can easily adjust the period of the exposed grating. The setup has a practical resolution of ~170 nm in pitch over areas up to 25 cm^2 with a high degree of uniformity and an error in the period less than 2 nanometers[66].

3.4.2. Tri-layer photo-resist stack for interference lithography

In the previous section, interference lithography was described as interference between two beams that produces a standing wave which is registered in a photosensitive material. In reality, one must take into account reflections from these two beams from the lower resist surface, resulting in interference between *four* beams. The primary beams interfere such as they create a standing wave perpendicular to the film plane, as discussed before. The reflected beam interference, however, creates standing waves parallel to the plane of the film which can lead to the loss of line-width control. Therefore in practice it is necessary to eliminate or minimize the reflection from the lower resist surface. This is achieved by the use of anti-reflection coating (ARC) below the resist. The use of anti-reflection coatings was proposed in the early 1980's but it was not until the 1990 that ARCs became widely accepted[67].

The ARCs function by a combination of absorption of light and thin-film interference. This suggests that both film thickness and complex refractive index must be optimized for each case. In practice, the optical properties are difficult to vary easily, so manufacturers provide ARCs such that adjusting the thickness minimizes the reflections. Solving for the reflectivity from the lower surface of the photo-resist requires that all layers at the surface of the substrate be treated as a dielectric mirror and solving for the reflectivity at a specific interface. To simplify this task, a computerized algorithm has been developed [68] that calculates the reflectivity as function of ARC thickness. In addition to the ARC thickness, one last calculation must be performed in order to fully define the exposure process for IL – exposure time. Exposure time depends on several parameters, and is calculated by:

$$t = \frac{ED}{(1-R_1)(1-R_2)\cos\theta} \cdot \frac{1}{P}$$

200 nm resist n=1.79-0.02i
20 nm SiO_2 n=1.48-0.00i
189nm ARC n=1.55-0.14i
silicon substrate n=4.68-2.03i

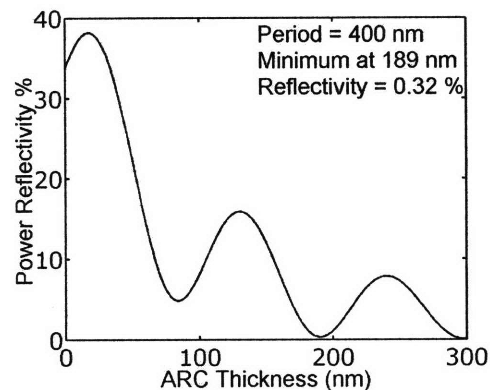

Figure 3-8: Left, optimized tri-layer stack for fabricating 400 nm period grating using interference lithography. Thickness and complex refractive index is shown for each layer. Right, a typical output of the computerized algorithm for optimizing the ARC thickness shown on left. Reflectivity at the resist/silica interface is shown as a function of ARC thickness.

where *ED* is the equivalent dose required to expose a particular resist (in the case of PFI-88, $ED = 52\ \mu J$), R_1 is the reflectivity off of the top surface of the resist, R_2 is the reflectivity off the bottom surface, θ is the incident beam angle and *P* is the incident beam power[66].

Figure 3-8 shows a typical tri-layer stack along with the output of the algorithm for optimizing the ARC thickness. This particular stack consists of a PFI-88 A3 positive photo-resist made by Sumitomo (Sumika) Chemicals, sputtered silicon dioxide as an interlayer and BARLi i-line ARC made by AZ Electronic Materials. This tri-layer was the basis of all work in interference lithography done in this thesis. The silicon dioxide is there chiefly as an interlayer to insure a faithful line-width reproduction from the photo-resist to the ARC. As this pattern transfer is done using oxygen / helium RIE, the etch selectivity between photo-resist and ARC is effectively 1:1 due to the similar chemical composition of the layers. As a result, the etching process will have a high degree of isotropy which would lead to the shrinking of the mesas, sloping sidewalls and generally poor control of the process. For precise line-width control, a chemically-dissimilar silicon dioxide layer is introduced as an interlayer and effectively an etch-stop or a hard mask. Figure 3-9 shows the steps of the pattern transfer. After exposure and developing, photo-resist lines were defined, and are sitting on top of the oxide layer. To transfer the pattern, CF_4 RIE is used to etch the oxide interlayer with the photo-resist pattern as a mask. CF_4 etches the silicon oxide because silicon tetrafluoride and carbon oxides are both volatile byproducts of the reaction, but the organic photo-resist forms no volatile species and consequently etches slowly. The middle row of Figure 3-9 shows the photo-resist lines on top of oxide lines after the RIE has been performed. Next, oxygen/helium RIE transfers the pattern into the ARC. Oxygen etches the organic photo-resist and ARC layers forming volatile carbon oxides. The He in this step serves to 'dilute' the gas and

slow the etch rate down. The etch rate of silicon dioxide using oxygen / helium RIE is effectively zero, as oxygen and silica do not form any volatile products at room temperature. When the etching is finished, lines of ARC topped by an oxide layer are visible (Figure 3-9, bottom row). The oxide mask is what enables the creation of high-aspect ratio gratings with tight control of the line-width. This pattern can now be transferred further into the substrate or used in a different manner. The process laid out above forms the basis of the IL / pattern transfer method used throughout this thesis.

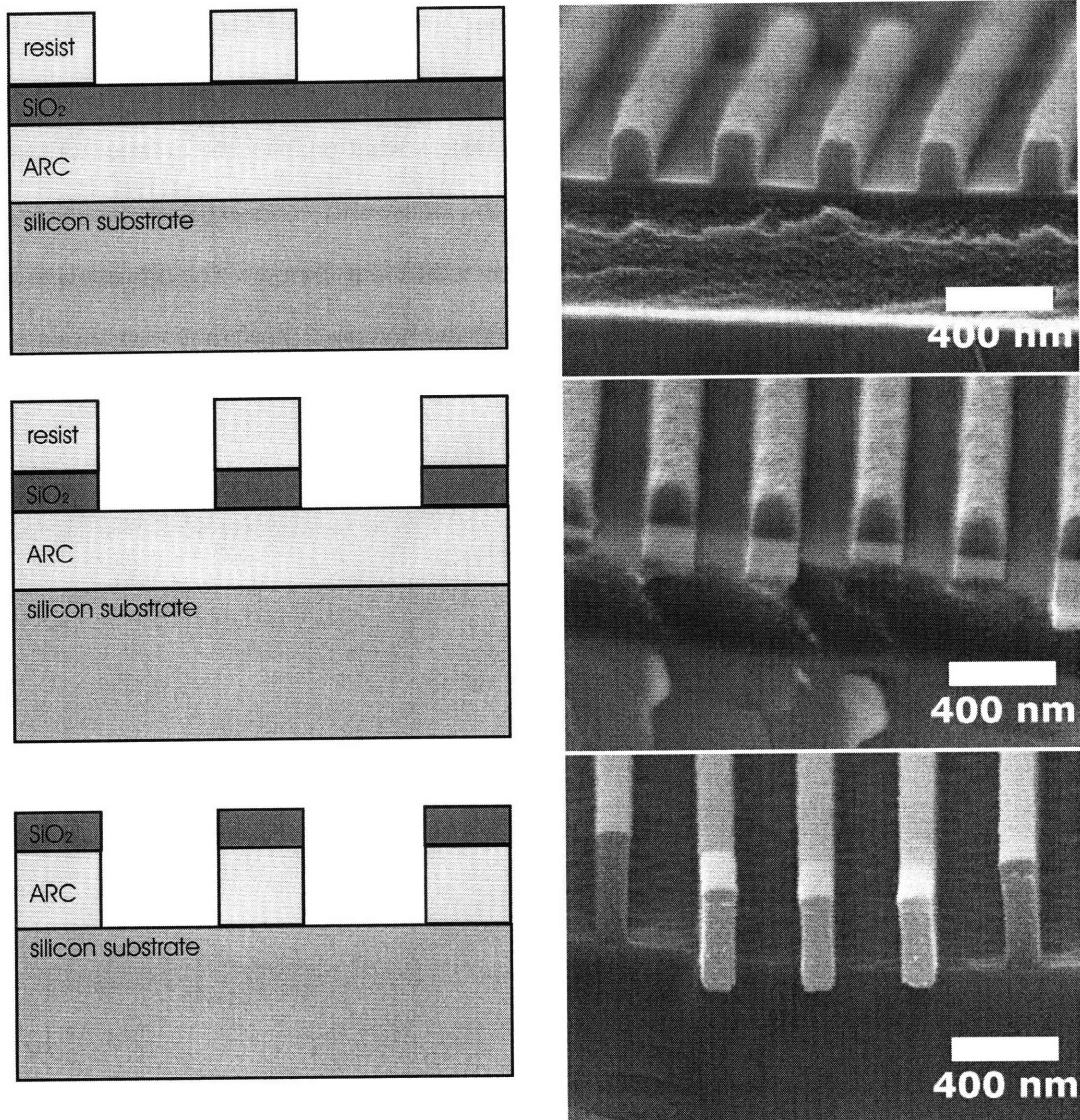

Figure 3-9: The pattern transfer of the tri-layer stack for interference lithography. After exposure and development, the photo-resist lines are transferred into the oxide layer using CF_4 RIE (second row), and lastly the pattern is transferred in ARC using He/O_2 RIE (bottom row). The slightly rough-looking bottoms of the trenches are due to ARC residue remaining that was cleared by a short He/O_2 RIE step. The resulting lines can now be transferred into the substrate or further processed. This is the basic IL / pattern transfer process used throughout this thesis.

3.4.3. Nanoimprint lithography

As has been discussed in previous chapters, there is a need for a simple method of a high-throughput fabrication with features in the regime not covered by other high throughput lithography techniques (namely the 10-100nm regime). Among others, this has lead to the proliferation of several imprinting techniques which as a group show great promise as high-resolution, fast, inexpensive and reliable methods of nanofabrication. The most notable among these methods are compared in Figure 3-10: stamping methods (also known as “soft lithography”) such as micro-contact printing[69] and nano-transfer printing[70] nano-imprint lithography[71], and step and flash lithography (SFIL)[72] which basically is nano-imprint lithography using a transparent molding mask and photo-polymerizing the polymer after the imprint step.

Nano-imprint lithography (NIL) is a technique that evolved from the hot-

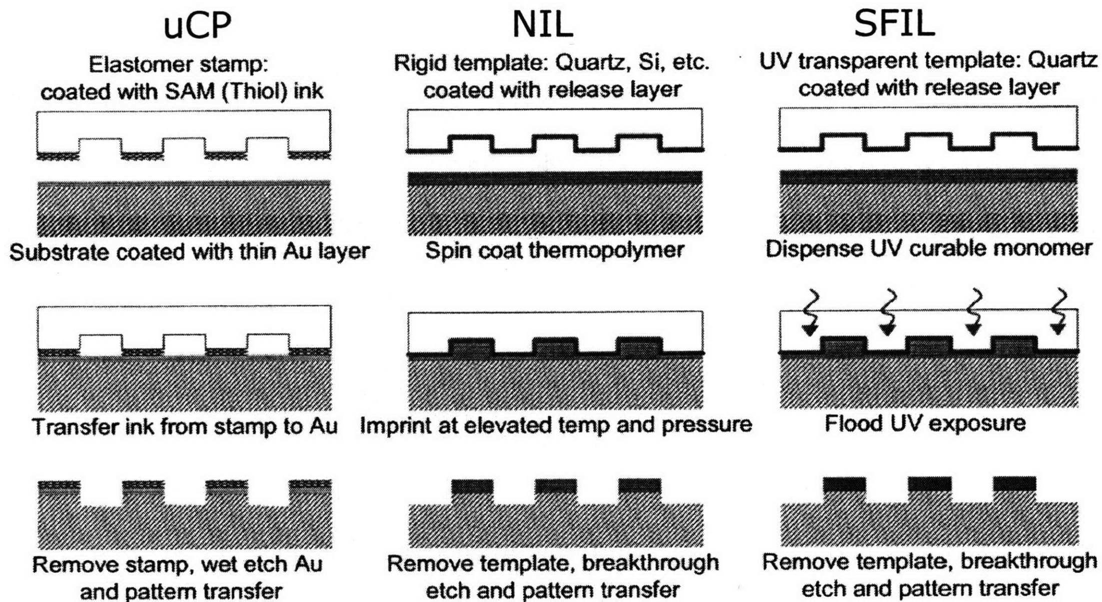

Figure 3-10: Simplified comparison of imprint lithography techniques. Pattern transfers for lift-off are also possible. After [74].

embossing process widely used in industry today to make copies of relief structures, such as compact disks (CDs). NIL was proposed by Chou[73] in 1995 and is fundamentally different from conventional lithography techniques. NIL creates an embossed relief structure in a thermoplastic resist, rather than modifying the resist using chemical and/or energetic means. It is also different from hot-embossing of compact disks as it does not emboss a structure in a bulk polymer wafer, but rather transfers the pattern in a thin thermoplastic layer which sits on a rigid substrate.

In the most basic setup, nano-imprint lithography consists of two steps – imprinting and pattern transfer. First, a solution of a thermoplastic resist (usually polymethyl methacrylate, or PMMA) is spin-cast on a wafer. The solvent evaporates to leave behind only a uniform thin layer of PMMA. The temperature is raised above the glass transition temperature of the resist, and a flat mold with nanostructures on its surfaces is pressed into the polymeric layer (imprinting step). The mold easily deforms the resist as the polymer has low viscosity at this temperature and the polymer flows into the cavities of the mold and/or is displaced by protrusions in the mold. The temperature is then lowered below the glass transition temperature of the polymer and the mold is removed. To finish the process, an anisotropic etch is performed to remove any residual resist from the compressed area (see Figure 3-10). The etching step can be extended to transfer the pattern into the substrate (pattern transfer step).

3.5 Summary

This chapter discussed the background of some unconventional methods of pattern formation. Block copolymer lithography was introduced, including methods of guiding or templating the assembly of the polymer microdomains such that long-range ordered patterns can be obtained. Next, we briefly discussed interference lithography which is a

useful tool for fabricating periodic patterns. Last, a short overview of nanoimprint lithography was given to introduce the reader to the complete set of lithography tools used in this thesis.

References

[1] C. Park, J. Yoon, and E. L. Thomas, "Enabling nanotechnology with self assembled block copolymer patterns," *Polymer*, vol. 44, pp. 6725, 2003.
[2] I. W. Hamley, "Nanostructure fabrication using block copolymers," *Nanotechnology*, vol. 14, pp. 39, 2003.
[3] G. Krausch and R. Magerle, "Nanostructured thin films via self-assembly of block copolymers," *Advanced Materials*, vol. 14, pp. 1579, 2002.
[4] M. Lazzari and M. Arturo Lopez-Quintela, "Block Copolymers as a Tool for Nanomaterial Fabrication," *Advanced Materials*, vol. 15, pp. 1583, 2003.
[5] I. W. Hamley, "Nanotechnology with soft materials," *Angewandte Chemie - International Edition*, vol. 42, pp. 1692, 2003.
[6] R. A. Segalman, "Patterning with block copolymer thin films," *Materials Science and Engineering R: Reports*, vol. 48, pp. 191, 2005.
[7] M. Li, V. Voenjarts, and C. K. Ober, in *Block copolymers II, Advances in polymer science, 190*, V. Abetz, Ed. Heidelberg: Springer, 2005.
[8] C. J. Hawker and T. P. Russell, "Block copolymer lithography: Merging "bottom-up" with "top-down" processes," *MRS Bulletin*, vol. 30, pp. 952, 2005.
[9] J. Y. Cheng, C. A. Ross, H. I. Smith, and E. L. Thomas, "Templated self-assembly of block copolymers: Top-down helps bottom-up," *Advanced Materials*, vol. 18, pp. 2505, 2006.
[10] M. P. Stoykovich and P. F. Nealey, "Block copolymers and conventional lithography," *Materials Today*, vol. 9, pp. 20, 2006.
[11] S. B. Darling, "Directing the self-assembly of block copolymers," *Progress in Polymer Science (Oxford)*, vol. 32, pp. 1152, 2007.
[12] G. G. Odian, *Principles of polymerization*, 4th ed. Hoboken, N.J.: Wiley-Interscience, 2004.
[13] F. S. Bates and G. H. Fredrickson, "Block Copolymer Thermodynamics: Theory and Experiment," *Annual Review of Physical Chemistry*, vol. 41, pp. 525-557, 1990.
[14] R. A. Segalman, A. Hexemer, R. C. Hayward, and E. J. Kramer, "Ordering and Melting of Block Copolymer Spherical Domains in 2 and 3 Dimensions," *Macromolecules*, vol. 36, pp. 3272-3288, 2003.
[15] M. W. Matsen and M. Schick, "Stable and unstable phases of a diblock copolymer melt," *Physical Review Letters*, vol. 72, pp. 2660-3, 1994.
[16] M. Roerdink, M. A. Hempenius, and G. J. Vancso, "Large area ordering at room temperature in thin films of poly(isoprene-block-ferrocenylsilane)s for nanofabrication," *Chemistry of Materials*, vol. 17, pp. 1275, 2005.
[17] J. Y. Cheng, A. M. Mayes, and C. A. Ross, "Nanostructure engineering by templated self-assembly of block copolymers," *Nature Materials*, vol. 3, pp. 823, 2004.
[18] K. Naito, H. Hieda, M. Sakurai, Y. Kamata, and K. Asakawa, "2.5-inch disk patterned media prepared by an artificially assisted self-assembling method," *IEEE Transactions on Magnetics*, vol. 38, pp. 1949-1951, 2002.
[19] T. Deng, Y.-H. Ha, J. Y. Cheng, C. A. Ross, and E. L. Thomas, "Micropatterning of Block Copolymer Solutions," *Langmuir*, vol. 18, pp. 6719-6722, 2002.
[20] R. G. H. Lammertink, M. A. Hempenius, E. L. Thomas, and G. J. Vancso, "Periodic Organic-Organometallic Microdomain Structures in Poly(styrene-block-ferrocenyldimethylsilane) Copolymers and Blends with Corresponding Homopolymers," *Journal of Polymer Science: Part B: Polymer Physics*, vol. 37, pp. 1009-1021, 1999.
[21] Y. Xuan, J. Peng, L. Cui, H. Wang, B. Li, and Y. Han, "Morphology Development of Ultrathin Symmetric Diblock Copolymer Film via Solvent Vapor Treatment," *Macromolecules*, vol. 37, pp. 7301-7307, 2004.

[22] S. H. Kim, M. J. Misner, T. Xu, M. Kimura, and T. P. Russell, "Highly Oriented and Ordered Arrays from Block Copolymers via Solvent Evaporation," *Advanced Materials*, vol. 16, pp. 226-231, 2004.
[23] Y. S. Jung and C. A. Ross, "Orientation-controlled self-assembled nanolithography using a polystyrene - polydimethylsiloxane block copolymer," *Nano Letters*, vol. 7, pp. 2046, 2007.
[24] M. Roerdink, M. A. Hempenius, U. Gunst, H. F. Arlinghaus, and G. J. Vancso, "Substrate Wetting and Topographically Induced Ordering of Amorphous PI-b-PFS Block-Copolymer Domains," *Small*, vol. 3, pp. 1415-1423, 2007.
[25] M. R. Hammond, E. Cochran, G. H. Fredrickson, and E. J. Kramer, "Temperature dependence of order, disorder, and defects in laterally confined diblock copolymer cylinder monolayers," *Macromolecules*, vol. 38, pp. 6575, 2005.
[26] T. Hashimoto, J. Bodycomb, Y. Funaki, and K. Kimishima, "Effect of temperature gradient on the microdomain orientation of diblock copolymers undergoing an order-disorder transition," *Macromolecules*, vol. 32, pp. 952, 1999.
[27] J. Bodycomb, Y. Funaki, K. Kimishima, and T. Hashimoto, "Single-grain lamellar microdomain from a diblock copolymer," *Macromolecules*, vol. 32, pp. 2075, 1999.
[28] B. C. Berry, A. W. Bosse, J. F. Douglas, R. L. Jones, and A. Karim, "Orientational order in block copolymer films zone annealed below the order-disorder transition temperature," *Nano Letters*, vol. 7, pp. 2789, 2007.
[29] C.-Z. Zhang and Z.-G. Wang, "Random isotropic structures and possible glass transitions in diblock copolymer melts," *Physical Review E (Statistical, Nonlinear, and Soft Matter Physics)*, vol. 73, pp. 031804, 2006.
[30] D. Boyer and J. Vinals, "Grain boundary pinning and glassy dynamics in stripe phases," *Physical Review E. Statistical Physics, Plasmas, Fluids, and Related Interdisciplinary Topics*, vol. 65, pp. 046119, 2002.
[31] T. Matsuyama and Y. Kawata, "Effects of solvent and ambient humidity on nanodot structures for near-field optical data storage using self-assembled diblock copolymer," *Japanese Journal of Applied Physics, Part 1: Regular Papers and Short Notes and Review Papers*, vol. 44, pp. 3524, 2005.
[32] P. Mansky, Y. Liu, E. Huang, T. P. Russell, and C. Hawker, "Controlling polymer-surface interactions with random copolymer brushes," *Science*, vol. 275, pp. 1458-1460, 1997.
[33] R. D. Peters, X. M. Yang, T. K. Kim, and P. F. Nealey, "Wetting behavior of block copolymers on self-assembled films of alkylchlorosiloxanes: Effect of grafting density," *Langmuir*, vol. 16, pp. 9620, 2000.
[34] S.-M. Park, M. P. Stoykovich, R. Ruiz, Y. Zhang, C. T. Black, and P. F. Nealey, "Directed assembly of lamellae-forming block copolymers by using chemically and topographically patterned substrates," *Advanced Materials*, vol. 19, pp. 607, 2007.
[35] L. Rockford, Y. Liu, P. Mansky, T. P. Russell, M. Yoon, and S. G. J. Mochrie, "Polymers on Nanoperiodic, Heterogeneous Surfaces," *Physical Review Letters*, vol. 82, pp. 2602, 1999.
[36] L. Rockford, S. G. J. Mochrie, and T. P. Russell, "Propagation of nanopatterned substrate templated ordering of block copolymers in thick films," *Macromolecules*, vol. 34, pp. 1487, 2001.
[37] X. M. Yang, R. D. Peters, T. K. Kim, and P. F. Nealey, "Patterning of self-assembled monolayers with lateral dimensions of 0.15 μm using advanced lithography," *Journal of Vacuum Science and Technology B: Microelectronics and Nanometer Structures*, vol. 17, pp. 3203, 1999.
[38] X. M. Yang, R. D. Peters, P. F. Nealey, H. H. Solak, and F. Cerrina, "Guided self-assembly of symmetric diblock copolymer films on chemically nanopatterned substrates," *Macromolecules*, vol. 33, pp. 9575, 2000.
[39] S. O. Kim, H. H. Solak, M. P. Stoykovich, N. J. Ferrier, J. J. De Pablo, and P. F. Nealey, "Epitaxial self-assembly of block copolymers on lithographically defined nanopatterned substrates," *Nature*, vol. 424, pp. 411, 2003.

[40] E. W. Edwards, M. F. Montague, H. H. Solak, C. J. Hawker, and P. F. Nealey, "Precise control over molecular dimensions of block-copolymer domains using the interfacial energy of chemically nanopatterned substrates," *Advanced Materials*, vol. 16, pp. 1315, 2004.

[41] M. P. Stoykovich, M. Muller, K. Sang Ouk, H. H. Solak, E. W. Edwards, J. J. de Pablo, and P. F. Nealey, "Directed assembly of block copolymer blends into nonregular device-oriented structures," *Science*, vol. 308, pp. 1442, 2005.

[42] E. W. Edwards, M. Muller, M. P. Stoykovich, H. H. Solak, J. J. De Pablo, and P. F. Nealey, "Dimensions and shapes of block copolymer domains assembled on lithographically defined chemically patterned substrates," *Macromolecules*, vol. 40, pp. 90, 2007.

[43] R. A. Segalman, A. Hexemer, R. C. Hayward, and E. J. Kramer, "Ordering and melting block copolymer spherical domains in 2 and 3 dimensions," *Macromolecules*, vol. 36, pp. 3272, 2003.

[44] R. A. Segalman, A. Hexemer, and E. J. Kramer, "Edge Effects on the Order and Freezing of a 2D Array of Block Copolymer Spheres," *Physical Review Letters*, vol. 91, pp. 196101, 2003.

[45] J. Y. Cheng, C. A. Ross, E. L. Thomas, H. I. Smith, and G. J. Vancso, "Templated Self-Assembly of Block Copolymers: Effect of Substrate Topography," *Advanced Materials*, vol. 15, pp. 1599-1602, 2003.

[46] J. Cheng, "Fabrication and characterization of nanostructures from self-assembled block copolymers." Ph. D. Thesis, Cambridge: Massachusetts Institute of Technology, 2003.

[47] J. Y. Cheng, C. A. Ross, E. L. Thomas, H. I. Smith, and G. J. Vancso, "Fabrication of nanostructures with long-range order using block copolymer lithography," *Applied Physics Letters*, vol. 81, pp. 3657-3659, 2002.

[48] K. Asakawa, T. Hiraoka, H. Hieda, M. Sakurai, Y. Kamata, and K. Naito, "Nano-patterning for patterned media using block-copolymer," *Journal of Photopolymer Science and Technology*, vol. 15, pp. 465, 2002.

[49] C. T. Black and O. Bezencenet, "Nanometer-scale pattern registration and alignment by directed diblock copolymer self-assembly," *IEEE Transactions on Nanotechnology*, vol. 3, pp. 412, 2004.

[50] D. Sundrani, S. B. Darling, and S. J. Sibener, "Guiding polymers to perfection: macroscopic alignment of nanoscale domains," *Nano Letters*, vol. 4, pp. 273, 2004.

[51] D. Sundrani and S. J. Sibener, "Spontaneous Spatial Alignment of Polymer Cylindrical Nanodomains on Silicon Nitride Gratings," *Macromolecules*, vol. 35, pp. 8531-8539, 2002.

[52] S. Xiao, X. Yang, E. W. Edwards, Y.-H. La, and P. F. Nealey, "Graphoepitaxy of cylinder-forming block copolymers for use as templates to pattern magnetic metal dot arrays," *Nanotechnology*, vol. 16, pp. 324, 2005.

[53] H. W. Li and W. T. S. Huck, "Ordered Block-Copolymer Assembly Using Nanoimprint Lithography," *Nano Lett.*, vol. 4, pp. 1633-1636, 2004.

[54] J. Y. Cheng, F. Zhang, H. I. Smith, G. J. Vancso, and C. A. Ross, "Pattern registration between spherical block-copolymer domains and topographical templates," *Advanced Materials*, vol. 18, pp. 597, 2006.

[55] J. Y. Cheng, Z. Feng, V. P. Chuang, A. M. Mayes, and C. A. Ross, "Self-assembled one-dimensional nanostructure arrays," *Nano Letters*, vol. 6, pp. 2099, 2006.

[56] V. P. Chuang, J. Y. Cheng, T. A. Savas, and C. A. Ross, "Three-dimensional self-assembly of spherical block copolymer domains into V-shaped grooves," *Nano Letters*, vol. 6, pp. 2332, 2006.

[57] T. Thurn-Albrecht, J. Schotter, C. A. Kastle, N. Emley, T. Shibauchi, L. Krusin-Elbaum, K. Guarini, C. T. Black, M. T. Tuominen, and T. P. Russell, "Ultrahigh-density nanowire arrays grown in self-assembled diblock copolymer templates," *Science*, vol. 290, pp. 2126-2129, 2000.

[58] V. P. Chuang, W. Jung, C. A. Ross, J. Y. Cheng, O. H. Park, and H. C. Kim, "Multilayer magnetic antidot arrays from block copolymer templates," *Journal of Applied Physics*, vol. 103, 2008.

[59] T. Kubo, J. S. Parker, M. A. Hillmyer, and C. Leighton, "Characterization of pattern transfer in the fabrication of magnetic nanostructure arrays by block copolymer lithography," *Applied Physics Letters*, vol. 90, pp. 233113, 2007.

[60] L. Kai, S. M. Baker, M. Tuominen, T. P. Russell, and I. K. Schuller, "Tailoring exchange bias with magnetic nanostructures," *Physical Review B (Condensed Matter)*, vol. 63, pp. 060403, 2001.

[61] K. Naito, "Ultrahigh-density storage media prepared by artificially assisted self-assembling methods," *Chaos*, vol. 15, pp. 47507, 2005.

[62] K. Asakawa and T. Hiraoka, "Nanopatterning with microdomains of block copolymers using reactive-ion etching selectivity," *Japanese Journal of Applied Physics, Part 1: Regular Papers and Short Notes and Review Papers*, vol. 41, pp. 6112, 2002.

[63] Y. Kamata, A. Kikitsu, H. Hieda, M. Sakurai, and K. Naito, "Ar ion milling process for fabricating CoCrPt patterned media using a self-assembled PS-PMMA diblock copolymer mask," *Journal of Applied Physics*, vol. 95, pp. 6705-6707, 2004.

[64] K. Suzuki and B. W. Smith, *Microlithography: science and technology*, 2nd ed. Boca Raton: CRC Press, 2007.

[65] P. Rai-Choudhury, *Handbook of microlithography, micromachining, and microfabrication*. Bellingham, Wash., USA; London, UK: SPIE Optical Engineering Press; Institution of Electrical Engineers, 1997.

[66] M. E. Walsh, "On the design of lithographic interferometers and their application." Cambridge, USA: Massachusetts Institute of Technology, 2004.

[67] T. Brewer, R. Carlson, and J. Arnold, "The reduction of the standing-wave effect in positive photoresists," *Journal of Applied Photographic Engineering*, vol. 7, pp. 184, 1981.

[68] M. E. Walsh, "Nanostructuring magnetic thin films using interference lithography." Cambridge, USA: Massachusetts Institute of Technology, 2000.

[69] A. Kumer and G. M. Whitesides, "Features of gold having micrometer to centimeter dimensions can be formed through a combination of stamping with elastomeric stamp and an alkanethiol “ink” followed by chemical etching," *Applied Physics Letters*, vol. 63, pp. 2002, 1993.

[70] Y.-L. Loo, R. L. Willett, K. W. Baldwin, and J. A. Rogers, "Additive, nanoscale patterning of metal films with a stamp and a surface chemistry mediated transfer process: Applications in plastic electronics," *Applied Physics Letters*, vol. 81, pp. 562, 2002.

[71] S. Y. Chou, P. R. Krauss, W. Zhang, L. Guo, and L. Zhuang, "Sub-10 nm imprint lithography and applications," *Journal of Vacuum Science & Technology B: Microelectronics Processing and Phenomena*, vol. 15, pp. 2897, 1997.

[72] J. Haisma, M. Verheijen, K. van den Heuvel, and J. van den Berg, "Mold-assisted nanolithography: a process for reliable pattern replication," *Journal of Vacuum Science & Technology B (Microelectronics and Nanometer Structures)*, vol. 14, pp. 4124, 1996.

[73] S. Y. Chou, P. R. Krauss, and P. J. Renstrom, "Imprint of sub-25 nm vias and trenches in polymers," *Applied Physics Letters*, vol. 67, pp. 3114, 1995.

[74] C. R. K. Marrian and D. M. Tennant, "Nanofabrication," *Journal of Vacuum Science and Technology A: Vacuum, Surfaces and Films*, vol. 21, pp. 207-215, 2003.

Chapter 4
Magnetic film deposition and properties

This chapter covers the deposition methods of magnetic thin films with perpendicular anisotropy, including requirements on deposition conditions to ensure perpendicular alignment. Magnetic reversal of thin films and of pseudo spin valve structures are examined to characterize the deposited material.

4.1 Thin film deposition by RF magnetron sputtering

Over the years various methods have been developed for depositing thin films of metallic, semi-conducting or insulating materials and many books and articles cover the vast number of techniques that have been developed [1-6]. Films are typically deposited on a surface from the vapor phase by either a chemical decomposition of a precursor (also known as chemical vapor deposition, or CVD) or by direct adsorption (physical vapor deposition, or PVD). In this thesis, a mode of physical vapor deposition – sputtering – is the method of choice employed for thin film fabrication.

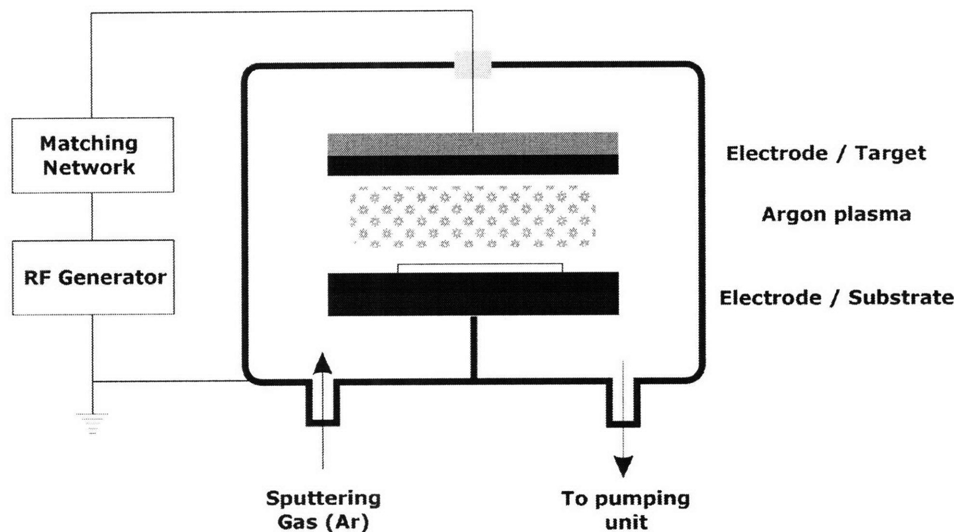

Figure 4-1: Schematic of a basic RF sputtering system. For DC sputtering the RF generator and matching network are replaced by a DC power generator.

Sputtering is certainly not a novel technique for metal film deposition. While it is generally believed that Sir William Grove was the first to report this mode of metal deposition in 1852[7], it was Langmuir that in the 1920s who developed sputtering into a thin-film deposition method [8-10].

At the heart of the sputtering system is noble-gas (most frequently Argon) plasma maintained between two electrodes. The DC biased sputtering is perhaps the simplest of all sputtering methods to explain. Ar gas at low pressures (greater than 1 mtorr) is placed between two metal plates which act as electrodes. As the voltage between the plates is increased, the neutral gas remains unaffected. At a certain value (the gas breakdown voltage V_{bd} [11]), a short high-voltage arc will "jump" between the electrodes ionizing the gas and creating a large number of ions and free electrons. These charged species will now react to the electric field in the chamber – the electrons will be accelerated towards the anode and the ions towards the cathode. Upon collision with the target, the Ar ions release secondary electrons from the cathode which are in turn accelerated towards the anode. If the voltage drop between the electrodes is sufficiently high, these secondary

electrons will excite/ionize more neutral atoms and the plasma is sustained. The energetic ions colliding with the target surface also sputter material from the surface, which is then deposited on a substrate.

While DC sputter deposition is suitable for depositing metallic materials, the deposition of any semiconducting or insulating material requires an alternating current. For RF sputtering, a high-frequency alternating voltage is applied instead of applying the direct current bias. Due to a larger mass, the Ar^+ ions are slower than the electrons (~300 times slower) and will not be capable of following the quick voltage change leaving the highly mobile electrons to strike both electrodes giving them a net negative charge with respect to the plasma.

Figure 4-1 shows a typical setup for a RF sputtering system. In addition to a RF power supply, a matching network is used to match the impedance between the plasma and the power supply. While the power supply does not provide a DC current, this should not be mistaken for non-existence of a DC voltage drop across the plasma in the vicinity of the electrodes. Without a voltage drop that accelerates Ar ions towards the target, no sputtering would occur, which would defeat the purpose of this tool. Nonetheless, biasing voltage develops on both electrodes because every half-cycle electrons strike the electrodes negatively biasing the electrodes with respect to the plasma. By making one of the electrodes much larger than the

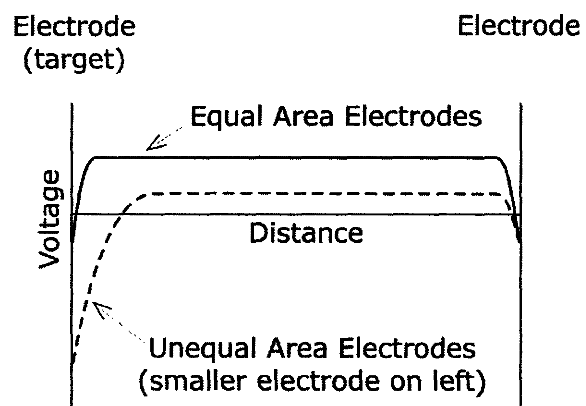

Figure 4-2: Steady-state voltage distribution in unequal area electrode RF powered system as compared to equal area electrode system. The target (source) would be placed on the left electrode and the substrate on the right. After Plummer[2] and Campbell [3]

other, a larger voltage drop will occur at the smaller electrode. Practically this is achieved by having one electrode be the chamber wall (and grounding it for safety reasons) while the other electrode is the target. The resulting voltage distribution (Figure 4-2) results in tens of volts bias of the plasma to the chamber wall, but several hundred volts bias to the target. As a result (and as desired), almost all sputtering will occur at the target.

In both DC and RF sputtering the efficiency of ionization is rather low – ion densities are around 0.0001%. This number approaches 0.03% in systems which involve a magnetron setup [2, 3] which in turn increases the sputtering rate and can lead to better film quality due to lower Ar incorporation in the deposited material. The addition of a magnetic field near the target causes the electrons to follow a spiral path due to the Lorentz force, raising the sputtering rate due to the concentrated ion flux. A magnetic field parallel to the target is desired, and this is typically achieved by a collection of permanent magnets arranged in a circular fashion (Figure 4-3).

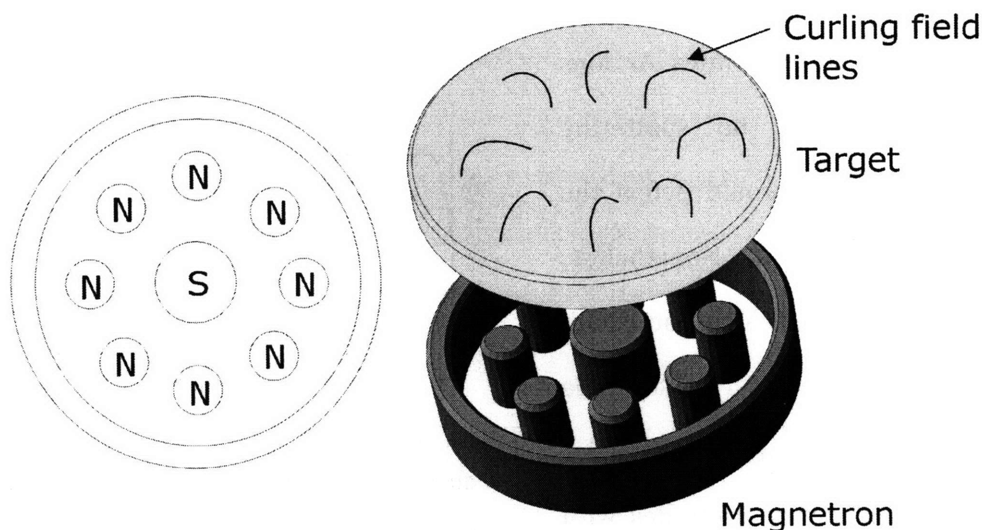

Figure 4-3: Planar magnetron sputtering system. The permanent magnets arranged circularly underneath the target create a curling field that concentrates the ion bombardment along a circular "track" between the magnets.

4.1.1. Example of a complete sputter system

While many companies provide complete system solutions for sputter-deposition systems, they are typically geared towards mass-production and typically lack the flexibility required for research and are inordinately expensive. The work done in this thesis was performed on a custom-built sputtering system developed in-house. Figure 4-4 is a schematic of the system. Base pressure in the chamber is maintained at 1×10^{-8} torr (1×10^{-6} Pa) or lower by a turbo-molecular pump backed by a mechanical roughing pump. The main chamber is brought to atmosphere only during maintenance and target exchange, so ultra high vacuum is always maintained. The sample is introduced into the chamber via a magnetically-coupled arm which transfers the sample from the load-lock to the main chamber. The load-lock is a separate small chamber connected to the main chamber via a gate-valve and is the only part of the system that is regularly cycled

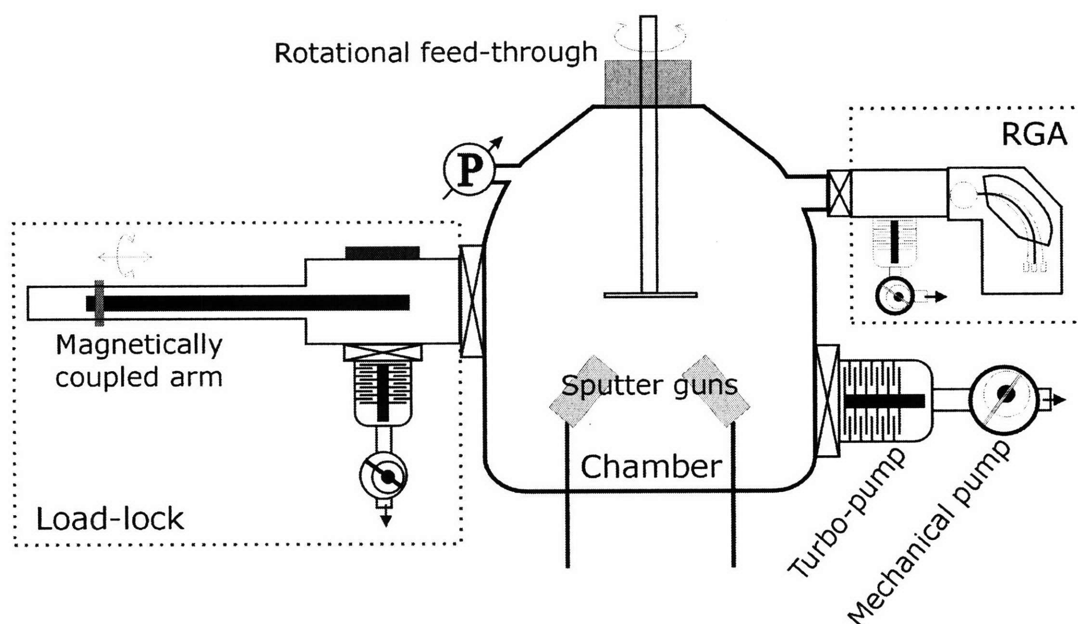

Figure 4-4: Schematic of a complete sputter system with a load-lock and a residual gas analyzer (RGA) capable of measuring gas composition during deposition. Three targets (2 shown for clarity) deposit in a sputter-up position, on a sample which is mounted on a rotating stage.

between atmosphere and vacuum.

Three RF magnetron sputter guns are positioned in a sputter-up position, each with a separate shutter, power supply and matching network. The guns can operate independently of each other, or can be run simultaneously for co-sputtering. A gas-mixing manifold supplies the sputtering gas to each of the guns. Two mass-flow-controllers regulate the gas-flow and can be used to control the relative amounts of a sputtering gas (Ar) to a reactive gas introduced for reactive sputtering (such as O_2). Vacuum-grade stainless steel tubing provide ultra-pure sputter gasses (99.999% Ar and Ar/O_2 mixtures).

For increased film uniformity, during deposition the sample can be rotated at speeds up to 80 rpm (in most cases 30 rpm is sufficient). The system also has the capability to heat the substrate up to 250 °C during deposition by resistively heating the substrate holder via an external heater located in the hollow rotational feed-through shaft, but heating was not necessary for the work done here. A differentially-pumped residual gas analyzer (a mass spectrometer) provided the relative concentration of gasses during sputtering.

4.2 Magnetic thin films with perpendicular anisotropy

As outlined in previous chapters, block copolymer lithography is a versatile technique which can be applied in the fabrication of a wide variety of devices, among which is bit-patterned media with perpendicular anisotropy. We need to start with a film with perpendicular anisotropy. This can be achieved by having a strong magnetocrystalline anisotropy pointing in the desired direction. For this purpose, we have selected a cobalt alloy as the material, as a cobalt-platinum alloy has a very strong uniaxial magnetocrystalline anisotropy (K_{U1} = 4.1×10^5 J/m^3, K_{U2}=1.4×10^5 J/m^3), and the crystalline c-axis is the axis of easy magnetization[12] . What this means is that the magnetization has a preferred crystallographic direction along the c-axis, and if no external field is present, than the magnetization direction will be codirectional with the crystalline c-axis. If we ensure a directional growth of the c-axis so that it points out of plane of the film, then the deposited film will have an easy magnetization axis perpendicular to the plane of the film. This directionality should persist even when the film has been patterned into magnetic elements, which is our ultimate goal, since the competing shape anisotropy would be reduced by 50% based on a reduced

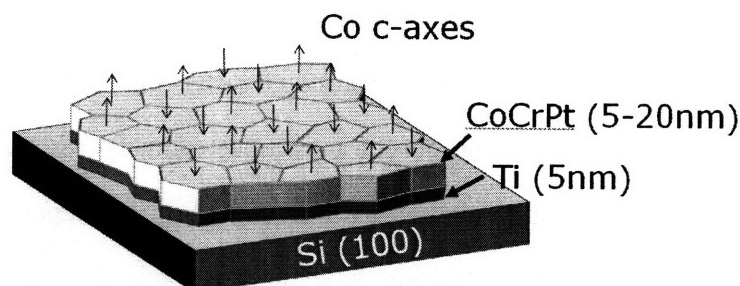

Figure 4-5: Schematic of the Ti/CoCrPt film grown on a Si substrate. Arrows show the perpendicular alignment of the crystalline c-axis of cobalt which is the easy magnetocrystalline direction.

demagnetization factor (1 for a thin film, 0.53 for an oblate ellipsoid).

A substantial amount of work has been done on superlattices of Co and noble elements, such as Pt and Pd[13-19]. These films typically exhibit perpendicular anisotropies. However, they are problematic to grow as they require specialized growth apparatus, and often consist of upwards of 40 layers. Etching of these films is also difficult because they lose their perpendicular anisotropy if there is ion-bombardment induced mixing between the layers. A much simpler system to work with is an alloy of CoCrPt. This family of alloys has been specifically developed for the hard-drive media industry, and have been the subject of much analysis [20-26].

We have decided on sputter-depositing Co 66 at. % Cr 22 at. % Pt 12 at. % (CoCrPt) as the starting magnetic films. Furthermore, as it is well known that CoCrPt films grown on Ti or Ta seed layers promote the perpendicular c-axis alignment of the Co, we decided on using Ti as a seed layer. The sputter deposition was carried out in a sputter chamber with 3 rf magnetron sources described in Chapter 1.1.1. Initial depositions were carried out in base pressures of 10^{-7} torr range and sputtering gas with regular purity (99.5% Ar) carried by polyethylene tubing. Those film deposition were unsuccessful in fabricating a film with perpendicular anisotropy and the problem was traced to the presence of oxygen in the sputtering gas. The sputter system was modified to sustain base pressures in the low 10^{-8} torr to mid 10^{-9} torr range, the gas carrier lines were replaced with UHV-compatible stainless steel tubing and the source gas was replaced by an ultrapure Ar source (purity of 99.9999%). Furthermore, a mass spectrometer (residual gas analyzer) was attached to the system to monitor the gas composition during deposition. The effects of introducing oxygen during deposition have been examined and are outlined in Chapter 4.3.

All films hereafter were deposited at room temperatures and at base pressure of 1×10^{-8} torr or lower. The sputtering Ar gas was flowed at a rate of 29 sccm, for a deposition pressure of 2×10^{-4} torr. RF power was set to 300 W, and typical deposition rates were 3.8 Å/sec for CoCrPt and 1.9 Å/sec for Ti at a substrate to target distance of about 15 cm. We explored the importance of the Ti seed layer thickness, and we found that, as long as the seed layer was thicker than 5 nm, the absolute seed layer thickness did not play a significant role in the quality of the film. This is in contrast to work by Roy and Laughlin [22] who found that the Ti seed layer thickness influences the quality of perpendicular c-axis alignment. We suspect that the authors did not consider the effects of contamination from poor base pressure (they report a base pressure of 5×10^{-7} torr) and sputtering gas composition.

Many samples have been deposited during this work, and most have the form of 5 nm Ti / 5-20 nm CoCrPt. We found that films as thin as 3 nm exhibit perpendicular

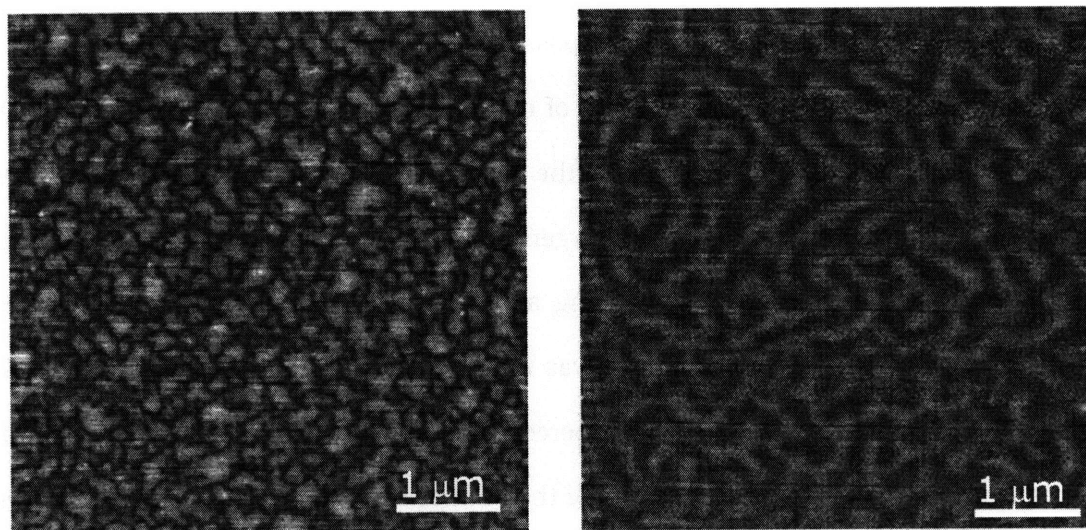

Figure 4-6: AFM / MFM images of the surface of 5 nm Ti / 15 nm CoCrPt film, left: height data showing the surface of the film, vertical scale 10 nm, right: phase image during interleave mode showing maze-like domain structures of AC-demagnetized sample, vertical scale is 2 degrees. Scan size is 5 × 5 μm.

anisotropy, which persists through films as thick as 100 nm. We mainly used 5 -20 nm thick films to avoid incomplete surface coverage for thin films and patterning issues for thick films. The deposited films are very smooth with RMS roughness of 1 nm as measured by AFM (Figure 4-6). We used an ultra-sharp MFM cantilever with a tip radius of 10 nm coated with a thin Co coating to acquire the images shown in Figure 4-6. The sample was AC demagnetized and the two images show the same physical area. The left image is of the topography showing the surface morphology of the film, and the right image is of the magnetic domains showing a typical maze-like pattern typical for perpendicular films. The magnetic domains in the AC-demagnetized state are about 100 nm wide.

4.3 Effect of oxygen partial pressure on the properties of perpendicular CoCrPt films

As outlined above, when the vacuum system had poor control over the vacuum and the quality of the sputtering gas, it was impossible to achieve out-of-plane anisotropy of the deposited films. To explore the effect of oxygen on the film quality and to establish tolerances to the oxygen concentration in the deposition atmosphere, a series of samples was prepared where the sputtering gas oxygen concentration was varied between 0 and 2 percent. This was achieved by connecting a second gas line into the sputter system manifold so that the Ar sputtering gas was mixed with the gas in the second line. To achieve better control over low oxygen percentages, we used premixed 5 % oxygen in argon as the second gas source. By varying the relative flow rates of the two gas lines we had continuous control over the oxygen composition feeding into the sputter system between 0-5 % oxygen. The actual gas composition was monitored via real-time mass spectrometry.

Nine samples were fabricated (Figure 4-7 and Figure 4-8) in 0% to 2% oxygen pressure in increments of 0.25 %. For oxygen concentration below 0.5 % the films were growing with the c-axis out of plane, with no noticeable difference in magnetic properties as can be seen in Figure 4-7. We see a typical square hysteresis indicative of easy-axis magnetization is measured when the field is applied in the out of plane direction (perpendicular to the substrate). Samples deposited in oxygen concentration 0.75 and 1 % show transitional hysteresis curves which are difficult to interpret and would require TEM work to fully understand the microstructural changes (Figure 4-9). Samples with oxygen pressures higher than 1% exhibit hysteresis curves where the easy magnetization axis lies in the plane of the sample.

Similar work was done on Cr/CoCrTa films grown at elevated temperatures by Takahashi and colleagues [27-29]. Even though the alloy they use is different, this work is relevant as CoCrTa is in the same family of magnetic alloys developed for the hard drive industry as CoCrPt. Takahashi reports that lower base pressure and low oxygen concentration leads to films with more uniform grains and better film quality, however, they report an increased coercivity for films deposited at lower base pressure which was attributed to better Cr segregation at the grain boundaries. Cr segregates during film deposition at elevated temperatures, but not as much when the deposition is carried out at room temperature. This is a crucial difference between Takahashi's and our work. As the CoCrPt films were deposited at room temperature there is no significant Cr segregation in the films. Furthermore, room temperature deposited CoCrPt films have higher coercivity when the oxygen concentration is increased, suggesting that there is an increase of magnetic domain pinning sites in the films. It is possible that the oxygen leads to grain boundary oxidation which could partially isolate the grains, leading to

higher coercivity, or alternatively, increased oxygen during film deposition leads to formation of defects or cluster which act as domain pinning sites.

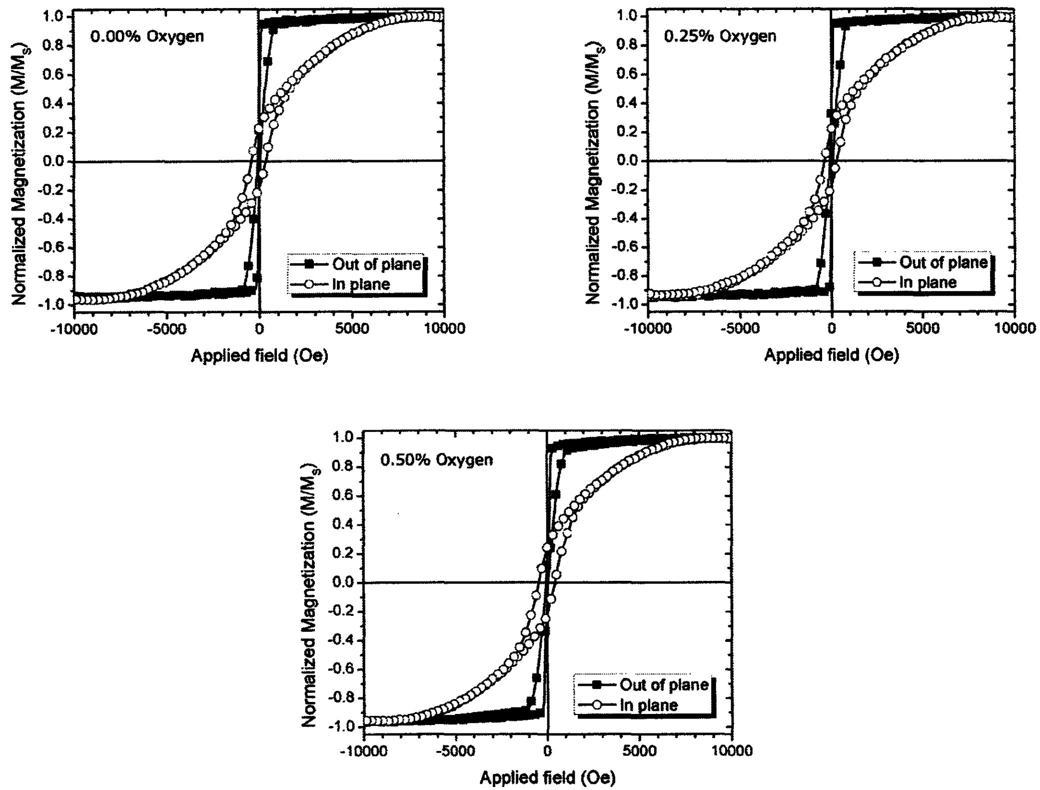

Figure 4-7: Hysteresis curves of Ti/CoCrPt films deposited in pure Ar atmosphere, and 0.25% and 0.5% oxygen.

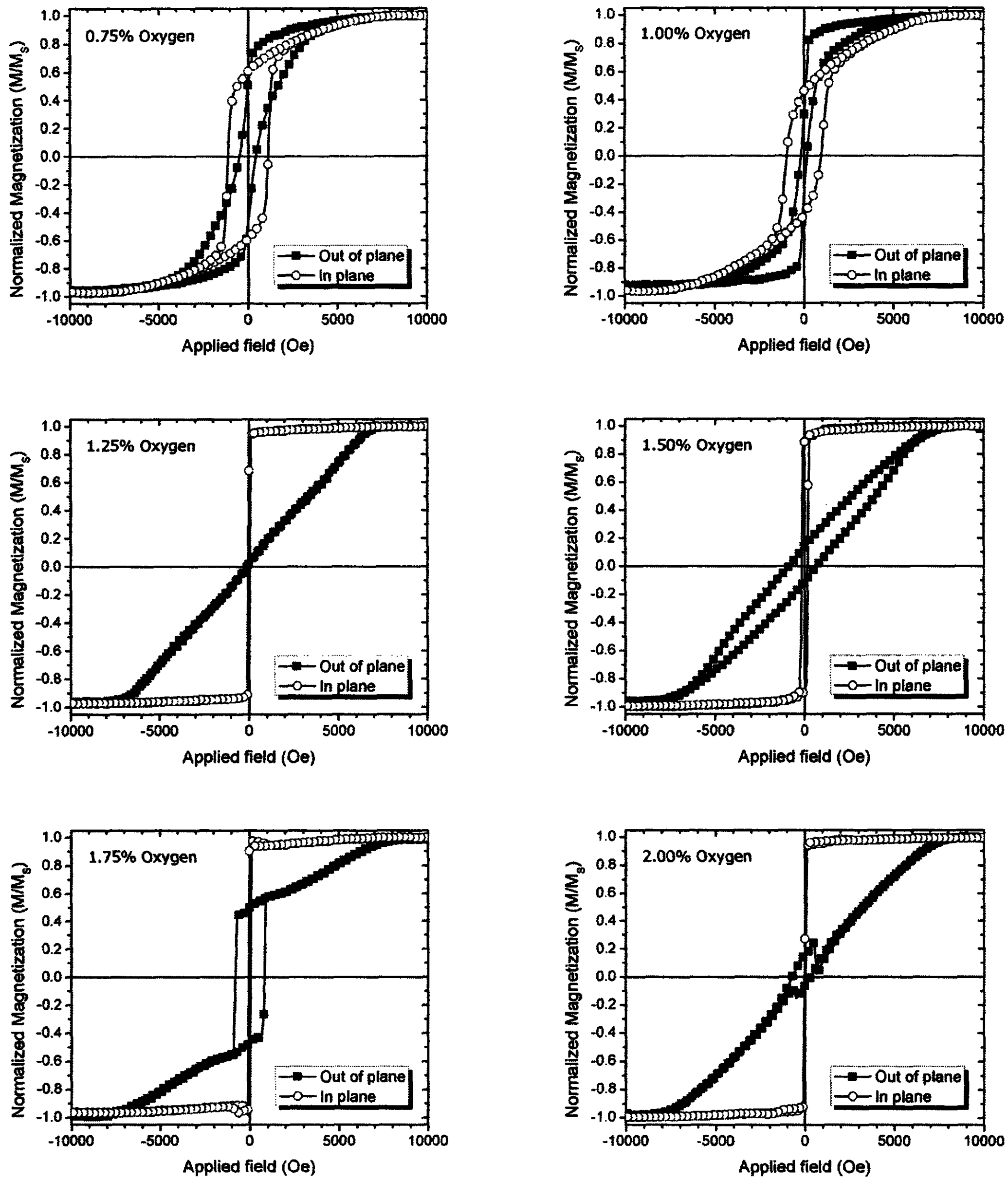

Figure 4-8: Hysteresis curves of Ti/CoCrPt films deposited in Ar atmosphere mixed with 0.75% - 2% oxygen.

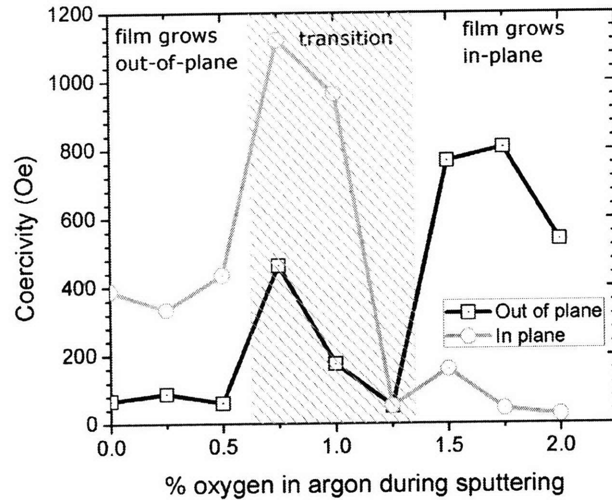

Figure 4-9: Summary figure of the deposition growth. Films deposited with oxygen concentration lower than 0.5% grow with the anisotropy axes perpendicular to the plane while those grown above 1.25% with clear in-plane anisotropy.

4.4 Magnetic reversal phenomena in pseudo spin valve films with perpendicular anisotropy

4.4.1. Introduction

To get better insight into coupling between perpendicular magnetic films, we decided to study the magnetic properties of perpendicular spin valves. A spin valve is a set of two magnetic thin films separated by a non-magnetic spacer layer so that the resistance is altered depending on the magnetic alignment of the two layers. A pseudo-spin valve utilizes the same magnetic material for both layers, but with different thicknesses in order to achieve different values of the coercive fields. Pseudo spin-valve (PSV) films with perpendicular anisotropy have so far received much less attention than PSV films with in-plane anisotropy, even though they show interesting differences in switching behavior because of the magnetostatic interactions between the layers. Furthermore, perpendicular PSVs are expected to show fewer effects of edge roughness when patterned into submicron elements and are therefore of practical interest as possible candidates for magnetic random access memory and for sensing applications such as read-back hard-drive heads. Most perpendicular spin-valve systems reported consist of superlattice structures such as Co/Pt laminates with upwards of 15 individual layers [30-33]. Magnetic reversal mechanisms have been well studied in single-layer films with perpendicular anisotropy [34, 35] but there are few reports of reversal in spin valve structures[36]. In this section we describe the magnetization reversal in a simple spin valve system of the form Ti/CoCrPt/Ti/CoCrPt with perpendicular anisotropy[36]. The Ti serves both as a seed layer to promote a perpendicular c-axis orientation, and as a non-magnetic spacer layer. We discuss a typical sample, where the layer thicknesses were 5nm Ti / 5nm CoCrPt / 5nm Ti / 20nm CoCrPt.

4.4.2. Experimental Procedures

Samples were prepared by RF magnetron sputtering using 99.999% pure Ar at base pressures better than 1×10^{-8} torr onto prime (100) Si wafers. The two CoCrPt layers ranged between 5 and 20nm thick and the Ti spacer layer thickness was varied from 1-10nm. The CoCrPt was sputtered from an alloyed target with composition of Co 66 at.% Cr 22 at.% Pt 12 at. % at room temperature with no further heat treatment to avoid Cr segregation to the grain boundaries. The magnetic properties of the samples were measured using a Princeton Measurement Corporation Alternating Gradient Field Magnetometer (AGFM) and magnetic force microscopy (MFM) images were taken at different remanent states on a Digital Instruments Dimension 3000 Scanning Probe Microscope using an Asylum Research Low-Moment Magnetic Force Microscopy tip in

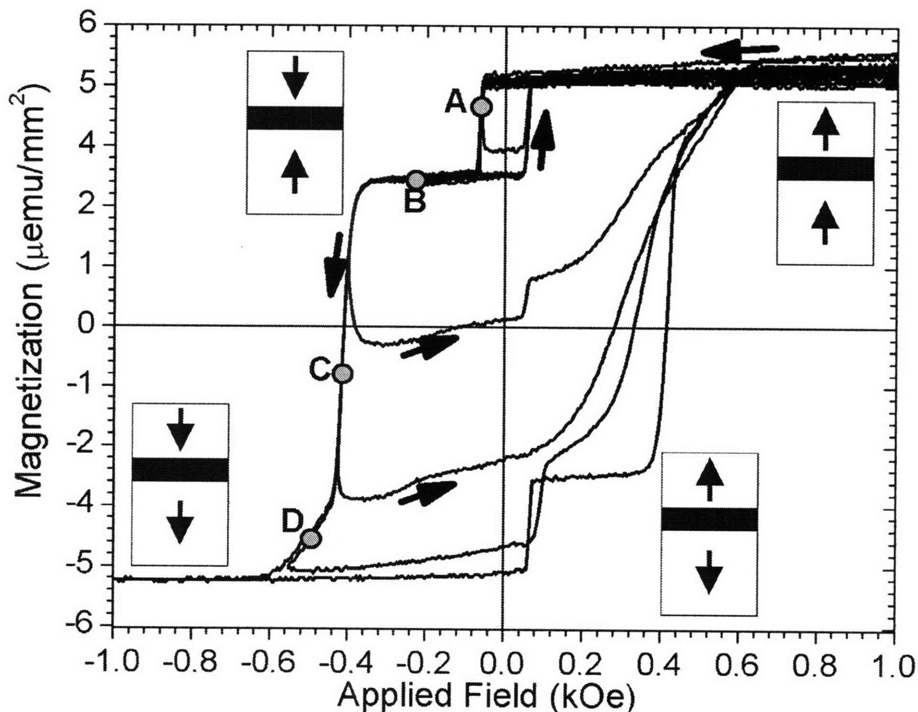

Figure 4-10: Major and minor hysteresis loops of a perpendicular PSV sample. Loops starting at the plateau B demonstrate the cycling of the thin (5nm) CoCrPt layer. Time dependent switching seen in the minor loops starting at regions A and C are attributed to domain growth.

standard lift-interleave imaging mode.

4.4.3. Results and discussion

Major and minor hysteresis loops of the film were measured with the field applied perpendicular to the sample (Figure 4-10). The major hysteresis loop exhibits a characteristic two-step switching corresponding to the switching of the two magnetic layers, and a tail-like feature (point D) on the approach to saturation.

The low-field step at H=65 Oe (point A) corresponds to the switching of the thinner (5nm) CoCrPt layer. The ratio between the step heights of the low- and high-field steps A and C, 1:4, is in agreement with the nominal thickness ratio of the two layers. The plateau B where the layers are magnetized anti-parallel to each other exists over a wide field range of 70-345 Oe. The tail of the loop, D, represents the completion of the reversal

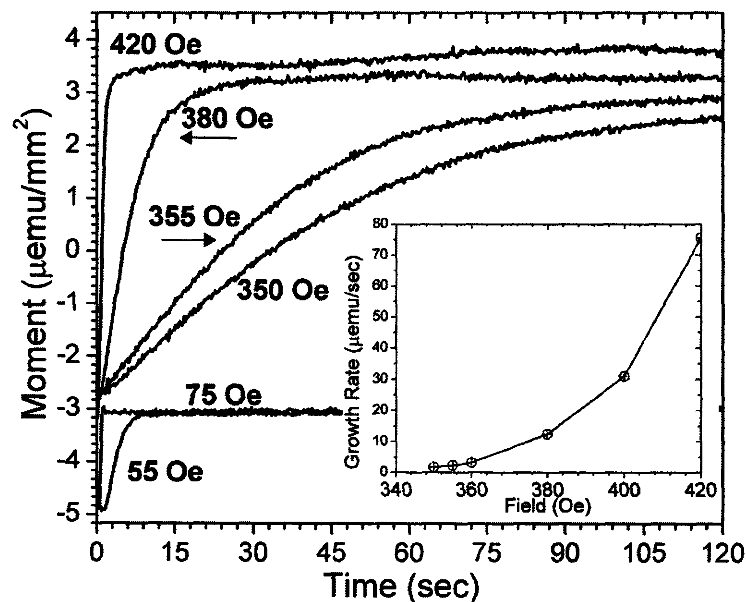

Figure 4-11: The rate of change of magnetization at a given reverse field in the range of 55 – 420 Oe, applied after saturation. When the reverse field is within either of the steps in the major loop, a time-dependent magnetization is observed. The inset shows the reversal rate as a function of applied field.

of the thicker layer. The tail is more evident for thicker films, and may correspond to annihilation of the magnetostatically-stabilized small bubble domains remaining in the thick layer after the reversal of the majority of the layer.

Minor loops starting at the first plateau (point B) illustrate the cycling of the thin layer. The minor loop is approximately symmetrical about zero field, suggesting that magnetostatic interactions with the thick layer have a small effect on the reversal of the thin layer. Magnetoresistance measurements show no measurable giant magnetoresistance (GMR) presumably due to large electron scattering in the Ti spacer layer. Minor loops measured starting from the plateau, B, show no time dependence, but when minor loops are measured starting from either of the steps A and C, a slow time-dependent magnetization is found (Figure 4-11). The sample was first saturated at a field of -10 kOe, and then the field was quickly reversed to a set value H_{rev} (between 55 and 420 Oe) where the moment was measured as a function of time at constant applied field. For H_{rev} = 55 Oe, within the low-field step, the magnetization decreases until it reaches the plateau value, within about 10 sec. For H_{rev} = 75 Oe, which is within the plateau, the rated of magnetization reversal dM/dt = 0. For H_{rev} = 350 – 420 Oe, within the high-field step, the magnetization increases to near the value for the fully-reversed film. The

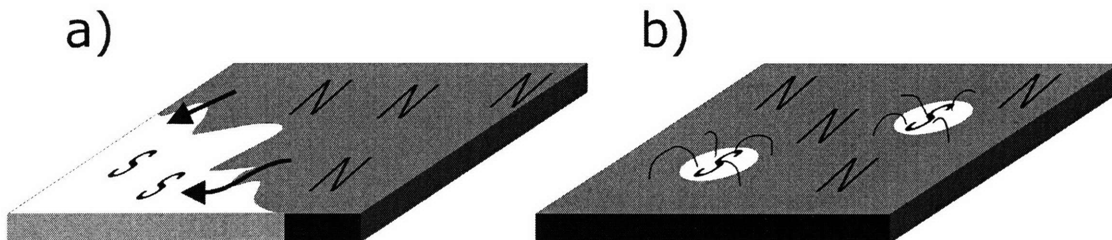

Figure 4-12: a) a large single domain (north) may expand by moving the domain wall, sometimes leaving behind a 'bubble' domain, depicted in b) which are magnetostatically stabilized and require high fields to annihilate.

time-dependent behavior is also visible qualitatively in the minor loops of Figure 4-10.

The asymptotic magnetization values suggest that the 'creep' measured for H_{rev} within the low-field step corresponds to completion of the reversal of the thin layer. In the low-field step reverse domains are nucleated in the thin layer and start to grow. This domain growth continues even when the film is held at a constant H_{rev}, and implies that the field required for domain wall propagation is smaller than the field necessary for domain nucleation. Similarly, the creep seen for H_{rev} within the high-field step corresponds to growth of reverse domains in the hard layer. A larger H_{rev} is expected to increase the rate of domain nucleation as well as the rate of domain growth, and dM/dt, the magnetization reversal rate, increases with H_{rev}. The inset of Figure 4-11 shows the magnetization reversal rate as a function of applied field for the 20nm thick layer. We notice an exponential dependence on the applied field, analogous to what has previously

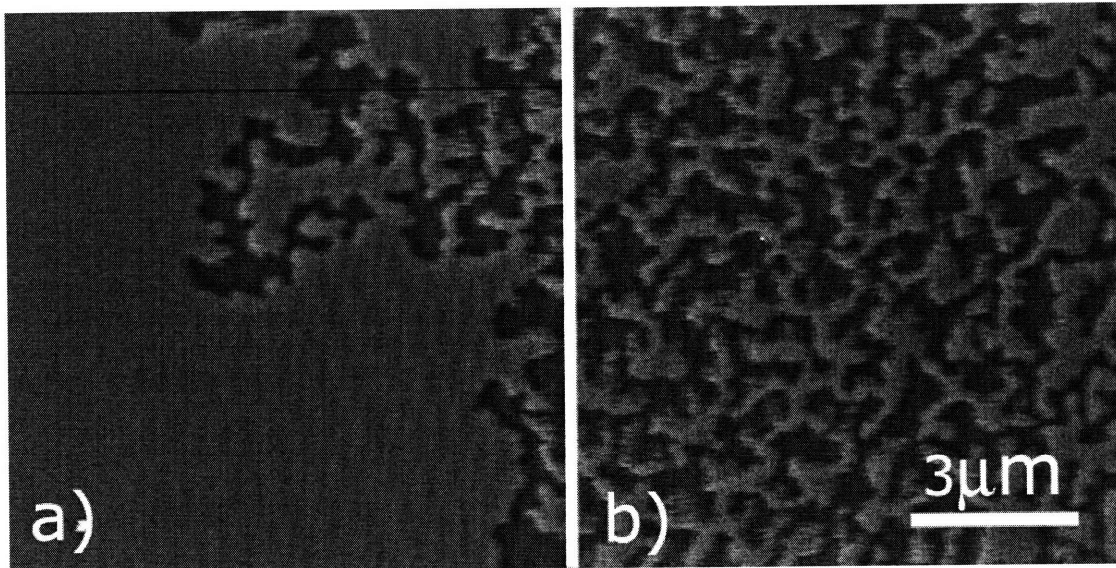

Figure 4-13: MFM images taken at remanence with a net zero moment of the sample (equal amount of 'up' and 'down' domains). For a) the sample was first saturated, then a reverse field of 355 Oe was applied for 30 seconds. b) a short-duration higher field (435 Oe for 200ms) was applied. Image area is 10×10μm, phase height is 7 degrees, light gray regions correspond to reversed domains. Notice the finer domain wall structure present in case b).

been reported for single-layer perpendicular films[34].

Magnetic Force Microscopy (MFM) images of domain pattern in the thick CoCrPt layer are shown in Figure 4-13. The remanent images correspond to different field histories, both resulting in zero net moment. For Figure 4-13 a), after saturating the sample in negative field, a positive field of 355 Oe (i.e. a field just past the start of the high-field step) was applied for 30 seconds, and the field was removed. The sample shows large (at least several tens of microns across) domains interspersed with regions of maze-like patterns, and suggests the nucleation of relatively few domains followed by extensive domain growth during the 30 sec hold time. The single domain on the left side of Figure 4-13 a) extends beyond the range of the scan field of the instrument. In contrast, Figure 4-13 b) shows the domain pattern obtained by applying a short field (435 Oe for 200ms) to a sample after negative saturation. In this case, small maze-like domains are present throughout the entire sample. These domains have much finer details than seen in Figure 4-13 a), and no large domains were observed. This observation suggests that the higher reverse field resulted in more extensive nucleation, but domain growth was suppressed when the reverse field was removed.

The time-dependent measurements at the high-field step show that the magnetization asymptotes towards a value which is not fully saturated. This is seen for all values of H_{rev} within the high-field step and is attributed to small bubble domains that are magnetistatically stabilized by the surrounding regions of the film[37], and therefore require larger fields for annihilation. Thinner films (such as the 5nm layer) do not exhibit this behavior.

4.5 Conclusions

Thin magnetic films of CoCrPt were deposited on a Ti seed layer. Films have strong out-of-plane magnetocrystalline anisotropy which is very sensitive to oxygen contamination during film deposition. To achieve good out of plane behavior the oxygen content in the chamber must be minimized, and more than 0.5% oxygen present in the atmosphere during deposition will disrupt the good texturing of the films.

Perpendicular pseudo spin valve films were grown using RF magnetron sputtering. Hysteresis loops show independent cycling of the thin 'free' layer. A slow time-dependent magnetization reversal is attributed to growth of reverse domains which can occur at a lower field than domain nucleation. Magnetic force microscope images show that the domain sizes and distribution can be tailored via the field history of the film.

References

[1] L. I. Maissel and R. Glang, *Handbook of thin film technology*. New York: McGraw-Hill, 1970.

[2] J. D. Plummer, M. Deal, and P. B. Griffin, Silicon VLSI technology: fundamentals, practice and modeling / James D. Plummer, Michael Deal, Peter B. Griffin. Upper Saddle River, NJ: Prentice Hall, 2000.

[3] S. A. Campbell, *The science and engineering of microelectronic fabrication*, 2nd ed. New York: Oxford University Press, 2001.

[4] M. Konuma, *Plasma techniques for film deposition*. Harrow, U.K.: Alpha Science International, 2005.

[5] L. Holland, *Vacuum deposition of thin films*. London: Chapman & Hall, 1956.

[6] B. N. Chapman, Glow discharge processes: sputtering and plasma etching. New York: Wiley, 1980.

[7] W. R. Grove, "On the Electro-Chemical Polarity of Gases," *Philosophical Transactions of the Royal Society of London*, vol. 142, pp. 87, 1852.

[8] I. Langmuir and K. T. Compton, "Electrical Discharges in Gases Part II. Fundamental Phenomena in Electrical Discharges," *Reviews of Modern Physics*, vol. 3, pp. 191, 1931.

[9] K. H. Kingdon and I. Langmuir, "The Removal of Thorium from the Surface of a Thoriated Tungsten Filament by Positive Ion Bombardment," *Physical Review*, vol. 22, pp. 148, 1923.

[10] L. Tonks and I. Langmuir, "A General Theory of the Plasma of an Arc," *Physical Review*, vol. 34, pp. 876, 1929.

[11] F. Paschen, "Ueber die zum Funkenübergang in Luft, Wasserstoff und Kohlensäure bei verschiedenen Drucken erforderliche Potentialdifferenz," *Annalen der Physik*, vol. 273, pp. 69-96, 1889.

[12] R. C. O'Handley, Modern magnetic materials: principles and applications. New York: Wiley, 2000.

[13] N. Sato, "Crystallographic structure and magnetism of Co-Pd and Co-Pt films with an artificially layered structure," *Journal of Applied Physics*, vol. 64, pp. 6424, 1988.

[14] R. F. C. Farrow, G. Harp, D. Weller, R. F. Marks, M. F. Toney, A. Cebollada, and T. A. Rabedeau, "MBE-growth of chemically-ordered Co-Pt and Fe-Pt alloy phases," Los Angeles, CA, USA, 1994.

[15] T. Suzuki, "Coercivity mechanism in (Co/Pt) and (Co/Pd) multilayers," *IEEE Transactions on Magnetics*, vol. 31, pp. 4085, 1995.

[16] C. J. Lin, G. L. Gorman, C. H. Lee, R. F. C. Farrow, E. E. Marinero, H. V. Do, H. Notarys, and C. J. Chien, "Magnetic and structural properties of Co/Pt multilayers," *Journal of Magnetism and Magnetic Materials*, vol. 93, pp. 194, 1991.

[17] P. F. Carcia, "Perpendicular magnetic anisotropy in Pd/Co and Pt/Co thin-film layered structures," *Journal of Applied Physics*, vol. 63, pp. 5066, 1988.

[18] B. D. Hermsmeier, R. F. C. Farrow, C. H. Lee, E. E. Marinero, C. J. Lin, R. F. Marks, and C. J. Chien, "Magnetic anisotropy and structural characterization of Co/Pt superlattices grown along selected orientations by molecular-beam epitaxy," San Diego, CA, USA, 1991.

[19] C. H. Lee, R. F. C. Farrow, B. D. Hermsmeier, R. F. Marks, W. R. Bennett, C. J. Lin, E. E. Marinero, P. D. Kirchner, and C. J. Chien, "Molecular beam epitaxial growth and magnetic properties of Co-Pt superlattices oriented along the [001], [110] and [111] axes of Pt," Strasbourg, France, 1991.

[20] K. Oikawa, G. W. Qin, T. Ikeshoji, O. Kitakami, Y. Shimada, K. Ishida, and K. Fukamichi, "Thermodynamic calculations of phase equilibria of Co-Cr-Pt ternary system and magnetically induced phase separation in the FCC and HCP phases," *Journal of Magnetism and Magnetic Materials*, vol. 236, pp. 220, 2001.

[21] S. Iwasaki, Y. Nakamura, and K. Ouchi, "Perpendicular magnetic recording with a composite anisotropy film," New York, NY, USA, 1979.

[22] A. G. Roy and D. E. Laughlin, "Effect of seed layers in improving the crystallographic texture of CoCrPt perpendicular recording media," *Journal of Applied Physics*, vol. 91, pp. 8076-8078, 2002.
[23] C. J. Sun, G. M. Chow, J. P. Wang, E. W. Soo, and J. H. Je, "Investigation of the crystallographic texture and interface roughness on CoCrPt /Ti magnetic thin films," *Journal of Applied Physics*, vol. 93, pp. 8725-8727, 2003.
[24] M. Futamoto, K. Terayama, K. Sato, N. Inaba, and Y. Hirayama, "Crystallographic and magnetic properties of CoCrPt thin films investigated using single-crystal perpendicular magnetic thin film samples," presented at Magnetic and Electronic Films - Microstructure, Texture and Application to Data Storage, Apr 1-4 2002, San Francisco, United States, 2002.
[25] I. S. Lee, H. Ryu, H. J. Lee, and T. D. Lee, "Role of a paramagnetic amorphous CoZr seed layer in CoCrPt/Ti perpendicular recording media," *Journal of Applied Physics*, vol. 85, pp. 6133-5, 1999.
[26] H. Laidler, L. Holloway, and K. O'Grady, "Crystallographic defects in CoCrPt thin film media: effect on interactions and magnetic viscosity," *Journal Of Physics D-Applied Physics*, vol. 35, pp. 512-519, 2002.
[27] M. Takahashi, A. Kikuchi, J. Nakai, and H. Shoji, "Effect of ultraclean sputtering process on Cr segregation in CoCrTa thin film media," *Journal of Magnetism and Magnetic Materials*, vol. 193, pp. 79, 1999.
[28] M. Takahashi, "Control of microstructure and magnetic properties in thin film disk by an ultra clean sputtering process," *Materials Chemistry and Physics*, vol. 51, pp. 15, 1997.
[29] M. Takahashi, M. Tsunoda, and H. Shoji, "Ultra-clean sputtering process for magnetic thin films on hard disk drives," *Vacuum*, vol. 59, pp. 814, 2000.
[30] L. Meng-Shian, L. Chih-Huang, L. Yu-Yi, W. Zhi-Hao, H. Sheng-Huang, and J. Ruo-Fan, "Perpendicular giant magnetoresistance composed of [Co/Pt] multilayer and CoFe/TbCo," *Journal of Applied Physics*, vol. 99, pp. 08T106, 2006.
[31] F. Garcia, F. Fettar, S. Auffret, B. Rodmacq, and B. Dieny, "Exchange-biased spin valves with perpendicular magnetic anisotropy based on (Co/Pt) multilayers," *Journal of Applied Physics*, vol. 93, pp. 8397, 2003.
[32] S. Van Dijken, M. Crofton, M. Czapkiewicz, M. Zoladz, and T. Stobiecki, "Magnetization reversal and field annealing effects in perpendicular exchange-biased CoPt multilayers and spin valves with perpendicular magnetization," *Journal of Applied Physics*, vol. 99, pp. 083901, 2006.
[33] Y. Ding, J. H. Judy, and J.-P. Wang, "Magnetoresistive sensors with perpendicular magnetic anisotropy," *Journal of Applied Physics*, vol. 97, pp. 10N704, 2005.
[34] A. Kirilyuk, J. Ferre, V. Grolier, J. P. Jamet, and D. Renard, "Magnetization reversal in ultrathin ferromagnetic films with perpendicular anisotropy," *Journal of Magnetism and Magnetic Materials*, vol. 171, pp. 45, 1997.
[35] J. Pommier, P. Meyer, G. Penissard, J. Ferre, P. Bruno, and D. Renard, "Magnetization reversal in ultrathin ferromagnetic films with perpendicular anisotropy: domain observations," *Physical Review Letters*, vol. 65, pp. 2054, 1990.
[36] F. Ilievski, J. C. Perkinson, and C. A. Ross, "Magnetic reversal phenomena in pseudo-spin-valve films with perpendicular anisotropy," *Journal of Applied Physics*, vol. 101, pp. 09D116, 2007.
[37] A. Hubert and R. Schäfer, *Magnetic domains: the analysis of magnetic microstructures*. Berlin; New York: Springer, 1998.

Chapter 5
Magnetic dot arrays

Patterning magnetic materials is a specific application of block copolymer lithography. This section will describe this particular study from the materials choice to the exact processing methods used. First, forming the PS-PFS block copolymer mask is discussed. Next, the full multilayer process is described, and lastly details of the pattern transfer process are covered. We then analyze the magnetic properties of the fabricated arrays and compare the results to micromagnetic simulation.

5.1 Introduction

Magnetic nanodot arrays have recently drawn significant attention both for fundamental studies of magnetic phenomena as well as for applications in high-density patterned magnetic media[1, 2]. Naito et al. have demonstrated a process of patterning CoCrPt magnetic layers using a mask of self-assembled polystyrene-polymethylmethacrylate block-copolymer combined with spin-on-glass for increased etch selectivity. They report on fabricating islands with pitch of 80 nm and diameter of

40 nm [3]. In previous work, we have shown that nano-scale structures can be manufactured by direct pattern transfer from a self-assembled diblock copolymer film with high etch selectivity between the blocks[2, 4]. Previously this technique was applied to fabricate close-packed magnetic dot arrays of 5-20 nm thick Co and NiFe with periodicity of 56 nm and dot diameters of 34 nm. The dot arrays have an in-plane magnetization direction and coercivities of up to 228 Oe for the Co and 160 Oe for NiFe arrays. Magnetic characterization showed strong magnetostatic interactions between the dots: the switching volume of NiFe and Co arrays was 2-6 times the physical volume suggesting that several dots switch collectively[4]. These samples behaved as arrays of strongly-interacting single-domain particles with in-plane magnetization, which makes them unsuitable for patterned media applications. In the present work we have patterned thin films with perpendicular magnetic anisotropy. We have made 49 and 36 nm period arrays of perpendicular CoCrPt dots with diameters of 34 and 28 nm respectively and thicknesses of 5, 10 and 15 nm. This section describes the fabrication process, hysteresis loops and time-scale dependent magnetic properties of these arrays[5].

5.2 Methods for etching materials

5.2.1. Introduction

In Europe, goldsmiths and metalworkers decorated metal items, such as armor, weapons and household items by etching intricate patterns into them since the Middle Ages, and probably even earlier. Albrecht Dürer, one of the greatest creators of old master prints, experimented with etching to use it as a printmaking medium. The artist was able to create a complex image with a wide range of tones by a laborious multi-step process[6]. Modern day microelectronics relies on the same concept – protect the

surface and define features, and using a certain chemical (or physical) process, transfer the pattern into underlying layers.

While wet etching is still in use, especially in MEMS processes and non-critical steps in microelectronics, it has diminished in popularity. A comprehensive review of chemical etching processes can be found in reference [7]. The work in this thesis heavily relied on dry etching, and a short description of the processes will be reviewed here.

As the name suggests, dry etching does not involve the use of liquids and is a category which is more properly labeled as plasma-assisted etching. Today's integrated circuit fabrication would not be possible without the advent of the dry etching processes. Dry etching can be highly anisotropic and performs a more faithful mask-to-substrate pattern transfer, which has enabled higher packing density in interconnects. Dry etching can be categorized into three categories (1) chemical dry etching, (2) ion-enhanced etching and (3) physical etching processes. The first category includes processes such as plasma etching in barrel-type systems; reactive ion etching, ion-assisted reactive etching and high-density plasma etching fall into the second category; ion beam etching (ion milling) or sputter-etching in the third. Reactive ion etching (RIE) and ion beam etching (IBE) were extensively used for the work performed in this thesis and will therefore be reviewed in more detail.

RIE is performed in a chamber similar to the sputtering system discussed in Chapter 4. In the RIE system a low pressure (1 – 100 mtorr) reactive gas is introduced in the chamber. By applying a high electric field across the electrodes, a plasma is started which, besides free electrons and neutral molecules, will contain excited and/or ionized molecules and molecule fragments and free radicals. The ionized species are accelerated towards the cathode where the sample being etched is placed. Depending on the material etched different etch chemistries (different reactive gasses) are used. For example, to

etch inorganic materials, such as silicon, silica and silicon nitride, gases used typically contain halides (such as CF_4, CHF_3, Cl_2 or HBr). For etching organic materials, O_2 is typically used. Using mixtures is not uncommon, as well as using a buffering (or diluting) gas to slow down the etch rates.

In the plasma there are two species that are active during etching – namely ionic species and reactive neutral species. If etching was performed only by ionic species, we would have simple physical etching, which is highly anisotropic, but also not very selective. If etching was performed by the reactive species only, a pure chemical etching would take place which is typically isotropic, but extremely selective. In the middle, we have the ion-enhanced or ion-assisted etching. This is the true RIE process as most RIE systems are optimized for this regime. Ion-enhanced etching has the best qualities of physical and chemical etching simultaneously – it is both directional (anisotropic) and highly selective. While there is no one unified theory on the exact mechanism responsible for the highly anisotropic character, it is believed that low penetration of the reactive species at the surface or sidewall passivation is responsible for the high anisotropy achieved in RIE systems [8-10].

While ideal etch processes have infinite etch selectivity between the mask and the material being etched, in reality the mask does undergo some etching during the process. Etch selectivity can be controlled by a choice of materials – selecting a mask that has a high resistivity to the etching gas is a fairly straightforward process. However, because during RIE ionic species are also present, this selectivity cannot be made infinite in majority of the cases. This is particularly problematic for ion beam etching as it relies solely on the physical process of sputtering to perform the etching. As such, it is highly directional as ion fluxes are well collimated, but also not very selective. The directionality

of ion milling is unparalleled[2] in RF sources, and can be controlled to some extent in ion beam sources. The etching process is exactly the same as sputtering, and as a result the selectivity of etching is the ratio of the sputter yields of the mask and substrate.

The most popular source for ion milling is the Kaufman type source that originally was developed as a propulsion system for space travel. Unlike RF sources, Kaufman sources have a direct and independent control over both ion bombardment energy and ion flux[11-13]. An electron filament (cathode) is heated using a current supply which is held at a voltage difference below the anode. This voltage is typically around 40 V to avoid high energy ions from sputtering the inside of the source. Electrons boil off of the cathode and are attracted towards the positively charged anode. While traversing the inside of the gun, they have a chance of colliding with neutral Ar ions which get ionized. These ions are accelerated towards a grid held at a negative voltage and are ejected into a chamber. Acceleration voltages are typically in the range of 500 - 1000 V. If the target being bombarded were insulating, it would quickly charge up as only positive Ar ions are accelerated towards the target. To avoid this, an electron flood gun is typically installed in front of the ion source. It should be noted that the electrons do not recombine with the positive ions in the plasma, but rather neutralize an otherwise positively charged target surface.

[2] In RF processes, ions are highly collimated – a simple calculation, assuming random thermal velocity and *very* modest 20V acceleration gives a maximum angle deviation of less than 0.07 degrees from the normal. In ion beam sources, such as Kaufman sources, this value is higher and varies by design up to 20 degrees at the edges of the beam.

5.3 Patterning perpendicular magnetic films using PS-PFS block copolymer as a mask

5.3.1. Material choice for block copolymer lithography pattern formation

Subtractive patterning of magnetic films provides for an interesting example of the complex material considerations that must be taken into account in order to perform a good pattern transfer from a self assembled block copolymer mask into a functional material. The process used throughout this thesis was adopted from Cheng *et al*[14]. During this research we exclusively utilized polystyrene-polyferrocenyldimethylsilane (PS-PFS) because of the large etch selectivity between the two blocks (8:1)[15].

PFS contains inorganic elements (iron and silicon) in the backbone (Figure 5-1) and therefore resists etching in oxygen plasma by forming a thin layer of silica and iron oxide at the surface of the PFS domain. As a result, a well defined mask is formed which can directly be used to etch into silica, for example. Furthermore, since the PFS mask resists RIE significantly more than a purely organic mask, using the cylindrical morphology is not necessary. Polymers with low etch selectivity between the blocks (purely organic polymers) such as PS-PMMA have low resistance to RIE and must form tall standing cylinders in order to be able to transfer the pattern from the block copolymer into a functional material. PS-PFS forms a good mask, and

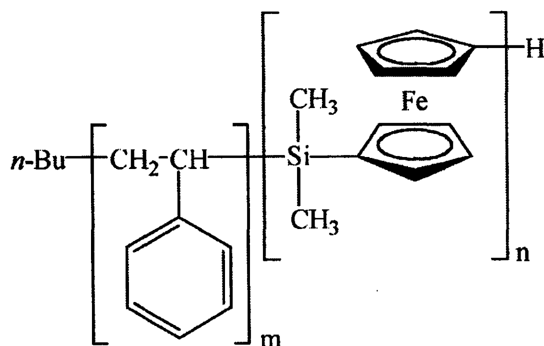

Figure 5-1: Chemical structure of polystyrene-b-polyferrocenyldimethylsilane (PS PFS).

forming tall topographic structures is not necessary as the etch selectivity is provided by the chemistry of the block copolymer. As a result, we bypass the requirements of neutralizing the surface to achieve appropriate directionality of the cylinders, as spheres do not have directionality, which ultimately simplifies our processing.

Polystyrene-polyferrocenyldimethylsilane block copolymers were synthesized in the group of Prof. Julius G. Vancso from the University of Twente. Several molecular weight polymers were used and are referenced in Table 1-1. Anionic polymerization was utilized to synthesize the PS-PFS. First, styrene was polymerized in ethylbenzene initiated by n-butyllithium for a preset time. After the polystyrene block was formed, 1,1'dimethylsilyferrocenophane and tetrahydrofuran were added to form the PFS block. To terminate the polymerization of the PFS, methanol is added to the solution. The polymer is then precipitated in methanol and subsequently sequestered. Gel permeation chromatography gives a polydispersity index of less than 1.1, and volume fractions were measured using ^{1}H- nuclear magnetic resonance (PFS volume fraction is 20% for spherical morphology).

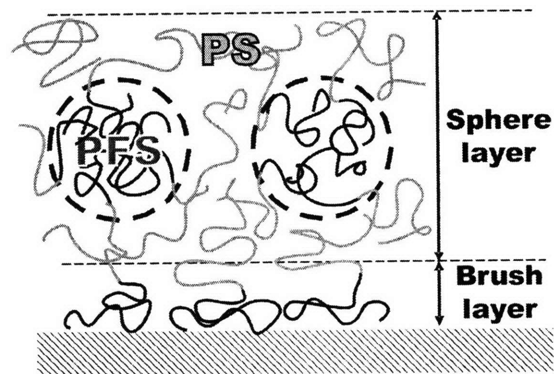

Figure 5-2: Schematic of the arrangement of the polymer chains of PS-PFS at the surface of silica. The PFS preferentially wets the silica surface, and as a minority phase microphase segregates into spheres embedded in a polystyrene matrix.

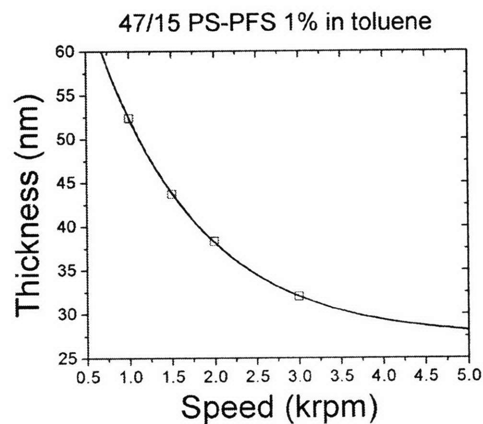

Figure 5-3: A typical spin curve of PS-PFS solution in toluene.

5.3.2. Preparation of block copolymer thin films

For lithographic applications a single monolayer of close-packed spheres on a surface is desirable. At the surface with the silica substrate, the polymer forms a brush layer 10 nm thick as PFS preferentially wets the silica surface, while at the polymer-air surface the polystyrene block segregates preferentially. Control over the thickness of the deposited block copolymer film is required because if the film is too thin, partial dewetting will occur forming areas (islands) where polymer is microphase segregated, and holes where no polymer is present. If the film is too thick, multiple layers of spheres will be formed.

Spin-coating or spin-casting is a standard technique that can be used to deposit uniform thin films of polymers diluted in solvents. For this purpose, the PS-PFS is diluted in toluene at 1-2% (by weight). The thickness of the film depends on the rate (speed) of rotation and on the viscosity of the solution from which the polymer is deposited. Speed control is much simpler and method of controlling the thickness than preparing different viscosities. To correlate the thickness to the speed, after a batch of solution is prepared, a "spin curve" is measured by depositing the polymer at various speeds and measuring the thickness of the deposited film by ellipsometry or AFM. A typical spin curve is shown in Figure 5-3.

Figure 5-4 demonstrates the point of polymer thickness and morphology raised above. At low speeds (Figure 5-4 a), the block copolymer film is too thick to for a single layer of spheres. As a result, two layers of spheres form. As the thickness of the film is reduced (Figure 5-4 c) a single monolayer of spheres forms. To achieve a single layer of spheres the thickness of the block copolymer needs to be about 44 nm. This value is 9 nm larger than the value of the period of the block copolymer, which corresponds to the thickness of the brush layer formed at the silica surface. Further reducing the thickness

results in increasing of the period of the block copolymer, and reducing of the PFS diameter (Figure 5-4 d and e), and lastly regions form without any spheres (holes) because of local dewetting (lower left corner, Figure 5-4 f). This is analogous to previous work on cylinder-forming block copolymers[16] where the film thickness influenced the morphology of the block copolymer. Irregular structures are not desirable for lithography purposes and therefore control of the polymer thickness is important. Typically, after spinning the block copolymer, the thickness of the layer is checked by ellipsometry to determine if the correct thickness has been deposited. Alternatively, upon the first examination of the surface post-anneal with scanning electron microscope it becomes obvious if the correct thickness was achieved or not.

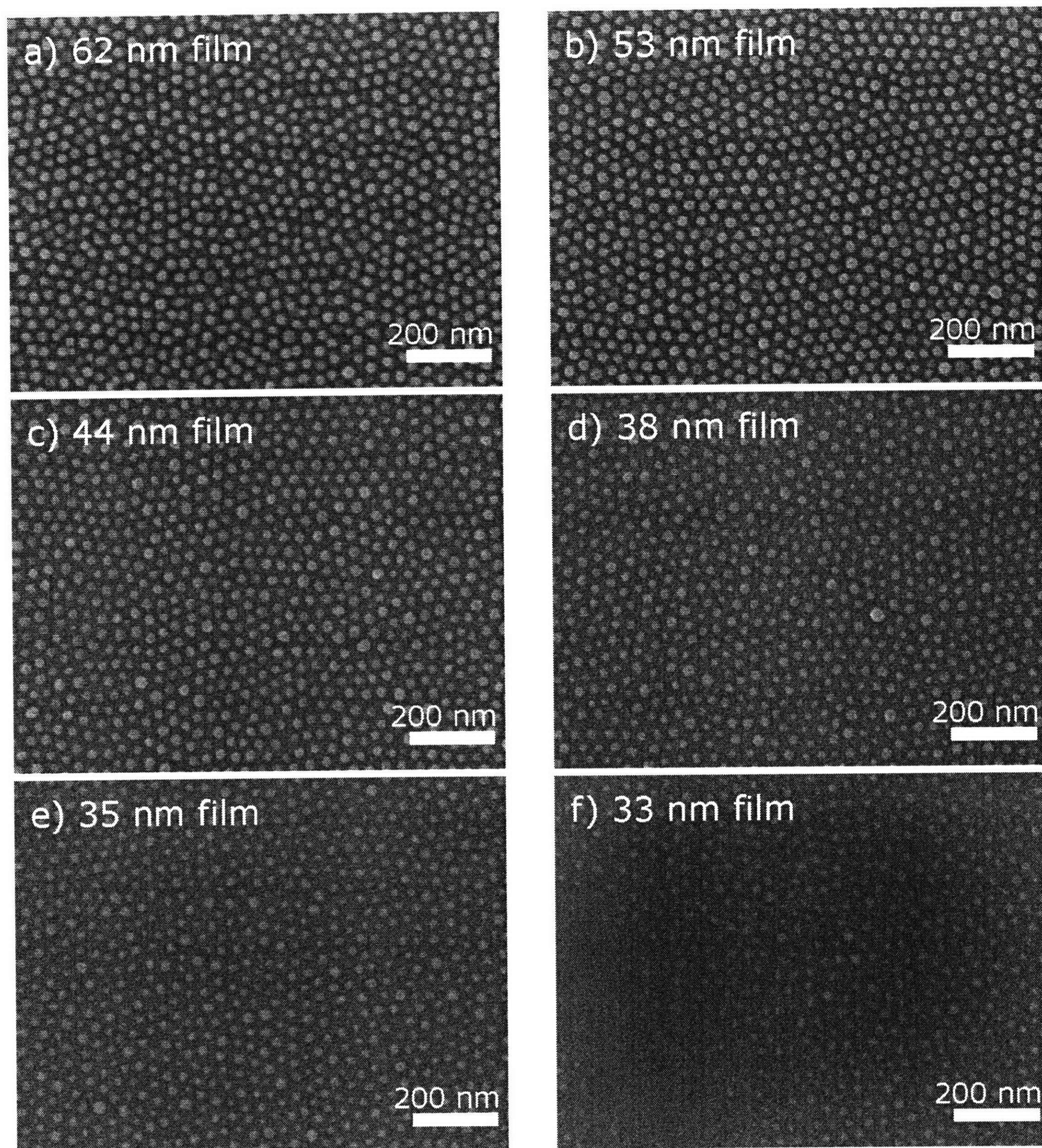

Figure 5-4: Effect of film thickness on the morphology of the self assembled PS-PFS 47/15 block copolymer. 1% solution was spin cast at: a) 750 rpm, b) 1000 rpm, c) 1500 rpm, d) 2000 rpm, e) 2500 rpm and f) 3000 rpm.

5.3.3. Effect of molecular weight on the microphase segregation of PS-PFS

Direct control over the size of the PFS domains and their period is achieved by varying the molecular weight and volume fraction of the polymer used. Reducing the PFS fraction results in the reducing of the PFS domain diameter, to a certain extent. For short block copolymer chains it is energetically favorable to form a disordered melt, rather than to microphase segregate. This is also evident in the phase diagram, where block copolymers with low χN fall in the disordered regime (Figure 3-2). More interesting for lithography applications is the periodicity of the pattern, which can be controlled by a change in the total molecular weight of the block copolymer. As an example, Table 1-1 shows the molecular weights of the block copolymers used in this work. We see a direct correlation between the molecular weight and the period of the morphology; the larger MW 69/21 polymers has a longer periodicity than the smaller MW 33/10 polymer. The period of the microdomains scales as $MW^{1/3}$ (for this polymer the period, $p=2.061\ MW^{1/3} - 44.372$). It should be noted that the kinetics also scale with the molecular weight – larger polymers have higher glass transition temperatures, and have slower diffusion than smaller polymers. As a result, the quality of the pattern formed scales inversely with the molecular weight. A generally accepted parameter of 'quality' is the correlation

Designation	Molecular Weight PS/PFS (Da)	PFS diam. (nm)	Pitch or period (nm)	Correlation length (# periods)
69/21	**69 000 / 21 000**	**34**	**49**	**5**
47/15	**47 000 / 15 000**	**28**	**35**	**7**
33/10	**33 000 / 10 000**	**16**	**29**	**10**

Table 5-1: Molecular weight, size and correlation length of PS-PFS used in this work.

length of the polymer. This value is the average size of an area measured in periods where short range close packed ordering persists. This number can be obtained by counting the number of peaks present in a pair distribution function measured from a top-down SEM. As can be seen, the smaller 33/10 block copolymer has a correlation length of 10, meaning that, on average, each 'grain' in the 'polycrystalline' pattern is on average 10 periods wide. This is particularly obvious in the top-down scanning electron micrographs shown in Figure 5-5 b.

Another aspect of the pattern formation important to lithographic processing is the uniformity of the domain size. Image analysis of the average area of the PFS spheres shown in Figure 5-5 yields a distribution in domain size (diameter) whose standard deviation is 11% for 33/10 and 17% for 69/21. It should be noted that because the diameter of 69/21 PS-PFS is larger, the absolute value by which the diameters vary is proportionally larger. Compared to the read-back tolerances of hard-drive systems which are in the neighborhood of $1\sigma = 10\%$ [17, 18] the smaller 33/10 is on the border of the tolerance for practical application. As discussed previously, PS-PFS has a rather low value of the Flory-Huggins interaction parameter χ and as a result the size distribution is more significant that similar polymers that have a higher value of χ which could be used

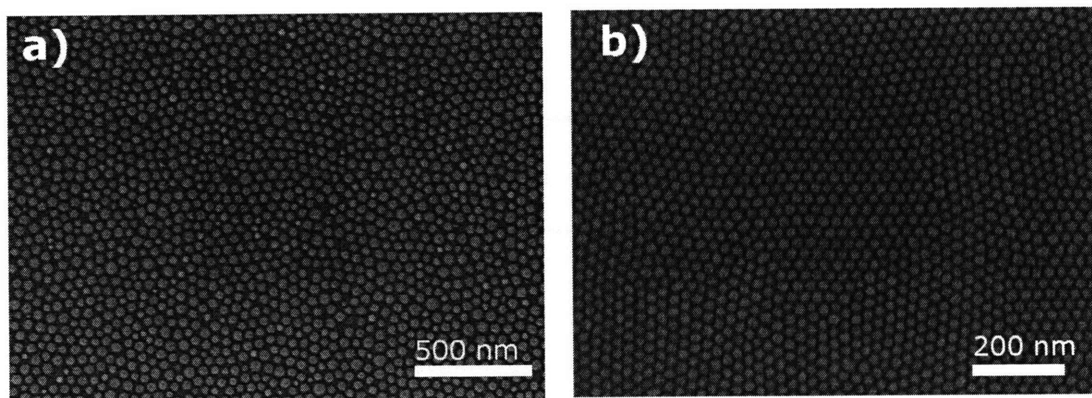

Figure 5-5: Top view micrographs of different molecular weight PS-PFS morphologies on a flat surface: a) 69/21 PS-PFS and b) 33/10. Note the different length scale.

in lieu of PS-PFS for manufacturing applications.

5.3.4. Fabrication of islands with perpendicular magnetic anisotropy using BCP lithography

Even though reactive ion etching would be the most desirable method of etching the magnetic film as it is a process that can transfer small features well and form vertical

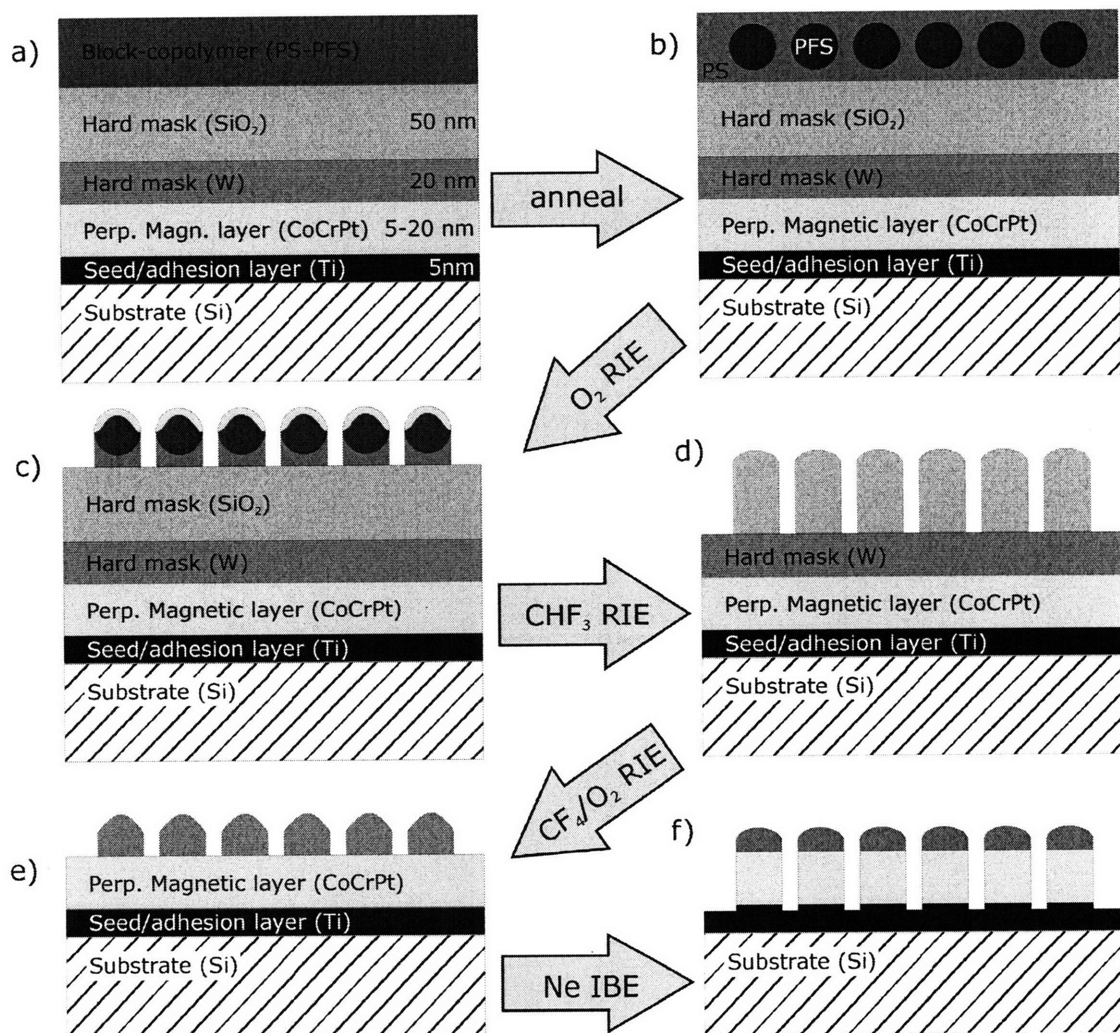

Figure 5-6: Schematic of the pattern formation and transfer process. a) the starting multilayer, which is annealed to induce microphase segregation in the block copolymer; b) monolayer of PFS domains embedded in PS matrix forms; reactive ion etching is used to form and transfer the pattern from b) through e) and ion beam etching transfers the pattern into the magnetic layer f).

side walls, etching magnetic films using RIE is not feasible. Very few transition metals, and no magnetic elements form volatile halide compounds that are a necessary element to the etching process. Therefore, ion beam sputtering is used, and as a result, a hard mask layer of tungsten and silica are used for this purpose. Tungsten is chosen because of better etch selectivity during ion beam etching with respect to the magnetic film and silica is necessary to form a pattern into tungsten[15]. The magnetic layer is Co 66 at% Cr 22 at % Pt 12 at% (CoCrPt) with perpendicular magnetic anisotropy deposited using UHV sputtering on a Ti seed layer as described in detail in Chapter 4. The Ti ensures a

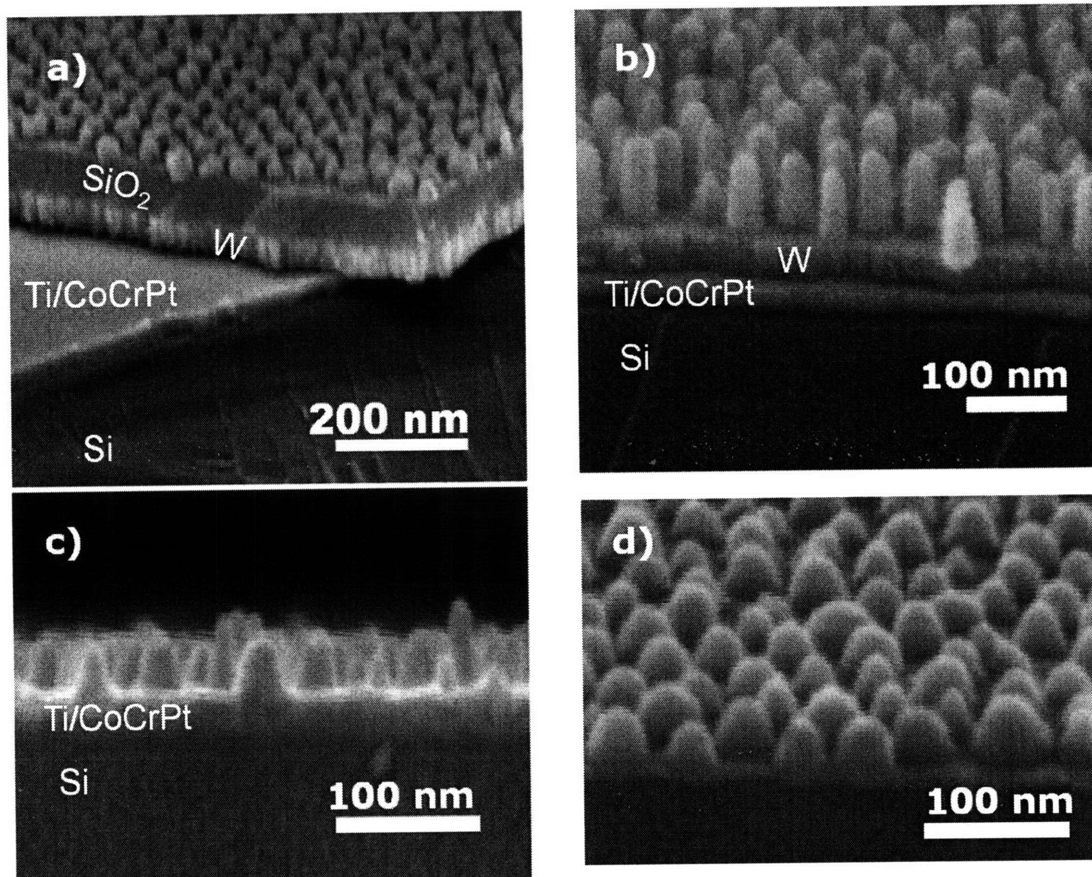

Figure 5-7: Tilted-view scanning electron micrographs at different steps of the pattern transfer. a) PFS spheres on silica surface exposed by RIE, b) silica pillars formed by RIE, c) tungsten caps formed by RIE, d) finished sample by ion milling into the magnetic layer.

perpendicular alignment of the c-axis of Co, and as a result a perpendicular alignment of the easy magnetization axis of the magnetic layer.

Ultimately the stack, represented in Figure 5-6 a), is spin-coated with a 1% solution of PS-PFS and subsequently annealed at 150°-180° C for 24 hours to induce microphase segregation in the block copolymer. After annealing an array of PFS spheres embedded in a PS matrix is formed and the sample is quenched below the glass transition temperature to preserve the structure (Figure 5-6 b). The PS matrix is then removed in oxygen RIE. All reactive ion etching was performed in a PlasmaTherm model 790 RF plasma reactive ion etcher. To minimize the degradation of the PFS domains, the RIE process has been optimized such that it utilized a low bias (5-7 V) and low power (90 W) at 6 mtorr pressure. To achieve slower etch rates and a gentler etch, the oxygen pressure is lowered from the typical 10 mtorr value for RIE processes. This etch gives good selectivity between the two blocks which is close to 1:9 PFS:PS [15] because the PFS domains form a 'skin' of non-volatile inorganic oxides thereby protecting it from the chemical attack by oxygen radicals (Figure 5-6 c). Low bias ensures that removal of the layer by sputtering is minimized. Figure 5-7 a) shows the PFS spheres that have been exposed by RIE on the silica surface (darker band layer beneath the spheres).

Next, the pattern is transferred into silica, forming silica pillars. This step is also done using RIE, except the parameters are modified to optimize for etching of silicon dioxide. CHF_3 is used as the reactive gas at 10 mtorr, and the bias is increased to 150 V and consequently the power is 300 W. Etching silicon dioxide in CHF_3 mainly forms volatile byproducts of SiF_4, CO/CO_2, H_2/H_2O, all of which are pumped out. Using a low bias seems to deteriorate the masking PFS domains, and they appear to coalesce which could be due to heating and melting of the sample. Both evaporated silica and sputtered silica seem to etch at the same rate, and have been used interchangeably throughout this

work. As can be seen from Figure 5-7 b), the pattern transfer is good, the selectivity between PFS and SiO_2 is high resulting in straight sidewalls. Over-etching results in degradation of the pattern with reducing the diameters of the pillars and sloped walls.

When the silica pillars have been fully formed and the silica layer has been etched through completely, a new RIE step transfers the pattern into W. For this purpose, the chemistry is changed to 85% CF_4 / 15% O_2 mixture at 10 mtorr and a low bias voltage of 5-7 V and low power of 90 W. Tungsten forms WF_6 under CF_4 plasmas, a volatile byproduct that is removed, and the oxygen is added to reduce the formation of the carbonaceous deposits that might hinder the etching of W, and increase the etch selectivity between the silica and the tungsten. Figure 5-7 c) shows the pattern transferred into the W layer, forming W caps that are going to be used as a hard mask to etch the magnetic layer.

As discussed earlier, Ne ion beam etching is used to transfer the pattern into the magnetic layer using a Kaufman-type [13] source. Ionized Ne^+ ions were accelerated with energies of 500 eV and used to sputter away unprotected material. As can be seen from Figure 5-7 d) because a thin mask was used, no sidewall depositions were formed. It should be noted that even though the images show these islands with rounded tops, the actual magnetic part closely resembles a flat disc, with a diameter equal to the diameter of the PFS domain, and height equal to the thickness of the magnetic film that we started with. The rounded section is the W hard mask that remains and can be selectively removed by more CF_4/O_2.

To study the effect of island size on the magnetic properties of the arrays, two sets of samples were fabricated by using a different molecular weight (MW) of PS-PFS. Sample set A was fabricated using PS-PFS with MW of 69k for PS block and 21k for the PFS block, with PFS domain periodicity of 49 nm and average diameter of 25 nm.

Domain size and pitch was estimated from digitized top-down scanning electron micrographs. The magnetic layer for this set has Hc=160 Oe and is expected to have MS=350 emu/cc, and KU=2×106 erg/cc[19]. Sample set B was fabricated using a PS-PFS with MW of 47k for PS and 15k for PFS, with PFS domain periodicity of 34 nm and average diameter of 28 nm. It should be noted that the magnetic CoCrPt layer for sample set B was inadvertently alloyed with Cu from the target backing plate at concentration of 6.8 at% as measured by depth-profiled Auger spectroscopy. As a result, the M_S = 160 emu/cc, H_C = 160 Oe and K_U=8.2×104 erg/cc as measured by vibrating-sample and torque magnetometry. The large size distribution of the domains is assumed to be due to large polydispersity index (PDI=1.062) of the available PS-PFS block copolymer and low diffusivity / slow kinetics. Samples will be referenced by providing the set letter followed by the thickness of the starting magnetic film, for example A-15 corresponds to the sample in set A fabricated from 15 nm thick CoCrPt film.

As a result of this patterning, we have formed a large-area array of close-packed magnetic islands with crystalline magnetic anisotropy pointing perpendicular to the plane of the substrate. The magnetic properties of this array have been examined and will be discussed in following chapters.

5.4 Magnetic properties of arrays of islands with perpendicular magnetic anisotropy

Magnetic properties of the samples were tracked as a function of the ion beam etching step which patterns the magnetic layer (Figure 5-8). During ion beam etching, the W hard mask protects areas of the sample which correspond to the areas where PFS domains were in the polymer layer. At short etching times, partial etching roughens the surface and magnetic domain nucleation and propagation remain the dominant methods of magnetization reversal. Further etching fully transfers the pattern into the magnetic film which is accompanied by a sharp jump in the coercivity (for example, in sample A-15 the coercivity increases an order of magnitude at the value where the moment is reduced

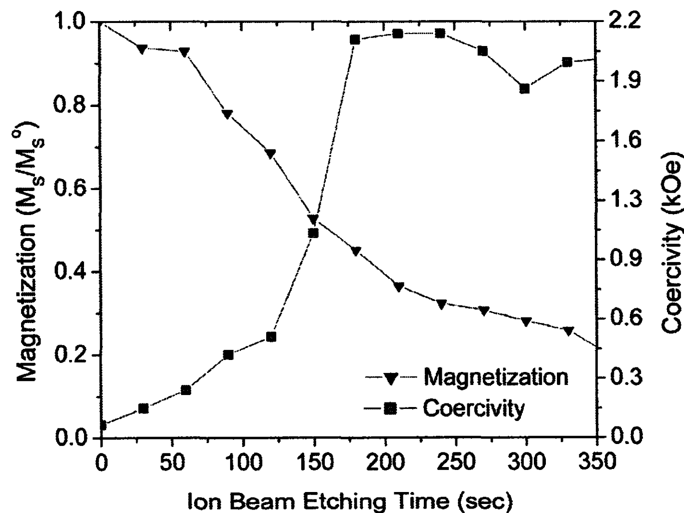

Figure 5-8: Magnetization and coercivity of sample A-15 as a function of ion beam etching time. At short times, partial etching roughens the surface of the magnetic film, the coercivity is increased slightly and the total moment of the sample is reduced as a result of magnetic material being etched away. Further etching fully transfers the pattern into the magnetic film, which is accompanied by a sharp jump in the coercivity. At this point the magnetic islands are physically and magnetically separated from each other. Further ion etching results in pattern degradation by side-wall erosion of the islands accompanied by lowering of the total moment, while the coercivity remains roughly constant.

by 45%). At this point the magnetic islands are physically and magnetically decoupled from each other and the magnetization reversal mechanism changes from domain wall nucleation and propagation to coherent reversal of individual islands, as will be described below. Further ion beam etching results in pattern degradation by side-wall erosion of the islands accompanied by lowering of the total moment, while the coercivity remains roughly constant. The change in coercivity is more pronounced in thicker films, and conversely have a higher island volume when finished (Figure 5-9). The thinnest sample (B-5) shows no change in the coercive field from un-patterned film to fully isolated islands.

Once the patterning is complete, the magnetic film has been sectioned into an array of close-packed disk-shaped islands with a height equal to the film thickness and diameter approximately equal to the diameter of the PFS domain. This array retains the uniaxial anisotropy from the deposited film, and therefore time-scale dependent reversal phenomena can be analyzed following the model developed by Sharrock[20]. This model assumes an array of non-interacting uniaxial particles with aligned easy axes and treats the magnetization reversal as an energy-activated process, where the reversing field

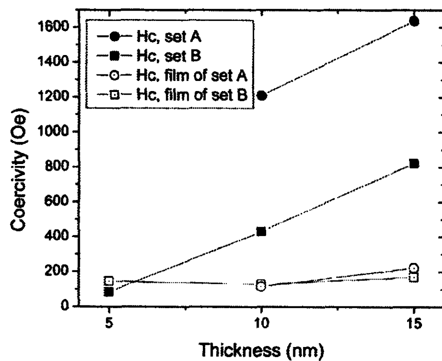

Figure 5-9: Coercivity of unpatterned film, as well as patterned samples. Islands in set A have an average diameters of 34 nm, while those in set B have an average diameters of 28 nm.

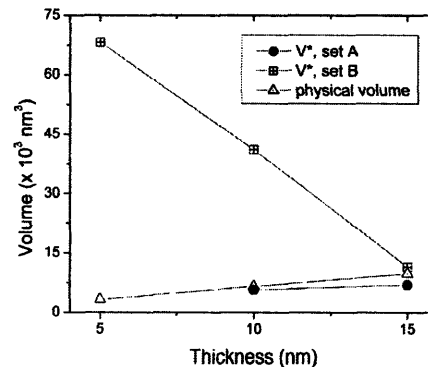

Figure 5-10: Switching volume V* as measured for arrays of uniaxial islands fabricated by block-copolymer lithography.

reduces the energy barrier to switching. By reducing the rate by which the reversed field is swept, the coercivity of the array is reduced as thermal processes have more time to switch the magnetization. Consequently, one can extract a value for a switching volume V^* which corresponds to the minimum volume of magnetic material that reverses its magnetization. If V^* is equal to the physical volume V of the particle, than these particles reverse their magnetization by coherent and independent switching. If V^* is larger than V, then several dots switch collectively. As can be seen from Figure 5-10, A-10, A-15 and B-15 have V^* approximately equal to the physical volume of one island, suggesting coherent and independent switching of each island. A simple calculation using the values for K_U listed above yields a KV value around $300\times k_bT$ for samples in set A, and a more modest $20\times k_bT$ for sample B-15 due to the degraded K_U value from Cu contamination.

Sample B-5 shows significantly different magnetic behavior. Unlike the rest of the patterned and unpatterned samples which exhibit out-of-plane remanent magnetization $M_R \approx 0.8\times M_S$, sample B-5 has $M_R \approx 0.25\times M_S$ and very low coercivity ($H_C = 70$ Oe). The large V^* value for this sample ($V^*=46\times10^3$ nm^3) which is $9\times V_{physical}$ suggests collective reversal of several islands. This value was not much different from the effective value of V^* measured for unpatterned films (20-60×10^3 nm^3). This behavior is likely due to large magnetostatic interactions between neighboring dots, similar to in-plane magnetized samples in our previously reported work[4]. A simple calculation assuming an hcp-packed array of cylinders with

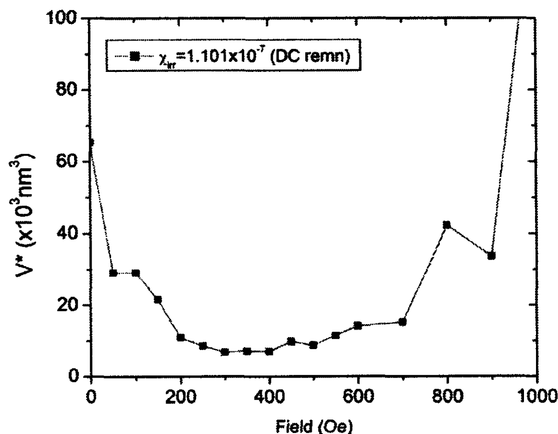

Figure 5-11: V* measured by following the analysis of Wohlfarth[21] for sample B-15.

34nm pitch and 28nm diameter yields a nearest-neighbor total interaction field H_i of around 100 Oe. While this field is negligible for the samples with larger coercivities (such as A-10, A-15 and B-15), sample B-5 has a coercive field H_C comparable to H_i. Furthermore, the *KV* for sample B-5 is about $5 \times k_b T$ at room temperature, making this sample particularly sensitive to thermal effects. Finally, sample B-10 also exhibits a larger V^* than $V_{physical}$. With a $M_R \approx 0.75 \times M_S$ and $H_C = 430$ Oe, B-10 is an intermediate case between B-5 and the rest of the samples. It should be noted that a field-dependent V^* was measured following the analysis of Wohlfarth[21] (Figure 5-11) and we found that the values of V^* obtained agree well with those measured following Sharrock's method[20] (Figure 5-10) over a wide value of applied magnetic fields (200-600 Oe).

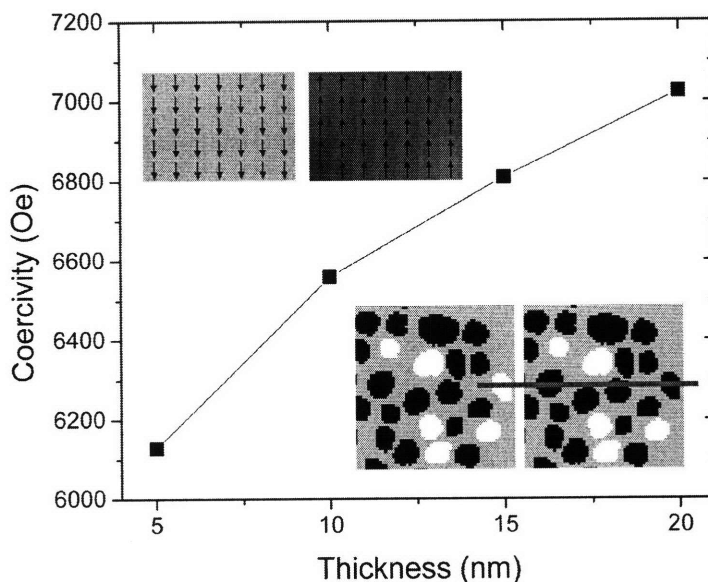

Figure 5-12: Results of micro-magnetic simulation showing coherent and independent reversal of a single island. Inset shows two consecutive stages in the simulation at field difference of 10 Oe. Bottom right shows the top-down view, where a single island can be seen reversing the magnetization abruptly (black islands have the magnetization pointing towards the reader, and white away from the reader). The gray horizontal line depicts the location of the cross-section shown in top-left, where all magnetization vectors are aligned with the vertical c-axis. The varying cell-colors depict the angle of the vector in the basal (substrate) plane consistent with the slight variation of the c-axis programmed into the simulation.

Lastly, as a theoretical confirmation of the reversal mechanism of the islands, a micro-magnetic simulation was carried out using the OOMMF software from NIST[22]. A scanning electron micrograph of a patterned film (sample B-10) was digitized and used for the simulation. Cell-size was set to 4×4×5 nm (x×y×z) and 3D simulations were carried out on stacks consisting of 1-4 layers (corresponding to 5-20nm thickness). To better approximate the sample, a uniaxial anisotropy vector-field was generated with a 5 degree random variation around the c-axis. The value of K_U was taken from measurement (8.2×10^4 erg/cc). The field was applied perpendicular to the plane of the sample. While the magnitude of the calculated coercive field of the array is larger than the measured value, the trend in the simulation, an increase in H_C with thickness, follows the trend in the measurement. Furthermore, the simulation corroborated the independent reversal of each island in coherent fashion.

Long range order necessary for practical applications can be imposed by several methods[23]. A method of topographical ordering using selectively-removable polymeric templates has been developed and will be discussed in Chapter 6.

5.5 Conclusion

A series of 2D close-packed islands with varying sizes (5-15 nm thick, 20-35 nm diameter) and with uniaxial anisotropy perpendicular to the substrate have been fabricated using block-copolymer lithography. Magnetic analysis showed that the islands reverse their magnetization in a coherent and independent fashion. One exception is the array of 5 nm thick / 28 nm diameter islands, in which interactions significantly influence the magnetic reversal. Micro-magnetic simulation confirmed the coherent reversal of the thicker islands. More generally, we have shown that block copolymer

lithography with subtractive patterning can be used to fabricate patterns with diameter as small as 28 nm while preserving the magnetic properties of the magnetic film.

References

[1] K. Naito, H. Hieda, M. Sakurai, Y. Kamata, and K. Asakawa, "2.5-inch disk patterned media prepared by an artificially assisted self-assembling method," *IEEE Transactions on Magnetics*, vol. 38, pp. 1949-1951, 2002.

[2] C. A. Ross, H. I. Smith, T. Savas, M. Schattenburg, M. Farhoud, M. Hwang, M. Walsh, M. C. Abraham, and R. J. Ram, "Fabrication of patterned media for high density magnetic storage," *Journal of Vacuum Science and Technology B*, vol. 17, pp. 3168-3176, 1999.

[3] A. Kikitsu, Y. Kamata, M. Sakurai, and K. Naito, "Recent Progress of Patterned Media," *IEEE Transactions on Magnetics*, vol. 43, pp. 3685, 2007.

[4] J. Y. Cheng, W. Jung, and C. A. Ross, "Magnetic nanostructures from block copolymer lithography: Hysteresis, thermal stability, and magnetoresistance," *Physical Review B (Condensed Matter and Materials Physics)*, vol. 70, pp. 064417, 2004.

[5] F. Ilievski, C. A. Ross, and G. J. Vancso, "Magnetic reversal phenomena of perpendicular magnetic islands fabricated by block copolymer lithography," *Journal of Applied Physics*, vol. 103, pp. 07C520, 2008.

[6] M. Stokstad, M. S. Grayson, and S. Addiss, *Art history*. New York: H.N. Abrams, 1995.

[7] J. L. Vossen and W. Kern, *Thin film processes*. New York: Academic Press, 1978.

[8] G. C. Schwartz and P. M. Schaible, "Reactive ion etching of silicon," *Journal of Vacuum Science and Technology*, vol. 16, pp. 410, 1979.

[9] G. S. Oehrlein, J. G. Clabes, and P. Spirito, "Investigation of reactive-ion-etching-related fluorocarbon film deposition onto silicon and a new method for surface residue removal," *Journal of the Electrochemical Society*, vol. 133, pp. 1002, 1986.

[10] G. S. Oehrlein, J. F. Rembetski, and E. H. Payne, "Study of sidewall passivation and microscopic silicon roughness phenomena in chlorine-based reactive ion etching of silicon trenches," *Journal of Vacuum Science & Technology B (Microelectronics Processing and Phenomena)*, vol. 8, pp. 1199, 1990.

[11] J. M. E. Harper, "Ion beam techniques in thin film deposition," *Solid State Technology*, vol. 30, pp. 129, 1987.

[12] N. G. Einspruch and G. B. Larrabee, *VLSI electronics: microstructure science*. New York: Academic Press, 1981.

[13] H. R. Kaufman, J. J. Cuomo, and J. M. E. Harper, "Technology and applications of broad-beam ion sources used in sputtering. Part I. Ion source technology," *Journal of Vacuum Science and Technology*, vol. 21, pp. 725-736, 1982.

[14] J. Y. Cheng, C. A. Ross, V. Z.-H.Chan, E. L. Thomas, R. G. H. Lammertink, and G. J. Vancso, "Formation of a Cobalt Magnetic Dot Array via Block Copolymer Lithography," *Advanced Materials*, vol. 13, pp. 1174-1178, 2001.

[15] J. Cheng, "Fabrication and characterization of nanostructures from self-assembled block copolymers." Ph. D. Thesis, Cambridge: Massachusetts Institute of Technology, 2003.

[16] A. Knoll, A. Horvat, K. S. Lyakhova, G. Krausch, G. J. A. Sevink, A. V. Zvelindovsky, and R. Magerle, "Phase Behavior in Thin Films of Cylinder-Forming Block Copolymers," *Physical Review Letters*, vol. 89, pp. 035501, 2002.

[17] G. F. Hughes and G. F. Hughes, "Read channels for patterned media," *Magnetics, IEEE Transactions on*, vol. 35, pp. 2310, 1999.

[18] B. D. Terris and T. Thomson, "Nanofabricated and self-assembled magnetic structures as data storage media," *Journal of Physics D: Applied Physics*, vol. 38, pp. 199-222, 2005.

[19] N. Inaba, Y. Uesaka, and M. Futamoto, "Compositional and temperature dependence of basic magnetic properties of CoCr-alloy thin films," *IEEE Transactions on Magnetics*, vol. 36, pp. 54-60, 2000.

[20] M. P. Sharrock, "Measurement and interpretation of magnetic time effects in recording media," *IEEE Transactions on Magnetics*, vol. 35, pp. 4414-4422, 1999.

[21] E. P. Wohlfarth, "The coefficient of magnetic viscosity," *Journal of Physics F: Metal Physics*, pp. L155, 1984.
[22] M. J. Donahue and D. G. Porter, "OOMMF User's Guide, Version 1.0," National Institute of Standards and Technology, Gaithersburg, MD NISTIR 6376, National Institute of Standards and Technology, 1999.
[23] J. Y. Cheng, A. M. Mayes, and C. A. Ross, "Nanostructure engineering by templated self-assembly of block copolymers," *Nature Materials*, vol. 3, pp. 823, 2004.

Chapter 6
Directed self assembly of block copolymers

Various applications require high-density ordered nanoscale pattern over a large area, such as plasmon waveguides and bit patterned media. One way of achieving this is by using directed self assembly of block copolymers. As described in previous chapters, various graphoepitaxy methods have been developed to template block copolymer microdomains that could be applied to fabricating large-area arrays of magnetic islands for applications such as patterned magnetic media. All graphoepitaxy methods involve some topographical features which would form a relief pattern when transferred in the magnetic film in addition to the pattern stemming from the block copolymer domain structure (Figure 6-1). For patterned media applications, this proximity is undesirable as it places magnetic wires and islands close-by which may result in superfluous magnetic interactions. Therefore, there is a need of developing a method of directing the self assembly of block copolymer in such a manner that only the block copolymer pattern is transferred in the magnetic layer, but not the template itself, so that tracks may be

separated from each other. This chapter covers two methods that we have developed to address these issues.

6.1 Directed self-assembly of block copolymers using selectively removable topographic templates

6.1.1. Introduction

One method which would satisfy the requirements outlined above is using selectively removable templates for the guided self assembly of block copolymers. The selectively removable template would provide a topographical guide to the ordering and then be removed independently of the block copolymer such that only the pattern of the block copolymer is transferred into functional materials. There are several material requirements that such a template must possess: (1) it must withstand the solvents used for spin-coating the block copolymer, (2) it must tolerate elevated temperatures necessary for the annealing step, (3) it must be immiscible with the block copolymer and (4) it can be removed without affecting the block copolymer. From a structural point of view, we require good control over all dimensions of the template (thickness and width) – the topographical templates must

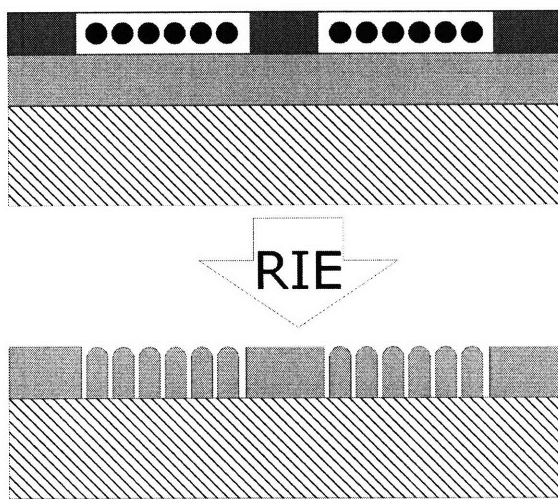

Figure 6-1: A non-removable topographic template used for ordering the microdomains of a block copolymer will transfer into the underlying layers ultimately forming magnetic stripes next to magnetic islands which could have undesirable magnetic interactions.

have heights equal to the height of a monolayer of self-assembled spheres, and the topographic pattern must be simple to fabricate in various widths.

Many polymeric templates satisfy these requirements; a particularly elegant one would be a crosslinked matrix of the majority block of the block-copolymer in use. We found that the BARL-i antireflective coating made by AZ Electronic Materials used for interference lithography is a suitable material. It was designed to withstand a variety of solvents, is routinely exposed to 175° C during the pre-bake and yet it can be removed by

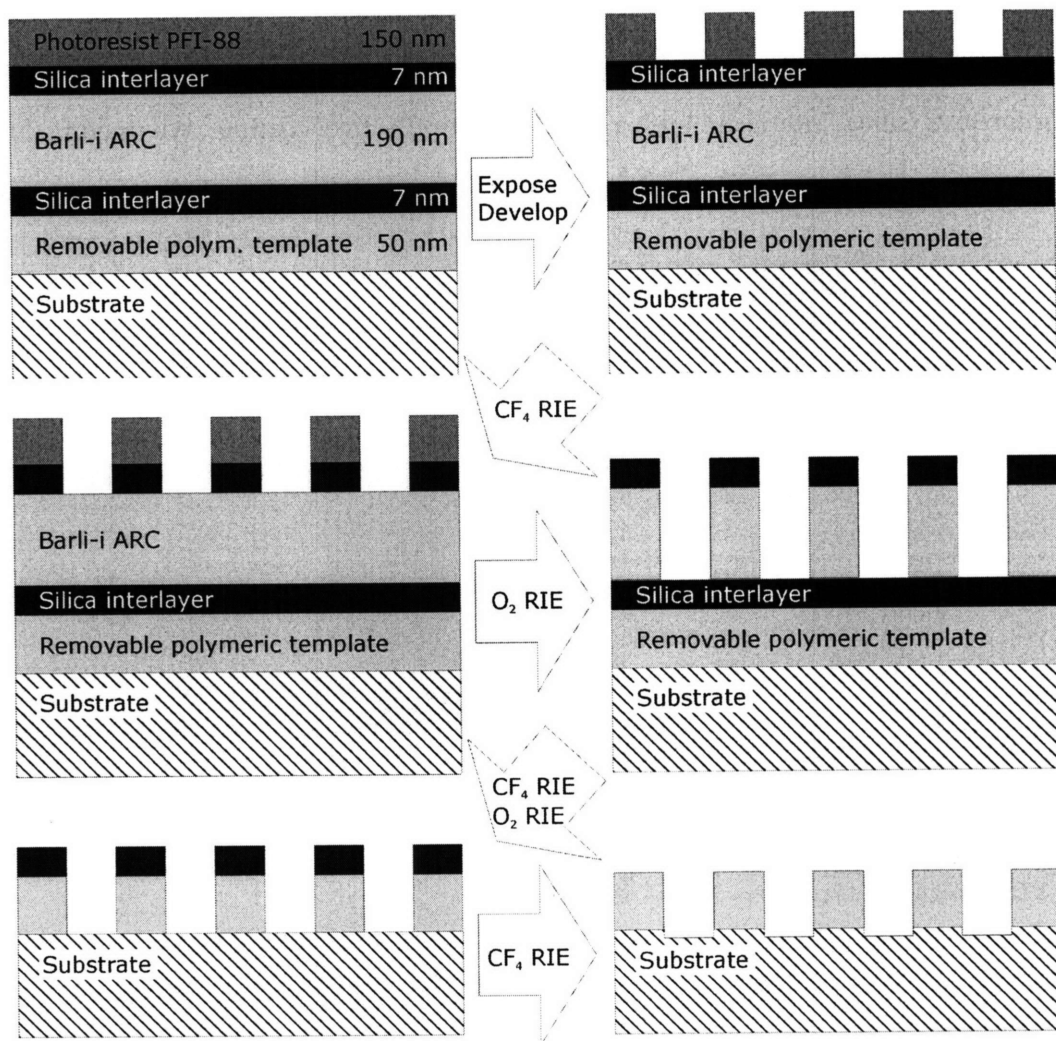

Figure 6-2: Schematic of the process flow for fabrication of selectively removable templates using interference lithography (not to scale).

n-methyl pyrrolidone (nMP). Our goal was to develop a method with wide process latitude such that it can be applied to various materials with small changes. Furthermore, we wanted a process suitable for rapid prototyping so that we may examine different template dimensions with ease. Therefore, we decided to use interference lithography with changes to the standard processing methods.

6.1.2. Fabrication of selectively removable templates using interference lithography

Typical tri-layer resist for interference lithography consists of a layer of photoresist, silica interlayer and a bottom antireflective coating. We modified this method to include another silica layer so that we get good pattern transfer and a fifth

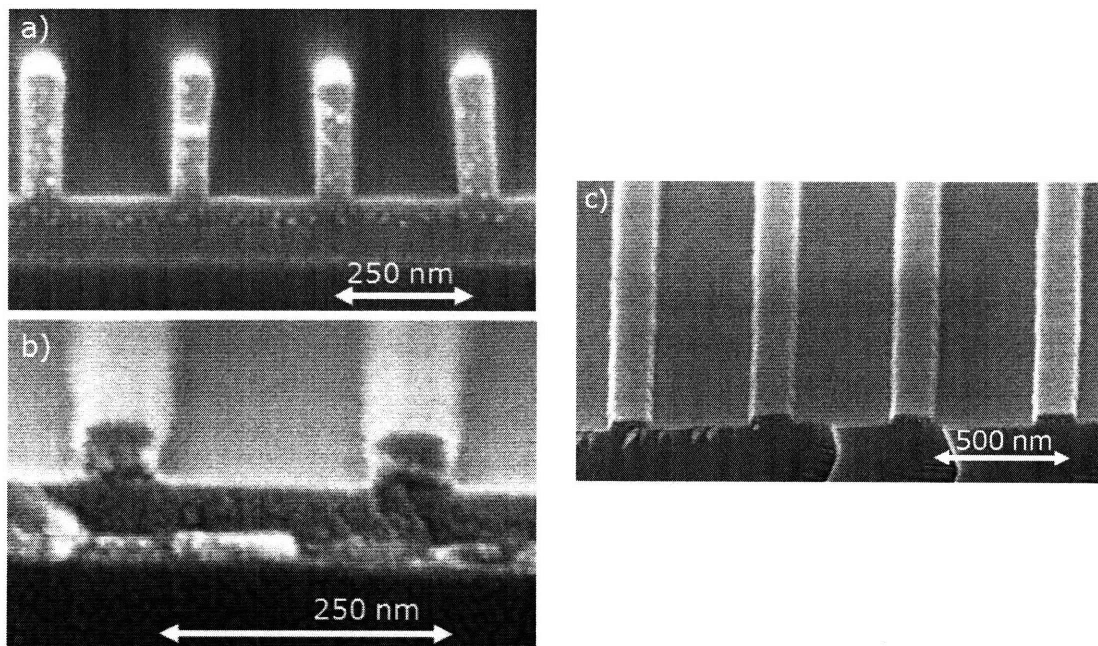

Figure 6-3: a) pattern transferred into the ARC layer, other layers visible (from bottom upwards: dark band on bottom is substrate, brighter band is the Ti/CoCrPt/W layers, medium gray is silica hard mask, layer with spots is the ARC removable template, and a thin silica interlayer is between the free-standing ARC grating and removable template. c) a 500 nm period grating on silicon substrate.

layer which was the actual removable template. The process flow is depicted in Figure 6-2. The thickness of the layers is as follows: removable template (BARL-i ARC) 50 nm, silica interlayers were 7 nm thick (deposited by sputtering), BARL-i ARC layer to minimize back reflections into the photoresist was optimized for the period of the pattern and around 200 nm, photoresist was 150 nm thick.

After exposure in the Lloyd's mirror setup, the photoresist was developed according to standard processing. RIE was used to transfer the pattern from layer to layer until only the removable template remains. The last CF_4 RIE removes the silica from the removable template to allow access for the solvents to attack the template, and consequently slightly etches the exposed area of the substrate.

This five-layer resist can be deposited on top of any stack, and since our goal is transfer of the pattern into a magnetic layer, typically the samples were deposited on the Ti/CoCrPt/W/SiO_2 multilayer described in Chapter 4. Figure 6-3 b) shows the finished grating template and Figure 6-3 a) shows an intermediate step in the grating fabrication. Figure 6-3 c) shows a larger period (500 nm) removable template fabricated on silicon substrate.

6.1.3. Directed assembly of PS-PFS in selectively removable templates

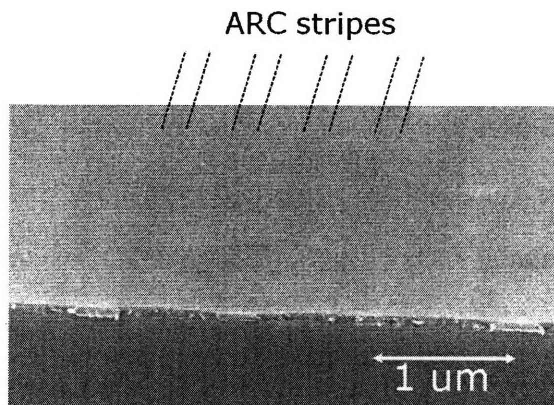

Figure 6-4: Block copolymer solution spin-coated on a grating of a selectively removable template.

The gratings described above were spin-coated with a 1% solution of PS-PFS in toluene so that the film thickness is appropriate to form a single monolayer of self-assembled PFS spheres (Figure

6-4). The sample was then annealed at 150° C for 24 hrs to induce microphase segregation. To expose the PFS spheres, samples were subjected to oxygen RIE step which removed the PS matrix, and partially removed the ARC removable template. In the case of larger period templates, such as the 500 nm period grating shown in Figure 6-5, full template removal was accomplished by a 15 second spin-clean of nMP, followed by 15 second spin-clean of acetone and lastly a 15 second spin-clean of isopropanol. The solvents do not attack the PFS domains as after oxygen etching they are covered with a 'skin' of inorganic oxide which is insoluble in organic solvents. As a result, the block copolymer pattern remains unaffected, yet the template is removed. For smaller period templates, such as the 250 nm period pattern shown in Figure 6-6, the oxygen RIE step is sufficient to remove the template and no solvent cleaning is necessary.

As can be seen from Figure 6-5, in the case of guided self-assembly of 33/10 PS-PFS, long range order extends beyond what was achieved using the same block copolymer on a flat substrate. The block copolymer forms 14 rows of spheres inside the grooves of the pattern, adjusting for slight variations in the groove width by the introduction of a 15th row in a few places. Furthermore, local defects such as dislocations are present but few. It should be noted that the correlation length of this block copolymer is 10 periods, but the micrographs show single-crystal grains that extend at least 200 periods parallel to the groove (well beyond the 10 periods correlation length), and certainly to 14 periods perpendicular to the template. It should be noted however that at such wide templates, the energetic penalty for adding an extra row of spheres is quite low, and therefore defects form easily. As reported previously, the limit to pre-determining the number of template rows extends to templates of up to 10 periods, above which the exact control of number of rows is not possible[1]. This is evident in the presence of dislocations and changes from 14 to 15 rows in several locations in Figure

6-5. To further reduce the number of defects for this particular system and to achieve good control over the number of rows, a narrower template must be utilized.

A 250 nm period template with grooves that were 180 nm wide was used to template the same 33/10 PS-PFS (Figure 6-7). As can be seen from the entire

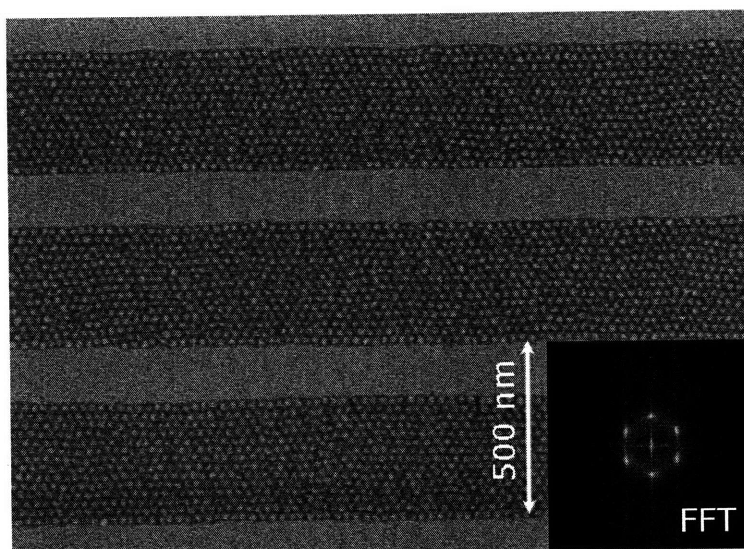

Figure 6-5: Scanning electron micrograph of the guided assembly of PS-PFS in selectively removable template. Polymer forms 14 rows in the groove which is 370 nm wide.

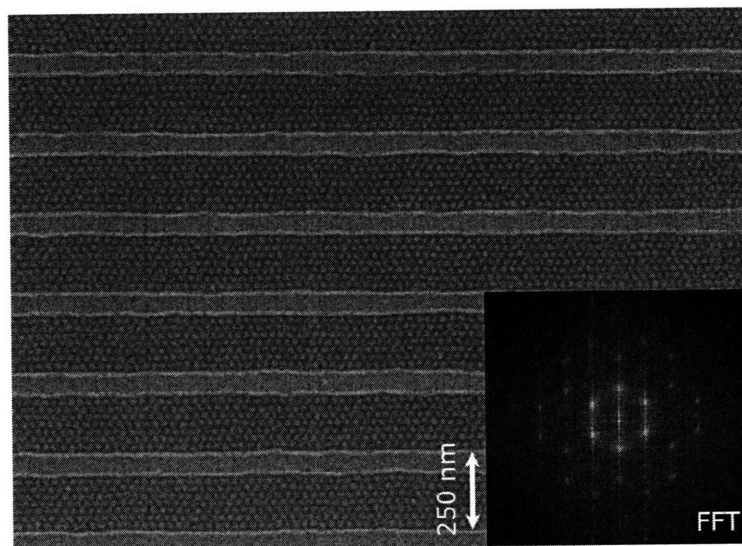

Figure 6-6: Scanning electron micrograph of the guided assembly of PS-PFS in selectively removable template. Polymer forms 7 rows in the groove which is 180 nm wide.

micrograph, there are no defects (vacancies, dislocations) present in this view, and very few can be found throughout the sample. This is not to say that the pattern is perfect – there are regions where the template meanders locally but the block copolymer pattern follows the bends of the template always maintaining the same number of rows and close packed packing.

Lastly, a larger molecular weight 47/15 block copolymer was also ordered in selectively removable templates. While there are regions of good long range order which persist longer than the correlation length of the block copolymer, the ordering is not as good as the ordering of 33/10, which is expected since the kinetics of diffusion of the larger molecule are slower and therefore defects would have a long half-life.

6.1.4. Pattern transfer of ordered arrays into functional materials

Once the pattern has been formed in the block copolymer and the selectively removable template has been removed, we can proceed to transfer the pattern into

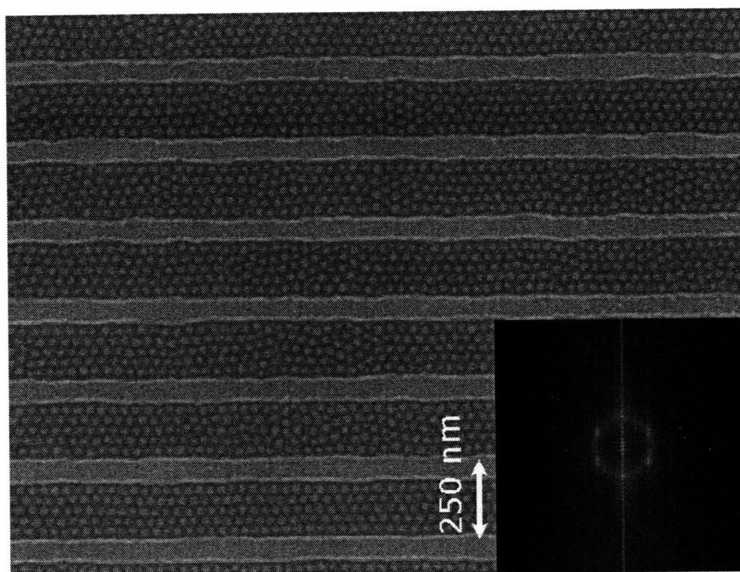

Figure 6-7: Guided self assembly of 47/15 in 250 nm period grooves made of selectively removable material.

functional materials. The process follows the same methodology as the process of transferring disordered arrays. First, using CHF_3 RIE the pattern is transferred into the silica hard mask. Size-dependent etch rate differences becomes obvious as wide exposed areas, such as those beneath the removed template etch slightly slower than the finely-patterned block copolymer posts. Furthermore, the etching is accelerated at the edges of the pattern due to trenching, which is visible in Figure 6-8 a). When the pattern is fully transferred, only the free-standing oxide pillars are visible, and the area where the template was is void of material. Next, the silica posts can be used to transfer the pattern into other functional materials.

In this case, the next step is the formation of a tungsten hard mask. For this purpose, the sample shown in Figure 6-8 is etched under CF_4 / O_2 RIE, which transfers the pattern into the tungsten layer. As can be seen from Figure 6-9, the pattern has been transferred into the tungsten layer similar to the process outlined in Chapter 5. A well-ordered array of 17 nm diameter tungsten islands has been formed over a large area with satisfactory uniformity. The last step is the ion beam etching step using Ne^+ to transfer the tungsten pattern into the magnetic layer. Due to the purely physical etching character of the process, this step does not proceed as uniformly as the RIE steps above. It is debatable how much of this is due to instrument limitations, and not simply due to fundamental limits of the ion beam etching process. As can be seen from Figure 6-10, the pattern has lost its uniformity as compared to Figure 6-9. This is understandable as 17 nm diameter islands are hardly a significant etch mask and likely erode quickly.

Magnetic measurements show modest increase of the coercivity from 100 Oe to 150 Oe while the total moment of the sample is reduced by 60 %. However, it should be noted that this could be due to the complete removal of magnetic material in areas where the etching proceeds at a slightly faster rate and not actually due to segmentation of the

film into islands. In our previous argument that the magnetic layer is fully sectioned into islands assumes uniform etching over the entire area, which is confirmed by SEM examination. In the above case, we were able to localize regions where the etching appeared to have been successful, such as those depicted in Figure 6-10, however there were many areas where no pattern was present.

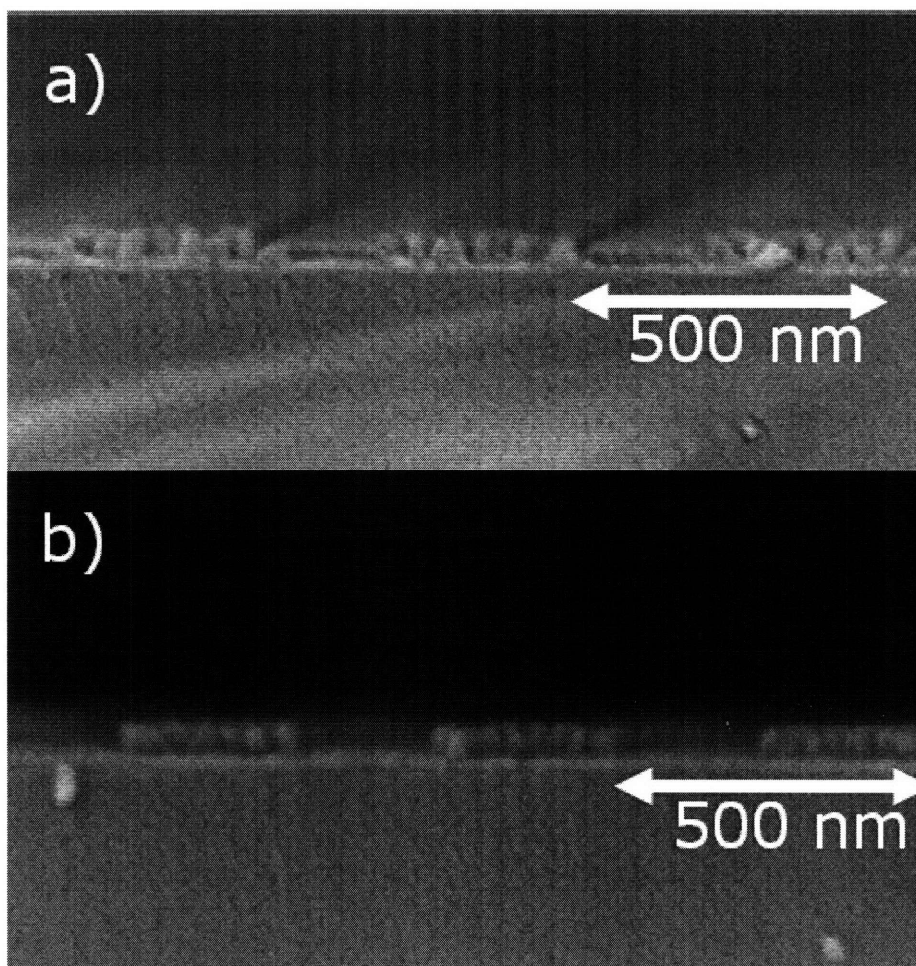

Figure 6-8: Pattern transfer into silica hard mask. a) partially transferred block copolymer pattern into the silica layer – silica pillars are being formed and trenching is visible where the template used to be. b) full pattern transfer into the oxide, free-standing oxide pillars have been formed and the area beneath the removable template is void of material.

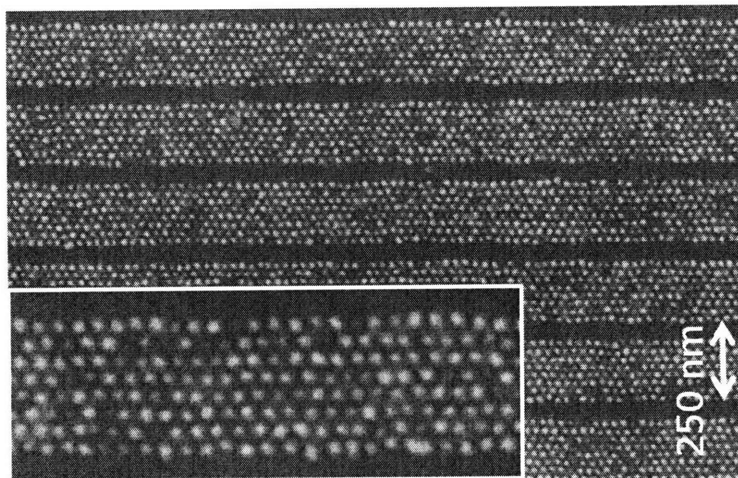

Figure 6-9: Block copolymer ordered patterns by selectively-removable template transferred into tungsten forming a well-ordered array of islands with 17 nm diameter.

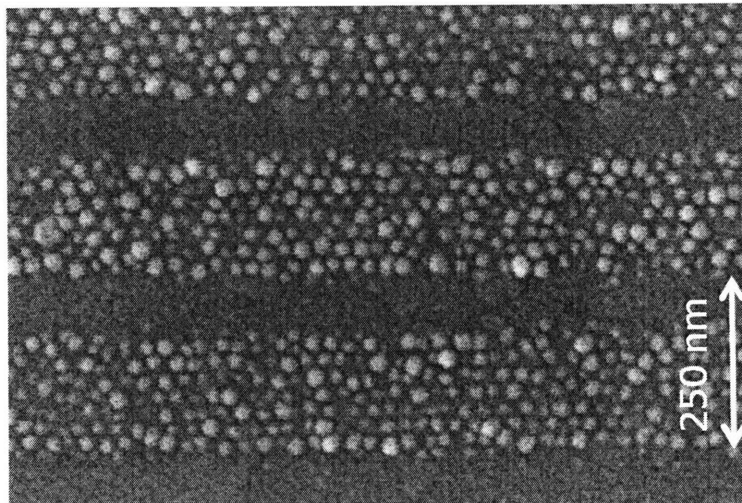

Figure 6-10: Pattern transferred into CoCrPt using ion beam etching.

6.2 Nanoimprint lithography with in-situ annealing

Another approach to the problem of transferring solely the block copolymer pattern and not the template, would be to utilize nanoimprint lithography as a method of guiding the assembly of the block copolymer. Previously, Deng and colleagues have used soft stamping with fluorinated PDMS stamps to form a pattern in PS-PFS, after which the block copolymer was heat-annealed [2] resulting in a poorly ordered pattern. Li used sapphire molds with in-situ annealing to order PS-PMMA with some success[3]. We wanted to explore the nanoimprint with in-situ annealing method to direct the self-assembly of PS-PFS.

The general processing outline for guiding the block copolymer self-assembly by nanoimprint lithography with in-situ annealing is represented in Figure 6-11. A thin layer of block copolymer film is first spin cast on a substrate. The thickness of this layer is lower than the desired thickness[3] to account for the displaced volume beneath the mesas of the imprint mold. The mold is then pressed into the film, and the entire setup is annealed at typical conditions. To lock-in the morphology, the substrate and mold are quenched and subsequently separated.

While commercial nano-imprint tools have become available recently, none are specifically designed for templated self assembly. On one hand, commercial tools often include multi-layer aligning ability, which is of no importance to us. On the other hand, we require maintaining the sample after imprinting under vacuum at elevated annealing temperatures. As a result we needed to develop a system suitable for nanoimprinting block copolymer solutions and annealing them in situ, without special alignment, and

---

[3] The desired thickness is the thickness of one monolayer of spheres, or roughly equal to the period of the block copolymer.

able to apply and maintain loads of several thousand pounds uniformly. For this purpose, a simple press was designed that can fit inside our vacuum oven (Figure 6-12). To apply the large loads, we used a simple lever system that multiplied a clamping load applied at the end of the lever by a factor of 4. The clamping load was estimated using the equation:

$$P = \frac{T}{k \cdot D}$$

where P is the clamping force (load), T is the torque applied on the bolt, D is the bolt diameter, and k is a constant of proportionality that typically has values from 0.1-0.15, depending on the type of bolt used[4]. For non-lubricated bolts (such as the ones we used) this value is 0.15. Using a torque wrench to apply a preset load we were able to apply and maintain loads of up to 7000 kg.

To ensure even load distribution, avoid mold and substrate cracking, isotactic pressure is best suited. However, fluids are problematic to handle, and we needed to be

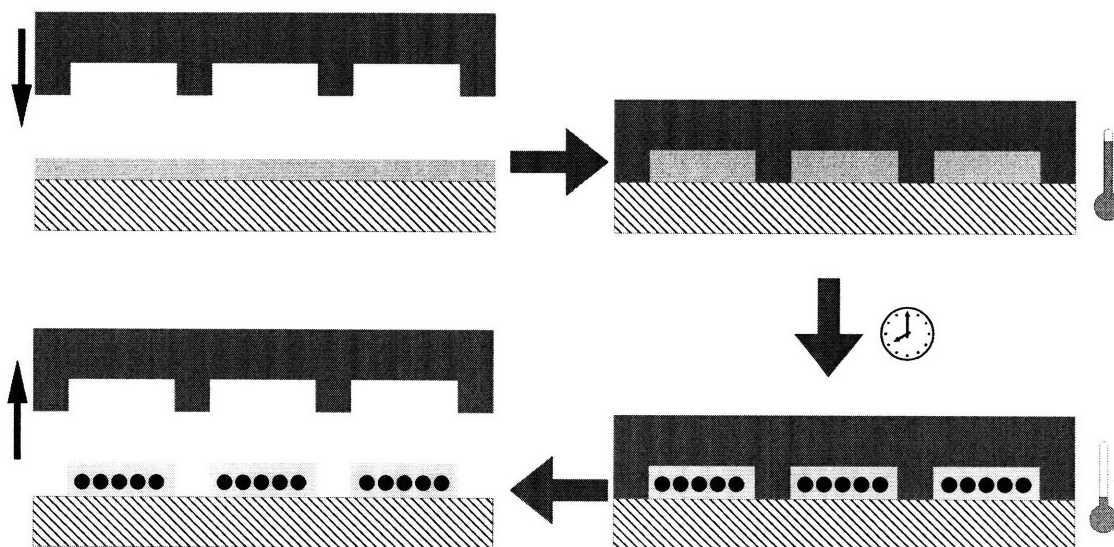

Figure 6-11: Schematic of the process steps in guided self-assembly of block copolymers by nanoimprint lithography and in-situ annealing.

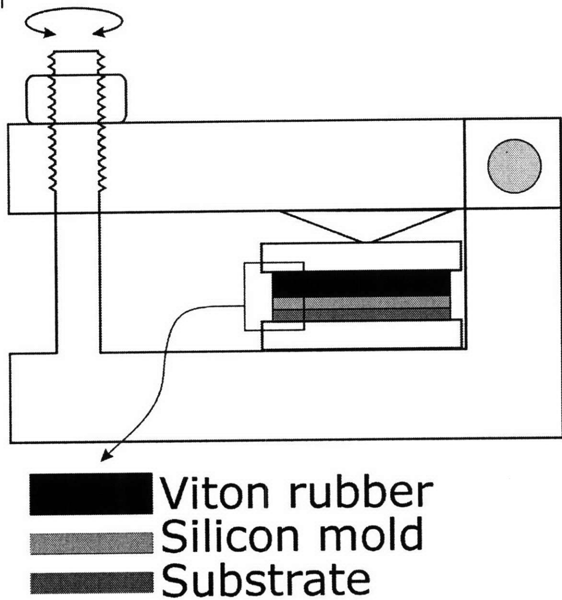

Figure 6-12: Schematic of the nanoimprint press for in-situ annealing.

able to quickly cool the samples. Just placing the mold and substrate between two rigid steel plates concentrates the stress on edges or around dust particles, which are often particles of the silicon wafer which break the mold and/or substrate. A layer of viton rubber was placed above the mold to minimize this load concentration and distribute the load evenly. Viton was chosen because it has operating temperatures between -30° C and 200° C.

To press the samples, the entire press assembly was pre-heated to the annealing temperature, and the substrate and mold were placed in the press and load was applied before immediately placing the entire press inside the vacuum oven. After annealing, the press was removed from the vacuum oven, the sample and mold were removed from the press and quenched to room temperature before separation for further processing.

6.3 Mask fabrication by interference lithography

Nanoimprint lithography's main challenge is the uniformity of contact between the mold and substrate. Molds for step and flash lithography have a small contact area and are typically made from thick rigid quartz flats. This is not suitable for our application as we require large area contact, which is best addressed by using flexible molds. Nitride membranes are too fragile, and therefore we settled on 3" wafers as the molds, which

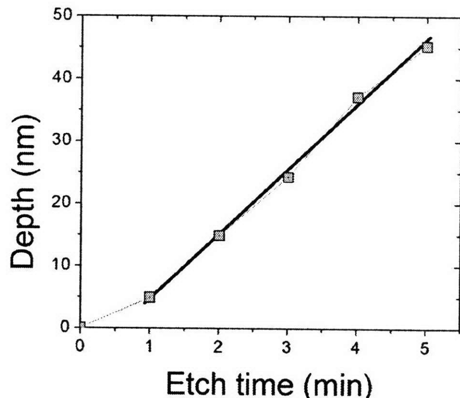

Figure 6-13: Silicon etch depth as a function of etch time in CF_4 RIE, bias 50V, power 70W. Effective etch rate is 10.4nm/min.

balance the flexibility with structural stability. Large area molds were fabricated by a combination of interference lithography and reactive ion etching.

We start by prime (100) silicon wafers with 3 in diameter (nominal thickness 375 μm). Using the process outlined in Chapter 3 we fabricate gratings in Barli-i antireflective coating on the silicon substrate. Using CF_4 RIE, the pattern was then transferred into the silicon, and RCA – 1 clean (5:1:1 H_2O:NH_4OH:H_3O at 80° C) was used to remove the remaining ARC lines. To achieve the appropriate mold depth, the etch rate was carefully calibrated by preparing several samples and measuring their depth using a SPM (Figure 6-13). The effective etch rate was 10.4 nm/min in silicon, under 50 V bias and 70W power. Initially, as can be seen from Figure 6-13, this etch rate is lower because of the surface oxide. Figure 6-14 shows an examples of a grating that was fabricated for this purpose.

6.3.1. Mold treatment with release layer

If the mold is used as prepared without further modification, release problems will arise. The adhesion of the block copolymer to the substrate is equal to that of the mold, as both the mold and substrate are made of the same material; therefore, upon removal the mold pulls off the pattern resulting in poor transfer. This is seen in Figure 6-15 where if the mold is left untreated, serious non uniformities can be seen in close proximity (some regions of good transfer are also present).

To ensure we are getting good pattern transfer during the nanoimprinting step, we used a surface fluorination treatment following Bailey's and Jung's approach [5, 6]. Tridecafluoro, 1, 1, 2, 2, tetrahydrooctyl trichlorosilane (CF_3– $(CF_2)_5$–CH_2–CH_2–$SiCl_3$) (FOS) was obtained from Gelest, Inc. and used as received. RCA-1 cleaned molds were placed inside a vacuum chamber where a small amount of FOS was introduced, and the chamber was evacuated. Vapors of FOS react with any surface-bound water on the mold, releasing HCl in the process. After 5 minutes of exposure, the chamber was vented, and the sample was placed on a 115° C hotplate to fully react any remaining unreacted silane groups. This process forms a self-assembled monolayer (SAM) at the surface of mold rendering a previously hydrophilic surface extremely hydrophobic.

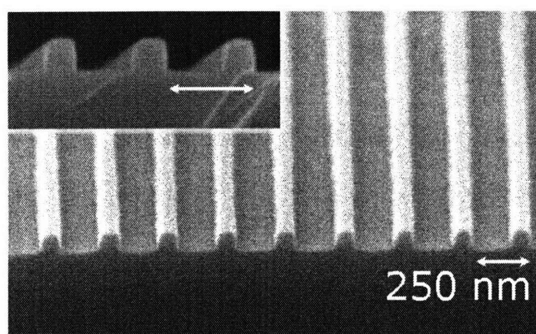

Figure 6-14: SEM micrograph of a 250nm period grating with groove depth of 90 nm.

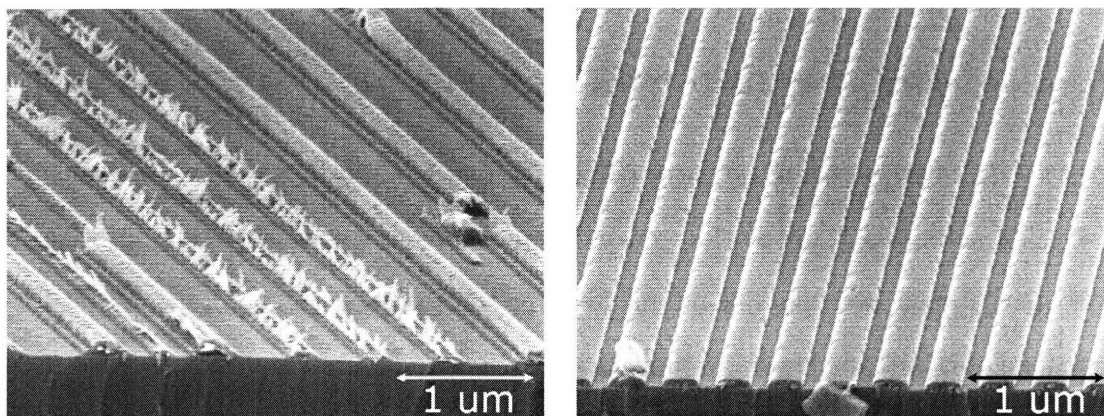

Figure 6-15: Imprinted pattern into PS-PFS, left without the use of a release layer on the mold, right, with release layer.

6.4 Directed assembly of PS-PFS under coated silicon molds

To explore the ordering of PS-PFS by in-situ annealing with nanoimprint lithography, several FOS-coated silica molds were fabricated by interference lithography. All molds were gratings of parallel mesas, with periods of 400 nm and 1000 nm. The gratings were fabricated in several depths, from 45 nm to 65 nm. The thickness of the block copolymer film before imprinting is also important as it determines the total amount of material available. If too much material is deposited prior to nanoimprinting, the mold will not be able to 'absorb' the entire polymer and some polymer will be trapped beneath the mesas. This layer would also microphase segregate, forming a

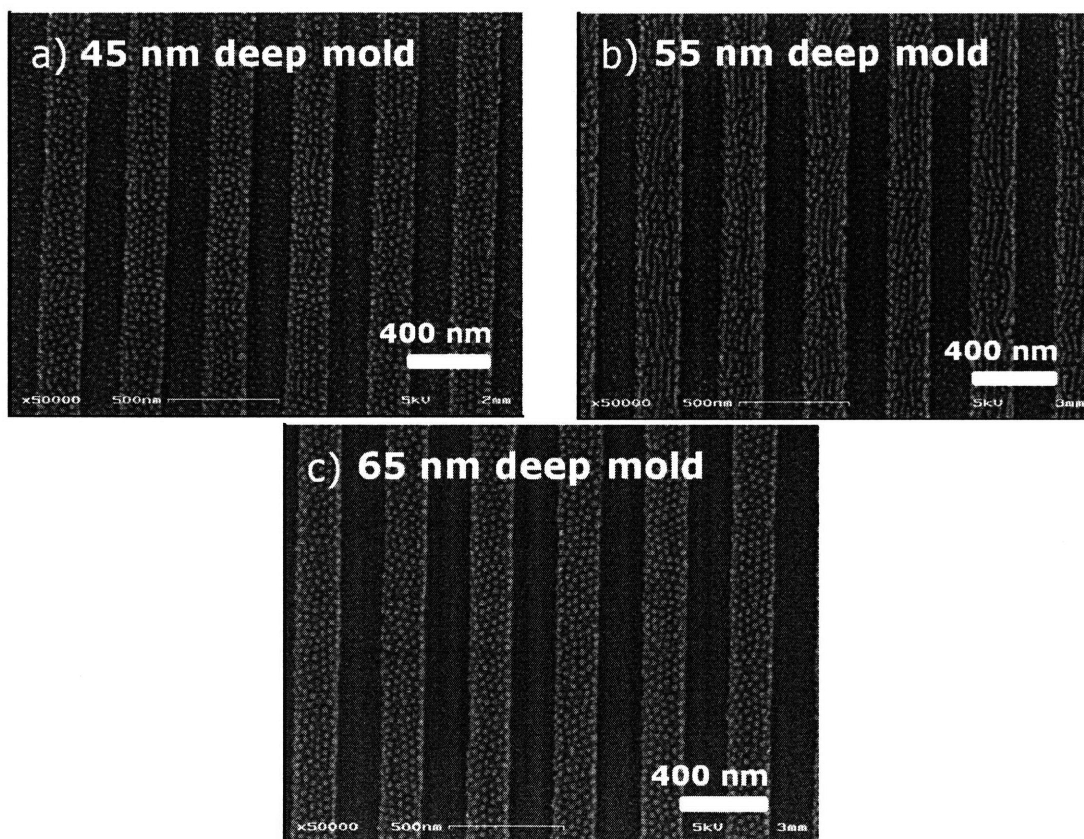

Figure 6-16: Mold was grating with 400nm period, a) 45nm deep mold, b) 55nm deep mold, c) 65 nm deep mold. All polymer was 47/15 spun at 45nm thickness.

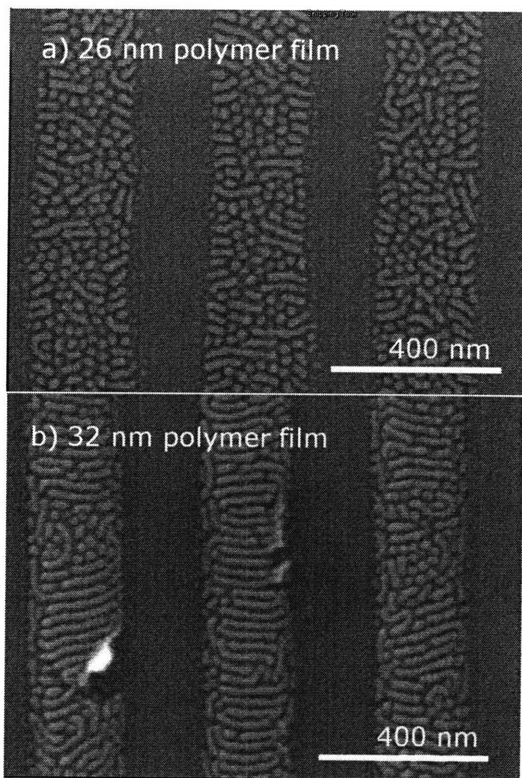

Figure 6-17: Mold was 400 nm period, 45 nm deep grating. Polymer was 33/10 spun to a) 26 nm, b) 32 nm.

pattern that would also transfer into the substrate which is undesirable. This is visible in some of the cases, such as Figure 6-16 a) and b), Figure 6-20 a) b) and c), Figure 6-21 a) and b).

We wanted to examine the effects the mold depth would have on the ordering of the block copolymer. For this purpose, we started with the same thickness 47/15 PS-PFS film of 45nm and imprinted it with same period mold but different depths. Figure 6-16 shows the resulting pattern. We see that when the mold is too shallow, the amount of block copolymer deposited is too high and evidence of microphase segregation is present underneath the mesas of the stamp. By using a deeper mold, such as Figure 6-16 c) no evidence of microphase segregation is visible at the bottom of the mesas, and just the pattern in the grooves is present. It should be noted that the quality of the self-assembly is not as good as we expected. On average, each PFS domain has 6 neighbors, but there is no clear guiding of the assembly. As it is a larger polymer with slower kinetics, we explored using 33/10 which has a longer correlation length than 47/15.

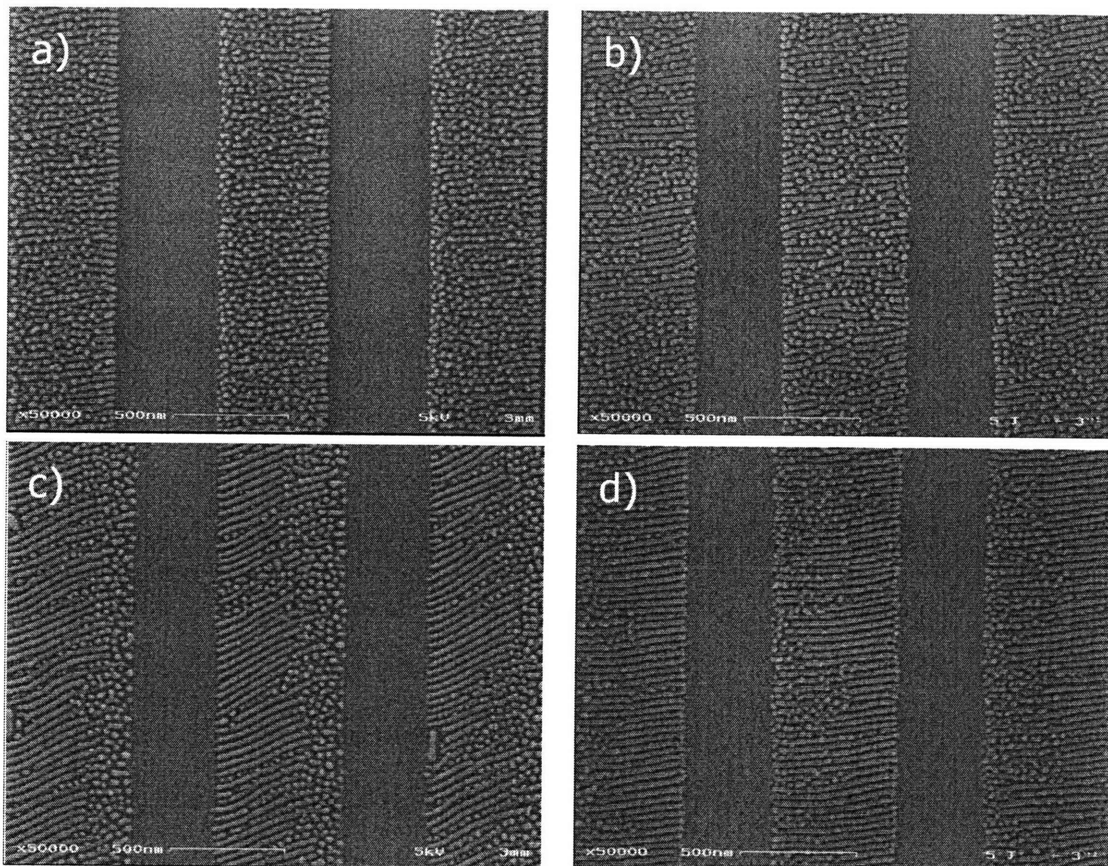

Figure 6-18: Mold was 1μm period, 65nm deep; polymer was 47/15 spun to a) 47nm, b) 42 nm, c) 38 nm, d) 36 nm.

Figure 6-17 shows the results of ordering the smaller 33/10 block copolymer underneath the coated silica grating molds. The polymer normally orders in the spherical morphology, but as can be seen from the micrographs, it seems to have taken on a mixed spherical and cylindrical morphology in these samples. It should be noted that the relative volume fraction of the block copolymer puts it just below the transition from spherical to cylindrical morphology. The exact mechanism behind the (partial) preference to ordering in the cylindrical morphology is unclear. It is possible that the FOS surface treatment is interacting with the block copolymer and the cylindrical morphology becomes preferential. Alternatively, the stresses during the imprinting could

be the contributing to the change of the morphology. There is extensive work (both theoretical [7, 8] and experimental [9-12]) which examines the effects of pressure on the phase behavior of polymers and polymer blends. Unfortunately no such studies have yet been carried out on PS-PFS so we cannot directly compare results. However, it should be noted that the block copolymer used in this work has a volume fraction which places it on the boundary between the cylinder and sphere forming morphology, so it is possible that the elevated pressures during imprint are causing the cylindrical morphology to become favorable.

The larger period grating molds do not produce an improvement to the ordering of the block copolymer. The block copolymer still forms a mix of the spherical and cylindrical morphologies. The cylinders order perpendicularly to the grating which is likely due to the flow-induced ordering of the block copolymer, similar to work reported by Jung [13]. The majority of the flow of polymer during the imprinting process is perpendicular to the grating as polymer flows from beneath the mesas into the grooves of the mold (Figure 6-19), so the cylinders are aligned along this direction. Interestingly, the samples that were annealed at a temperature of 175° C and were imprinted into a thinner polymer show only spherical morphology. The ordering is best out of all samples, but not of the expected quality (long range order which extends for many hundreds of microns to millimeters.

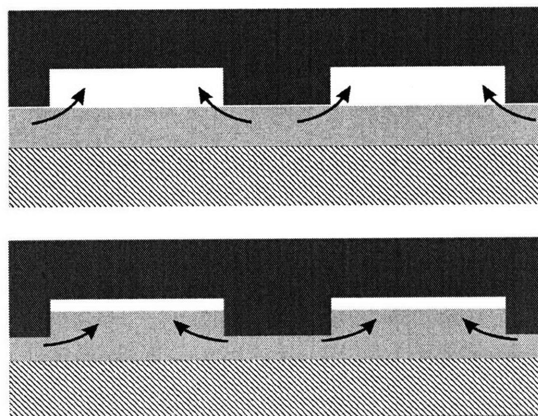

Figure 6-19: Flow of polymer during nanoimprinting.

Using the lower MW 33/10 PS-PFS was equally as unsuccessful in fabricating well-ordered arrays of block copolymers

(Figure 6-21). While thicker films left residue below the mesas (Figure 6-21 a), thinner films did form a single monolayer of spheres (Figure 6-21 c, d) under the grooves only. However, the long range order of the templated arrays is worse than the order in films spin-cast on flat substrates.

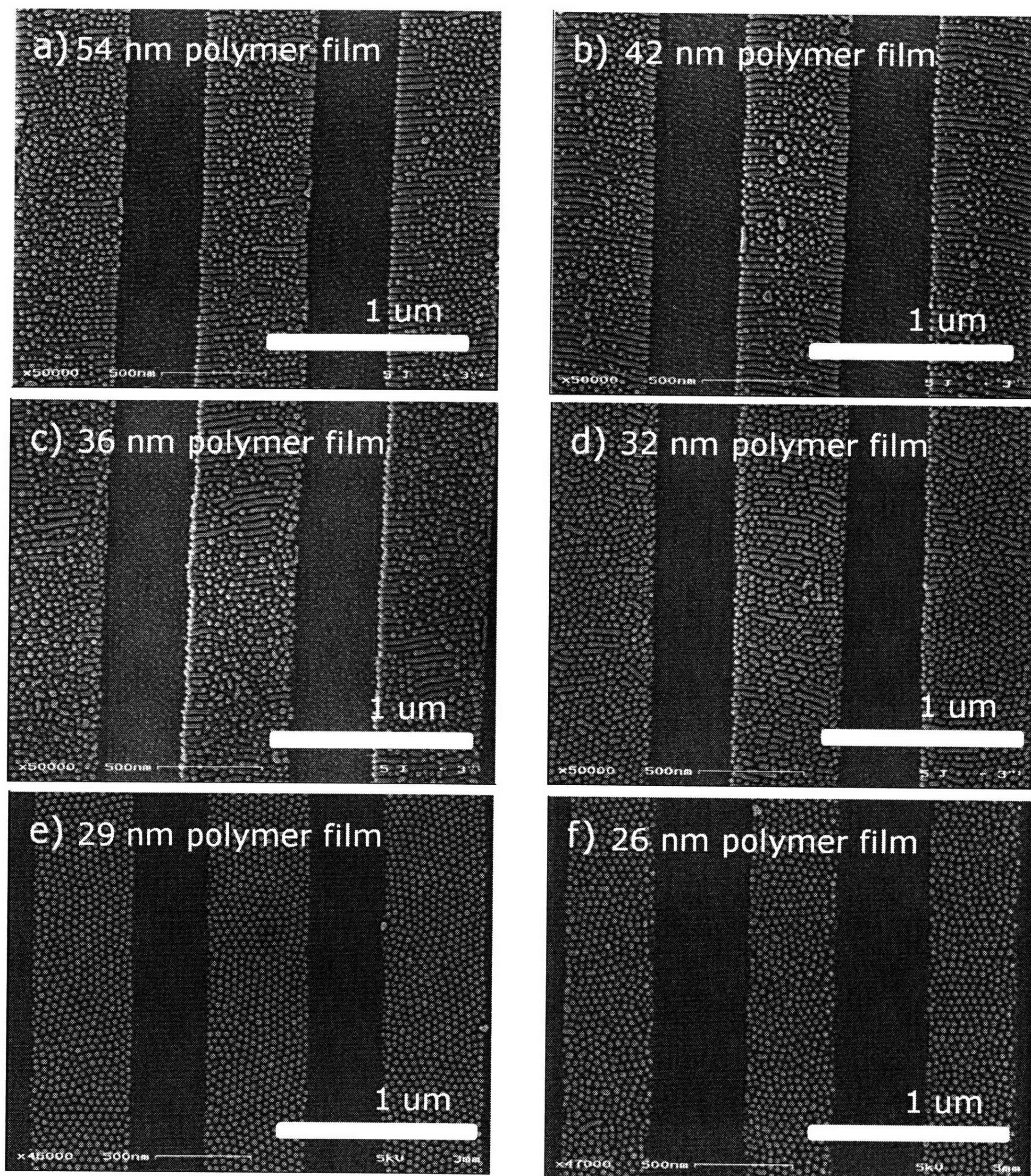

Figure 6-20: Mold was 55nm deep, 1 μm period grating. Polymer was 47/15 spun at a) 54 nm, b) 42 nm, c) 36 nm, d) 32 nm, e) 29 nm, d) 26 nm. Samples a-d were annealed at 150° C, and e-f were annealed at 175° C.

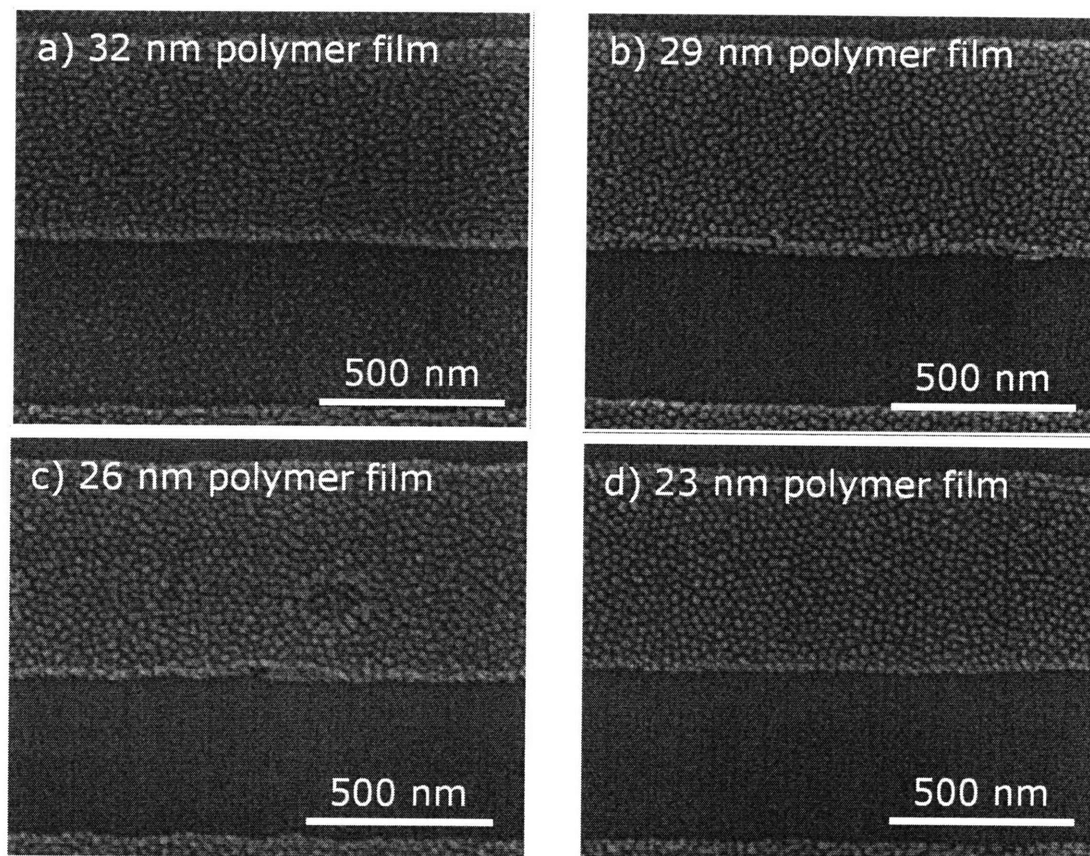

Figure 6-21: Mold was 1μm period, 55 nm deep grating; Polymer was 33/10 spun to a) 32nm, b)29 nm, c) 26 nm, d) 23 nm.

6.5 Conclusions

Selectively removable templates are a viable route to fabricating patterns that transfer directly and solely from patterns obtained in templated block copolymer systems. Several groove widths and polymer molecular weights were examined. Good ordering with very few defects was achieved in 33/10 PS-PFS and the pattern was successfully transferred first into silica and then into tungsten. The tungsten islands had 17 nm average diameter and were well ordered over large areas.

Modifications to the method of selectively removable templates are possible and straightforward for problems such as the addition of registration marks. These features are necessary for hard drive media, as well as other device oriented applications.

While nanoimprint lithography with in-situ annealing is an elegant method of guiding the self-assembly of block copolymers, practical applications of this method are difficult. Ordering is extremely dependent on the exact dimensions of the mold as well as the starting polymer thickness. Even when all parameters are optimized, the long range order is no better than that of a film spin-cast on a flat substrate. More work is necessary to further elucidate the effects of pressure and the boundary conditions on the long-range order of the PS-PFS block copolymer system. SANS studies of the ordering under pressure accompanied by calorimetry would yield information on the thermodynamics of PS-PFS, data necessary to optimize the ordering of PS-PFS with nanoimprint lithography.

While Huck *et al.* already examined cylindrical morphology PS-PMMA ordered by nanoimprint lithography, they only obtained patterns of the cylinders aligned parallel to the groove, or perpendicular to the substrate. Control over the ordering so that the block copolymer orders perpendicular to the template grating would enable higher flexibility in the achievable patterns using self-assembled methods. The alignment of cylinders perpendicular and diagonal to the groove might be caused by relative motion of the mold with respect to the substrate. Therefore, the effects of purposeful motion, both linear and oscillatory, between the mold and substrate should be examined to determine the ordering improvements on the block copolymer pattern.

References

[1] J. Y. Cheng, A. M. Mayes, and C. A. Ross, "Nanostructure engineering by templated self-assembly of block copolymers," *Nature Materials*, vol. 3, pp. 823, 2004.

[2] T. Deng, Y.-H. Ha, J. Y. Cheng, C. A. Ross, and E. L. Thomas, "Micropatterning of Block Copolymer Solutions," *Langmuir*, vol. 18, pp. 6719-6722, 2002.

[3] H. W. Li and W. T. S. Huck, "Ordered Block-Copolymer Assembly Using Nanoimprint Lithography," *Nano Lett.*, vol. 4, pp. 1633-1636, 2004.

[4] M. F. Spotts, T. E. Shoup, and L. E. Hornberger, *Design of machine elements*, 8th ed. Upper Saddle River, N.J.: Pearson/Prentice Hall, 2004.

[5] T. Bailey, B. J. Choi, M. Colburn, M. Meissl, S. Shaya, J. G. Ekerdt, S. V. Sreenivasan, and C. G. Willson, "Step and flash imprint lithography: Template surface treatment and defect analysis," presented at Papers from the 44th international conference on electron, ion, and photon beam technology and nanofabrication, 2000.

[6] G.-Y. Jung, Z. Li, W. Wu, Y. Chen, D. L. Olynick, S.-Y. Wang, W. M. Tong, and R. S. Williams, "Vapor-phase self-assembled monolayer for improved mold release in nanoimprint lithography," *Langmuir*, vol. 21, pp. 1158, 2005.

[7] T. Hino and J. M. Prausnitz, "Lower and Upper Critical Ordering Temperatures in Compressible Diblock Copolymer Melts from a Perturbed Hard-Sphere-Chain Equation of State," *Macromolecules*, vol. 31, pp. 2636-2648, 1998.

[8] J. Dudowicz and K. F. Freed, "Relation of effective interaction parameters for binary blends and diblock copolymers: lattice cluster theory predictions and comparisons with experiment," *Macromolecules*, vol. 26, pp. 213-220, 1993.

[9] A. V. G. Ruzette, A. M. Mayes, M. Pollard, T. P. Russell, and B. Hammouda, "Pressure Effects on the Phase Behavior of Styrene/n-Alkyl Methacrylate Block Copolymers," *Macromolecules*, vol. 36, pp. 3351-3356, 2003.

[10] O. Prasad, L. Sinha, N. Misra, G. P. Gupta, and R. C. Agnihotri, "Pressure induced order-disorder transition in a diblock copolymer," *Polymer*, vol. 46, pp. 11876, 2005.

[11] H. Frielinghaus, D. Schwahn, K. Mortensen, K. Almdal, and T. Springer, "Composition Fluctuations and Coil Conformation in a Poly(ethylene-propylene)-Poly(ethylethylene) Diblock Copolymer as a Function of Temperature and Pressure," *Macromolecules*, vol. 29, pp. 3263-3271, 1996.

[12] D. Schwahn, H. Frielinghaus, K. Mortensen, and K. Almdal, "Temperature and Pressure Dependence of the Order Parameter Fluctuations, Conformational Compressibility, and the Phase Diagram of the PEP-PDMS Diblock Copolymer," *Physical Review Letters*, vol. 77, pp. 3153, 1996.

[13] Y. S. Jung and C. A. Ross, "Orientation-controlled self-assembled nanolithography using a polystyrene - polydimethylsiloxane block copolymer," *Nano Letters*, vol. 7, pp. 2046, 2007.

Chapter 7

Conclusions and recommendations for future work

7.1 Conclusions

This research was aimed at understanding the methods of patterning magnetic films using self-assembled block copolymer masks and to understand the magnetic reversal mechanisms of as deposited and patterned magnetic films. First, the deposition of magnetic films with perpendicular anisotropy by UHV sputtering was optimized. We selected Co 66 at. % Cr 22 at. % Pt 12 at. % as the magnetic alloy as hcp cobalt has an easy magnetization axis oriented along the crystalline c-axis. To promote the c-axis texture out of plane, the magnetic films were deposited on a titanium seed layer. Early in the work it was noticed that the textured growth of the films is inhibited if contaminants are present in the sputtering gas. The effect of partial oxygen pressure was examined and it was found that good quality films can be grown if the oxygen concentration is lower

than 0.5%. Higher concentrations of oxygen during sputter-deposition lead to loss of texture and as a consequence, the films do not have a well defined easy magnetization axis.

Next, the perpendicular magnetic films were patterned by block copolymer lithography. Since reactive ion etching of magnetic metals is impractical, a hard-mask layer of tungsten was deposited so that the magnetic film may be patterned using Ne ion beam etching. A layer of silica was deposited to act as a mask for the tungsten, and a film of polystyrene-polyferrocenyldimethylsilane (PS-PFS) was spincoated from a toluene solution. After microphase segregation, the PFS block formed an array of close-packed spheres embedded in a PS matrix. The PS matrix was removed in oxygen reactive ion etching and the PFS spheres were used as a mask to transfer the pattern into silica, forming silica pillars. These pillars were then used as a mask to pattern the tungsten layer using reactive ion etching. Lastly the tungsten pattern was transferred into the magnetic layer by ion beam etching while the perpendicular alignment of the easy axis was not disturbed. Arrays of magnetic islands with no long range order were formed such that the easy magnetic axis of each island was pointing perpendicular to the sample plane.

Next, methods of imposing long range order on the pattern were examined. Two approaches were taken – nanoimprint lithography with in-situ annealing and selectively removable templates. The motivation for these approaches was the need to transfer only the pattern formed by the block copolymer and no the relief structure of the template.

Molds for nanoimprinting were fabricated out of monolithic silicon wafers using interference lithography and reactive ion etching. The molds were coated with a release layer and after imprinting the mold with sample was annealed as with non-templated samples. Nanoimprint lithography with in-situ annealing was successful in obtaining

regions of phase segregated block copolymer film; however, no long range ordering of the microdomains was achieved. Also, PS-PFS which normally orders in the spherical morphology was observed to form cylinders when templated under the mold. At this point, it is unclear what is the direct cause of the change of the block copolymer morphology, but we speculate that either the mold surface treatment or the pressure during annealing lie behind it. Further work is necessary to elucidate the exact mechanism. Interestingly, the cylinders orient themselves perpendicular to the groove, presumably due to shear-induced alignment (during imprinting, the mold induces a flow of the polymer which is generally perpendicular to the mold grooves).

Selectively removable templates were fabricated out of BARL-i anti reflection coating using a modification of the three-layer resist for interference lithography. These templates were spin-coated with PS-PFS, and after annealing the PS matrix was removed by oxygen reactive ion etching, and any remaining template was selectively dissolved in n-methylpyrrolidone leaving only PFS spheres on the surface. The long range ordering of the fabricated samples was comparable to long range ordering achieved by graphoepitaxy in silica trenches, and close packed arrays extended for large areas with very few defects. The ordered arrays were then transferred into silica, forming ordered arrays of silica pillars. From electron micrographs it was clear that only the pattern of the block copolymer was transferred while the removed template did not contribute to the topography. Next, the pattern was transferred into a W layer, forming an array of cp-packed W islands with period of 29 nm and island diameter of 17 nm. Transfer of the pattern into CoCrPt however, was difficult because of the non-selective ion beam etching process.

Magnetic analysis of the deposited perpendicular films revealed a reversal mechanism of domain nucleation and growth. This was evident both is single layer films

and in perpendicular pseudo-spin valve films (p-PSV) (Ti/CoCrPt/Ti/CoCrPt). The magnetic free layer of the p-PSV films can be cycled independently of the hard layer and exhibits a slow time-dependent magnetization reversal which was attributed to growth of reverse domains. In the case of the p-PSV, the domain propagation field is lower than the domain nucleation field, and MFM micrographs shows the different domain structure that arises from fast and slow magnetization reversal of the magnetic layers.

The magnetization reversal mechanism of patterned films was characteristically different than that of a continuous film. A series of 2D close-packed islands with varying sizes that were fabricated using block-copolymer lithography. Magnetic analysis showed that the islands reverse their magnetization in a coherent and independent fashion, in contrast to the domain nucleation and growth of a continuous film. One exception is the array of 5nm thick / 28nm diameter islands, in which interactions significantly influence the magnetic reversal. Micro-magnetic simulation confirmed the coherent reversal of the thicker islands.

7.2 Future work

While it would have been desirable to fabricate an ordered array of perpendicular magnetic islands and study the magnetic properties of such an array, much of the information has already been obtained from the disordered sample. Arrays could be fabricated by first prepatterning the substrate into a series of posts using the same methodology developed in this thesis, and then depositing a layer of perpendicular magnetic film. The material deposited in the trenches will be effectively isolated from that at the top of the posts, and could be analyzed magnetically by various methods.

Other process improvements to the lithographic processing should be examined, especially those relating to the quality of the structure. For example, the use of block

copolymers with good etch selectivity between the blocks and a larger Flory-Huggins parameter which order better (PS-PDMS for example) need to be examined for lithography purposes. Improvements in the synthesis of block copolymer are necessary so that polymers with a narrower polydispersity index are synthesized so that the size distribution of the microdomains is decreased. Additionally, improved templating and annealing processes should be explored so that device-grade patterns may be generated.

The behavior of the block copolymers during nanoimprinting needs to be further examined as it is a very interesting case. SANS studies of the ordering under pressure accompanied with simulation might provide insight as to why the normally spherical block copolymer orders in a cylindrical morphology. To avoid this situation, and obtain an ordered spherical pattern, a block copolymer which has volume fraction that places it further from the sphere-cylinder transition could be used. Nonetheless, nanoimprinting might be an interesting approach to ordering block copolymers with cylindrical morphology for applications where stripes are desired. While Huck *et al.* already examined cylindrical morphology PS-PMMA ordered by nanoimprint lithography, they only obtained patterns of the cylinders aligned parallel to the groove, or perpendicular to the substrate. Control over the ordering so that the block copolymer orders perpendicular to the template grating would enable higher flexibility in the achievable patterns using self-assembled methods. The alignment of cylinders perpendicular and diagonal to the groove might be caused by relative motion of the mold with respect to the substrate. Therefore, the effects of purposeful motion between the mold and substrate should be examined to determine the ordering improvements on the block copolymer pattern. Both linear motion and oscillatory motion might show interesting results. More generally, there is much interesting science to be explored in the combination of block copolymer and nanoimprint lithographies.

The work on the effect of oxygen during deposition opens an interesting question regarding the mode of growth of CoCrPt alloys. We only examined the films using magnetometry data, to complement these experiments, the depositions should be carried out on nitride membranes so that transmission electron microscopy may be used to observe the microstructure and draw a definite picture on the changes that occur when oxygen is introduced in the sputtering gas. Further research is needed on the effect of film microstructure on the reversal properties of patterned magnetic arrays. Also, magnetic force microscopy of ordered arrays should be examined for evidence of magnetic frustration and the results should be confirmed with modeling. The patterning should be extended to other systems, such as patterning perpendicular pseudo spin valves, which might lead to novel memory storage devices.

We have already seen that block copolymer lithography is particularly interesting as method of patterning periodic structures at the nanoscale. There are quite a few direct applications that block copolymers might address, such as patterned media, transistors, capacitors or other simple devices. Applications beyond patterned media should be explored, such as DNA sorting devices, plasmon waveguides or vertical transistors could be fabricated using guided self-assembled block copolymer lithography. As the methodology matures, it will be interesting to see what other applications are derived from the method. However, many issues remain unexplored or underexplored in order to fully demonstrate the potential of block copolymer lithography. While periodic patterns are interesting, certain controlled aperiodicities and intentional defect placement would permit encoding more information into the system so that, for example, servo-patterns may be written in an otherwise periodic structure. To that extent, more work is needed to better understand the role of templates in the control and formation of these aperiodic structures. Better theoretical and experimental analysis of

the kinetics of ordering in templated systems and full understanding of the effects of combined external fields and surface modifications would yield greater control over the uniformity of the pattern and allow for better device control.